Self-consistent modeling of relativistic runaway electron avalanches producing terrestrial gamma ray flashes

Pierre Gourbin

UNIVERSITÉ D'ORLÉANS

ÉCOLE DOCTORALE ÉNERGIE, MATÉRIAUX, SCIENCES DE LA TERRE ET DE L'UNIVERS

LABORATOIRE DE PHYSIQUE ET CHIMIE, DE L'ENVIRONNEMENT ET DE L'ESPACE (LPC2E)

THÈSE présentée par :

Pierre GOURBIN

soutenue le :

22 février 2024

pour obtenir le grade de : **Docteur de l'Université d'Orléans**

Discipline/ Spécialité : Sciences de l'Univers

SELF-CONSISTENT MODELING OF RELATIVISTIC RUNAWAY ELECTRON AVALANCHES PRODUCING TERRESTRIAL GAMMA RAY FLASHES

Modélisation auto-consistente d'avalanches d'électrons runaway relativistes produisant des flashs gamma terrestres

THÈSE dirigée par :

M. CELESTIN Sébastien	Professeur, Université d'Orléans

RAPPORTEURS :

M. CHANRION Olivier	Senior Researcher, DTU SPACE National Space Institute
M. LUQUE Alejandro	Senior Researcher, Institute for Astrophysics of Andalusia

---

JURY :

Mme HURET Nathalie	Professeur, Université Clermont Auvergne - **Présidente**
M. CHANRION Olivier	Senior Researcher, DTU SPACE National Space Institute
M. LUQUE Alejandro	Senior Researcher, Institute for Astrophysics of Andalusia

Abstract

English

Terrestrial gamma-ray flashes (TGFs) are short and intense bursts of gamma rays occurring during thunderstorms. Reported for the first time in 1994, a significant effort has been carried out to understand their properties and origins. It is agreed upon that TGFs are produced inside thunderclouds by relativistic runaway electron avalanches (RREAs): when submitted to a sufficiently high electric field, an electron can gain more energy from the field than it loses to collisions with air molecules, thus becoming runaway. Doing so, it ionizes the air, freeing more electrons, a small fraction of these electrons being themselves runaway, hence forming an avalanche of runaway electrons. The exact context in which RREAs are initiated inside thunderclouds remains up for debate. Two TGF-production theories are considered nowadays. The relativistic feedback mechanism rely on the backward propagation of photons and positrons created by a first RREA, to produce new avalanches near the starting location of the first RREA, allowing for an overall sufficient number of electrons and photons. The thermal runaway mechanism assumes that RREAs are created during lightning propagation: the strong electric field inside a streamer corona at the tip of leader could accelerate a high number

of electrons injected from the leader, triggering the production of subsequent RREAs leading to a TGF.

In this thesis, we formulate two outstanding questions that we address in the subsequent chapters. How the dynamics of RREAs is affected by self-consistent effects ? What is the importance of combined spatial and temporal aspects in the initiation of relativistic feedback ?

To address these questions, we have developed a new self-consistent relativistic model, using a Monte Carlo technique to simulate collisions with air molecules coupled with an electromagnetic particle-in-cell method, that solves the Maxwell-Ampere and Maxwell-Faraday equations at each timestep in order to represent accurately the interaction between the electromagnetic field and electrons. To our knowledge, this model constitutes the first fully causal relativistic description of RREAs. Using this new tool, we discovered that the low-energy electron density saturates at a predictable value. We also show that a fundamental limit exists in the number of high-energy electrons, with a magnitude matching TGF observations, and derive a simple formula giving the observed saturation density and electron number. In order to better understand the relativistic feedback mechanism, we devise a method to derive a value of the feedback threshold electric field. We then perform simulations of the feedback process using the complete model, which allows us to fully

appreciate the complexity of the phenomenon. From the results, we highlight the importance of taking into account all spatial and temporal aspects of the feedback process to describe it accurately. It also leads us to believe that the relativistic feedback mechanism is unlikely to act alone in the production of the shortest or most intense TGFs.

Français

Les flashs de rayons gamma terrestres (TGFs) sont des émissions très intenses et très brèves de rayons gamma se produisant durant les orages. Rapportés pour la première fois en 1994, de nombreuses recherches ont été menées afin de comprendre ses propriétés et origines. Il y a consensus quant au fait que les TGFs sont produit dans les nuages d'orage par des avalanches d'électrons runaway relativistes (RREAs): un électron soumis à un champ électrique suffisamment élevé peut gagner plus d'énergie du champ qu'il n'en perd via les collisions avec les molécules de l'air, devenant ainsi runaway. Il peut ainsi se propager et ioniser l'air, libérant de nouveaux électrons, dont certains sont runaway, formant ainsi une avalanche d'électrons runaway. Il y a cependant débat quant au contexte de l'initiation des RREAs dans les nuages orageux. Deux théories sont considérées à ce jour. Le mécanisme de feedback relativiste repose sur la propagation vers l'arrière de photons et de positrons produits

par une première RREA, qui pourraient produire de nouvelles avalanches au voisinage de la position de départ de la première RREA, permettant ainsi d'atteindre un nombre suffisant d'électrons et de photons. Le mécanisme de runaway thermique suppose que les RREAs sont créées pendant la propagation des éclairs: le champ électrique intense induit dans les couronnes de streamers qui se forment au bout de leaders pourraient accélérer une grande quantité d'électrons en provenance du leader, initiant ainsi la production de RREAs secondaires menant à un TGF.

Dans cette thèse, nous formulons deux questions non résolues que nous abordons dans les chapitres suivants. De quelle manière la dynamique des RREAs est-elle affectée par des effets auto-consistents ? Quelle est l'importance des aspects spatiaux et temporels combinés dans l'initiation du feedback relativiste ?

Pour répondre à ces questions, nous avons mis au point un modèle relativiste auto-cohérent, utilisant une technique de Monte Carlo pour simuler les collisions avec les molécules de l'air couplée à une méthode particle-in-cell (PIC) électromagnétique, qui résout les équations de Maxwell à chaque pas de temps afin de fournir une description détaillée des interactions entre le champ électromagnétique et les électrons. À notre connaissance, ce modèle constitue la première description pleinement causale des RREAs. En util-

isant ce nouvel outil, nous avons découvert que la densité d'électrons de basse énergie saturait à une valeur prédictible. Nous montrons également qu'une limite fondamentale existe pour le nombre d'électrons de haute énergie, avec une magnitude correspondant aux observations de TGFs, et déduisons une formule simple donnant la densité de saturation et le nombre d'électrons. Afin de mieux comprendre le mécanisme de feedback relativiste, nous mettons au point une méthode afin de déterminer la valeur du champ électrique seuil pour le feedback. Nous réalisons ensuite des simulations du processus de feedback en utilisant le modèle complet, afin d'apprécier la complexité du phénomène. À partir des résultats, nous démontrons l'importance de prendre en compte tous les aspects spatio-temporels du processus de feedback relativiste afin de le décrire correctement. Les résultats semblent également supporter l'idée que le mécanisme de feedback relativiste n'agit pas seul dans la production des TGFs les plus courts et les plus intenses.

Acknowledgments

These has been three great years spent in the LPC2E, and I wish to thank everyone who has been part my thesis. I would like first to thank CNES and region Centre-Val-de-Loire for funding this thesis. I wish to thank Olivier Chanrion and Alejandro Luque, who have accepted to review my manuscript and be part of the committee for my thesis. I also thank Nathalie Huret for accepting being part of the committee. I wish to thank Sebastien Celestin, my supervisor who was always available when I needed it, and was always here to push me to go further in this exciting project. I am grateful that I have been able to have such a great PhD advisor. I would also like to thank the info team: Claire, Xavier, Franck and Nathalie, and the admin team: Isabelle, Aurore, and Tiphaine. They were all of great help whenever I needed it. Merci aussi à Mathieu Garnung, qui m'a transmis les connaissances nécessaires pour que je puisse m'acquitter de ma tâche de Gourou de l'info du bureau 211.

The LPC2E, where I spent those three years, was a great place to work or even to spend time in, filled with all kind of interesting and pleasant people, many of them I call friend today. I wish to thank all my colleagues: merci à Melody, pour m'avoir accueilli du mieux possible en pleine période de confinement, et avec qui j'ai passé de bon moments de franche rigolade ; merci à

Nina, avec qui on a également bien rigolé, et avec qui on forme la meilleure équipe de baby-foot qui soit ! Merci à Andrea Larosa, qui m'a motivé à faire du vélo et a essayé de me m'initier à la plongée (même si apparemment je suis plus à l'aise les pieds au sol), et merci à Vamsee pour m'avoir cédé son vélo à prix d'ami. Merci également à Pietro, pour sa cuisine, son humour et son soutien, à Gaetane, qui a toujours des idées vachement chouettes pour divertir toute la bande, à Manu, avec qui Gaetane et moi avons escaladé moult murs (et qui m'a emmené aux urgences quand j'ai escaladé le mur de trop...), et Jeremie, dont l'humour et la conversation étaient à nul autre pareil. I also wish to thank our friends from the SAMPLE team: Alexander and Rima, who made this journey even funnier with their presence, and now Loic, who trained me to be the babyfoot player I am now. Merci également à Yanis, qui prendra la relève à la tête du bureau 211 quand je serai parti, et Hakim, dont les connaissances théoriques obscures lui permettront, j'en suis sûr, de trouver la masse du photon. Merci enfin à Lucas, qui a fini peu avant moi, Camille, qui faisait sortir Lucas de sa grotte, Luca, Federico et Clara Froment. Tout ce beau monde ont été une joyeuse compagnie qui ont rendu ces trois années inoubliables. Je souhaite mentionner les étudiants stagiaires avec qui j'ai travaillé: Lorenzo et Killian.

Lastly, I wish to thank my family: merci à Maman, Papa, Marine et

Charles, qui ont toujours été là quand j'en avais besoin, et qui ont rendu cette expérience plus agréable.

Contents

Chapter 1

Introduction

1.1 Terrestrial Gamma-ray Flashes

In 1994, Fishman et al. [1994] report the discovery of a new terrestrial phenomenon related to thunderstorms. Their paper describes the discovery of brief (< 1 ms) and intense flashes of gamma rays observed in the atmosphere by the BATSE instrument on board the Compton Gamma-Ray Observatory (CRGO), a NASA space observatory initially dedicated to the observation of high-energy photons produced by cosmic events. At first, the flashes were believed to originate from an altitude of at least 30 km, lasting from 1 to 4 ms, and have spectra consistent with bremsstrahlung emission. These phenomena would be later named Terrestrial Gamma-ray Flashes, or TGFs.

Since then, TGFs have been the subject of many studies, allowing to better understand their properties. Using observations from the Reuven Ramaty High Energy Solar Spectroscopic Imager (RHESSI), comparisons between the spectrum of these emitted photons and Monte Carlo models have been used to determine the source altitude, which was found to be between 10 and 15 km [Dwyer and Smith, 2005; Xu et al., 2012]. Observations from the

Astro-Rivelatore Gamma a Immagini Leggero (AGILE) satellite mission, as well as the Gamma-ray Burst Monitor (GBM) installed on board the Fermi satellite (NASA), have allowed to constrain the duration of the event, which lasts $\sim$ 100 μs [Fishman et al., 2011; Marisaldi et al., 2015], as well as the energy of the emitted photons, which can go up to $\sim$40 MeV [Marisaldi et al., 2010; Briggs et al., 2010; Mailyan et al., 2016, 2019]. From observations by the RHESSI, which were then confirmed by the Fermi/GBM, as well as the CRGO/BATSE and the Atmosphere-Space Interaction Monitor (ASIM) (an instrument funded by ESA on board the International Space Station (ISS)), it has been estimated that between 10^{17} and 10^{19} photons are emitted at the source [Dwyer and Smith, 2005; Gjesteland et al., 2015; Mailyan et al., 2016, 2019; Lindanger et al., 2021]).

While the majority of TGFs are emitted upwards, downwards emitting TGFs have also been discovered, allowing observations from the ground [Dwyer et al., 2004; Abbasi et al., 2018; Belz et al., 2020], making it easier to perform multi-point and multi-instrumental observations, potentially leading to a better understanding of sources geometries [Berge and Celestin, 2019; Belz et al., 2020].

Airborne observations of TGFs have also been made, using instruments on board an aircraft, like the Airborne Detector for Energetic Lightning Emis-

sions (ADELE) [Smith et al., 2011; Bowers et al., 2018], or the more recent Airborne Lightning Observatory for FEGS and TGFs (ALOFT) campaign in 2023 [Østgaard et al., 2023].

In addition to the observation of gamma-rays, optical and radio emissions have also been detected in association with TGFs. Radio emissions over a broad range of frequencies have been observed in association with TGFs: Energetic In-cloud Pulses (EIPs) (peak-current $>$ 150 kA, duration $\sim$50 μs [e.g., Lyu et al., 2016; Tilles et al., 2020]), slow LF pulses (duration of 50 to 100 μs, frequency frequency 3–300 kHz) [e.g., Pu et al., 2019]. TGFs are strongly suspected to be accompanied with VHF emissions (30-300 MHz) [e.g., Lyu et al., 2018]. Optical emissions have been reported in Heumesser et al. [2021] and Skeie et al. [2022], and shown to be linked to the propagation of a lightning discharge occurring at the same time. Heumesser et al. [2021] reports that all the TGFs in the study were associated with optical emissions due to lightning propagations, and that $\sim$ 90 % of the TGFs occurred on the onset of the optical emission, supporting the idea of a connection between the two. Specific optical emissions produced as a result of the propagation of runaway electrons in air have also been predicted by models [Dwyer et al., 2013; Xu et al., 2015].

A number of models have been developed to complement the numerous

observations made, trying to reproduce TGFs and better understand their properties and initiation mechanism. Many models include a Monte Carlo method [e.g., Lehtinen et al., 1999; Moss et al., 2006; Dwyer, 2007, 2021], that allows to simulate accurately the collisional processes of runaway electrons as well as photons. Fluid models are another option [e.g., Liu and Dwyer, 2013; Berge et al., 2022; Pasko et al., 2023], and recently particle-in-cell models have also been used to try to replicate more accurately the interactions between the electric field and the charged particles [e.g., Chanrion and Neubert, 2008; Luque, 2014].

Despite the accumulation of data on TGFs, from both simulations and observations, many questions remain regarding their nature, context, properties, and origins. Their global occurrence rate has been estimated to be ∼400,000 per year for TGFs detectable by Fermi [Briggs et al., 2013], yet observations from the recent ALOFT campaign [Østgaard et al., 2023] reported the detection of many TGFs not detectable by space-based instruments, questioning this number. Studies have also been made in order to assess the potential threat that TGFs could pose for irradiated aircraft passengers [e.g., Dwyer et al., 2010; Pallu et al., 2021, 2023], but the uncertainties over the geometry of TGFs and their frequency pose challenges for such estimations.

Another mystery regards the initiation of a TGF.

1.2 Relativistic Runaway Electron Avalanche (RREA)

Wilson [1925] describes the behaviour of electrons that, if propagating under a sufficiently high electric field, could gain more energy than they lose due to collisions with ambient particles, and thus could continuously accelerate, becoming what is called "runaway electrons" [see Moss et al., 2006, Figure 2]. Provided sufficient propagation distance, these runaway electrons could undergo an avalanche process, and create other runaway electrons at an exponential rate [Gurevich et al., 1992], forming what is now referred to as Relativistic Runaway Electron Avalanche (RREA). The RREA allows the production of an important number of relativistic electrons, that can then emit gamma-rays via bremmstrahlung emission.

It is currently agreed upon that RREAs are the fundamental TGF production mechanism [Dwyer and Smith, 2005; Celestin et al., 2012; Dwyer et al., 2012]. The environment inside a thundercloud provides regions with intense electric fields and potentials, which should allow the initiation of RREAs. However, to produce a RREA intense enough to match TGF energies, a great number of seed particles need to be submitted to an intense electric field over extended regions [Dwyer, 2008]. To attain such conditions, two theories have been proposed: The leader-based mechanism (or thermal runaway mechanism) and the relativistic feedback mechanism.

1.2.1 Relativistic feedback mechanism

Dwyer [2008] mentions that the backwards propagation of X-rays and positrons could lead to the initiation of subsequent avalanches: by undergoing Compton scattering, photoelectric effect, or elastic scattering in the case of positrons, new runaway electrons could be produced near the starting location of the first avalanche, allowing the propagation of secondary RREAs in the same acceleration region. This would allow an exponential increase in the number of electrons and an intensification up to energies and fluxes matching those of TGFs. Dwyer [2007] mentions that this mechanism can increase the production of relativistic electrons by a factor of 10^{13} compared to one RREA propagating through the large scale electric field. Moreover, simulations made in Dwyer [2008] show that a TGF could be produced by this phenomenon on timescales extending from several tens of microseconds to 1 ms, which matches observed TGF durations.

This model has been simulated several times [Dwyer, 2003; Skeltved et al., 2014; Pasko et al., 2023], showing consistent results, and have been shown to be able to reproduce the radio emissions [Dwyer and Cummer, 2013] in association with TGFs.

1.2.2 Thermal runaway mechanism

The leader based, or thermal runaway mechanism, is based on the assumption that RREAs are produced during lightning propagation [e.g., Moss et al., 2006; Celestin and Pasko, 2011; Celestin et al., 2015]. During negative leader propagation, plasma filaments called streamers form at the tip of the leader. In the streamer fronts, the electric field can become sufficiently intense to allow free electrons to become runaway. Indeed, lightning leaders are known to produce X-rays through this mechanism [e.g., Moore et al., 2001; Saleh et al., 2009; Schaal et al., 2012; Xu et al., 2014, 2017]. Under the high electric field in the vicinity of the negative leader tip, the number of available electrons to become runaway is very high (the energy threshold is low). Provided that the streamer corona corresponds to a sufficient potential drop over its limited extent, these electrons could lead to a RREA intense enough to be able to generate a TGF.

This model is consistent with observations that show a strong correlation between lightning propagation and TGFs [e.g., Heumesser et al., 2021], and recent works have been able to reproduce slow LF pulses observed in association with TGFs [Berge et al., 2022].

1.3 Objectives

As of now, many unknowns remain regarding TGF initiation, as we lack understanding about the nature and context of the production of these intense radiation sources inside thunderstorms. The two theories presented offer a possible explanation, yet we still are unable to either validate or discard either theories. The leader-based seeding mechanism is not incompatible with relativistic feedback but usually infers smaller acceleration regions of a few hundreds of meters [Pasko et al., 2023].

Many numerical models have simulated accurately the RREA [e.g., see Dwyer and Smith, 2005; Celestin and Pasko, 2010; Dwyer et al., 2012], and many key features are now known. However, radio observations have yet to be reproduced numerically in the context of electric discharges, and all models until now have lacked causal self-consistency between charged particles and electromagnetic fields. It is a key feature: as the velocity of runaway electrons approaches the speed of light, the electrostatic approximation may become invalid.

From these unknown features, we draw two outstanding questions that we will address in this thesis:

- How the dynamics of RREAs is affected by self-consistent effects ?

- What is the importance of combined spatial and temporal aspects in the initiation of relativistic feedback ?

To address these research questions, and to advance the analysis of radio emissions, we have developed a new numerical model, coupling Monte Carlo and particle-in-cell methods. This model distinguishes itself from others, in that it is fully causal. Using the local Maxwell equations to solve the dynamics of the electromagnetic field, this new approach allows for full self-consistency between charged particles and the electromagnetic field, and opens a new, more accurate way to simulate RREAs and relativistic feedback processes. It is also well-suited to study radio emissions. A description in detail of this new model, as well as its validation, are presented in Chapter 2.

With our newly developed model, we performed our first simulations of RREAs in simple configurations, to assess the capabilities of the model and to highlight potential self-consistent effects. The simulations were performed in homogeneous electric fields, either relatively weak electric fields over a great distance, or intense electric fields over short distances. In these simulations, we point out peculiar behaviours that had never been reported, highlighting the importance of self-consistency. We define and discuss new constraints on the RREA, and come to a better understanding of previously made observations. These results and their implications are presented in Chapter 3.

We then focus on the relativistic feedback mechanism. Several articles had reported different thresholds for the mechanism to occur [Dwyer, 2003; Pasko et al., 2023]. In order to either validate or invalidate those thresholds, we try to use our model to study the phenomenon dynamically. The study of this phenomenon highlights new physical features such as the need for a temporal resolution. The details of these method and results are presented in Chapter 4.

Chapter 2

Methods

Contents

The results presented in this chapter are published in Gourbin and Celestin [2024b, Section 2]

2.1 Monte Carlo Method

In order to keep track of the dynamics of electrons and photons in air in a causal fashion, we use a null-collision-technique Monte Carlo model based on that developed by Celestin and Pasko [2011]. The model is 3-dimensional in configuration space, 3-dimensional in velocity space, fully relativistic, and is able to simulate the dynamics of electrons and photons in air over an energy

range going from sub-eV to hundreds of MeVs. The air is assumed to be made of 80% nitrogen and 20% oxygen.

2.1.1 Electrons

Following Moss et al. [2006], 23 excitation collisional processes are taken into account for N_2 (rotational, vibrational, and electronic) and 11 for O_2 including also dissociative processes. The only difference with Moss et al. [2006] is that the dissociation of the oxygen molecule into $O(^3P)$ and $O(^3S)$ with a threshold of 14.7 eV is not taken into account in the model. It is expected to play only a minor role. At energies greater than $\sim$1 keV, which is the energy range of interest in the present study concerning the Monte Carlo model, excitation cross sections are extrapolated logarithmically. Moreover, as angular scattering differential cross sections are not readily available for all excitation processes, the direction of electrons' momenta after excitation collisions is assumed identical to that in the case of elastic scattering (see below). It is worth noting that excitation processes only have an overall minor role in the dynamics of high-energy electrons and are of rather low-probability compared to ionization and elastic collisions. They are described here for the sake of completeness as the model can be used over an energy domain extended to lower energies.

The dynamics of $>$ 1 keV electrons in air is dominated by ionization and

elastic collisions. Ionization is modeled through the use of the relativistic binary-encounter-Bethe (RBEB) model to obtain an orbital-based analytical singly differential cross sections (DCS) (Kim et al. [2000]). It is conveniently integrable analytically and does not need adjustable parameters as it only requires orbital kinetic energies and binding energies of target electrons (Hwang et al. [1996]; Santos et al. [2003]). The RBEB model provides a seamless coverage over the whole energy domain for primary and secondary electrons well-suited for the description of RREAs (e.g., see Xu et al. [2015]; Celestin and Pasko [2010]; Celestin et al. [2015]). The direction of the secondary electron's momentum is obtained from the conservation of energy and momentum (e.g., see Celestin and Pasko [2010]).

We use the inverse transform sampling of the DCS to tabulate the energy of secondary electrons as a function of a uniformly distributed random number for all primary electron energies ([Moss et al., 2006, eq. (22)]). However, the ionization DCS shows strong dynamics over the broad energy range of interest and a linear sampling of secondary energies would require an enormous number of points to obtain a sufficient resolution. To avoid it, we empirically found that the following non-linear sampling of the DCS integral was well-suited:

$$I_{\mathrm{DCS}}(\varepsilon_s) = \frac{1}{\sigma_i(\varepsilon_p)} \int_0^{\varepsilon_s} \frac{d\sigma(\varepsilon_p, \varepsilon_s)}{d\varepsilon_s} d\varepsilon_s \tag{2.1}$$

$$J_{\mathrm{DCS}}(\varepsilon_s) = -\log\left(1 - I_{DCS}(\varepsilon_s)(1-\varepsilon)\right) \tag{2.2}$$

where $\frac{d\sigma(\varepsilon_p,\varepsilon_s)}{d\varepsilon_s}d\varepsilon_s$ is the ionization DCS, $\sigma_i(\varepsilon_p)$ is the total ionization cross section, and ε is set to a value of 10^{-10} to avoid the argument of the logarithm to reach exactly one. It is now $J_{\mathrm{DCS}}(\varepsilon_s)$ that we sample linearly over N_R values (in the present case we use $N_R = 10,000$, which has proven to be sufficient). Using a random number R_{ε_s} uniformly distributed between 0 and 1, the energy index of the secondary electron is then found by taking the integer part of:

$$-\log\left(1 - R_{\varepsilon_s}(1-\varepsilon)\right)N_R \tag{2.3}$$

Although ionization collisions drive the electrons' linear energy loss, elastic collisions significantly impact their dynamics in phase space (e.g., Dwyer [2010]). Below 500 eV, we use differential cross sections obtained experimentally in N_2 (Shyn et al. [1972]; Kambara and Kuchitsu [1972]). The differential cross section for O_2 is assumed identical (for more details on the comparison of angular scattering between N_2 and O_2 at low energy, see [Moss et al., 2006, Figure 3, and references therein]).

For high-energy electrons (>500 eV) we consider that elastic scattering from molecules is similar to elastic scattering by atoms. Assuming that the electric potential of the nucleus and the atomic electrons result in a screened Coulomb potential, one can show that the angular differential cross section

has the following form (Carron [2006]; Dwyer [2007]) :

$$\frac{d\sigma_{\mathrm{e}}}{d\Omega} = \frac{1}{4}\left(\frac{Zr_{\mathrm{e}}}{\beta^2\gamma}\right)^2 \frac{1-\beta^2\sin^2(\chi/2)}{\left(\sin^2(\chi/2)+\dfrac{\hbar^2}{4p^2a^2}\right)^2} \tag{2.4}$$

where $\beta = v/c$ of the electron, $\gamma = (1-\beta^2)^{-1/2}$, χ is the scattering angle, $d\Omega$ is the corresponding differential solid angle, Z is the atomic number (i.e., $Z = 7$ for nitrogen and $Z = 8$ for oxygen), r_{e} is the electron classical radius, p is the electron momentum, and a is the atomic screening radius. For the sake of comparison with previous works, we use $a \simeq 1.3413Z^{-1/3}a_0$, where a_0 is the Bohr radius, which is the same value as that used in Dwyer [2007].

In Monte Carlo simulations, the scattering angle χ after one collision is calculated through a uniformly distributed random number R_χ between 0 and 1, by finding χ so that:

$$R_\chi = \frac{2\pi}{\sigma_{\mathrm{e}}^{\mathrm{a}}(\varepsilon)} \int_0^\chi \frac{d\sigma_{\mathrm{e}}}{d\Omega} \sin\chi \, d\chi \tag{2.5}$$

where $\sigma_{\mathrm{e}}^{\mathrm{a}}(\varepsilon) = 2\pi \displaystyle\int_0^\pi \frac{d\sigma_{\mathrm{e}}}{d\Omega} \sin\chi \, d\chi$ is the total elastic cross section for nitrogen or oxygen atoms. Equation (2.5) may be solved numerically by pre-tabulating R_χ. However, high-energy electrons being much more forward-scattered than low-energy electrons, the corresponding sampling would have to be performed cautiously. Instead, it is possible to obtain an accurate solution of equation (2.5) through analytical considerations and this is the method we use.

Let $A = \dfrac{1}{4}\left(\dfrac{Zr_{\mathrm{e}}}{\beta^2\gamma}\right)^2$ and $B = \dfrac{\hbar^2}{4p^2a^2}$, plugging equation (2.4) in (2.5), one

can integrate analytically equation (2.5). One finds:

$$R_\chi = \frac{4\pi A}{\sigma_{\mathrm{e}}^{\mathrm{a}}}(\varepsilon)\left(-\beta^2 \ln X - \frac{2(B\beta^2+1)}{X} + \beta^2 \ln(2B) + \frac{B\beta^2+1}{2B+1}\right) \tag{2.6}$$

where $X = 2B - \cos\chi + 1$. To solve directly this equation for X, and then for χ, one could use the inverse function of $f(W) = W\exp(W)$, where W is named the Lambert W-function. However, the Lambert W-function is uncommon and its use is not necessary in this context as one can make the following approximations. Over the energy range of interest, the term varying as $\sim(B\beta^2+1)/X$ in equation (2.6) is always dominant over the term in $\sim\beta^2\ln(X)$, and $B\beta^2 \ll 1$. Hence, one gets:

$$X = \left(\frac{-4}{\frac{\sigma_{\mathrm{e}}^{\mathrm{a}}(\varepsilon)R_\chi}{2\pi A} - 2\beta^2\ln(2B) - 2\beta^2 - \frac{2}{B}}\right) \tag{2.7}$$

The scattering angle χ can be calculated from R_χ through the following formula:

$$\chi = \arccos\left(\frac{4}{\frac{\sigma_{\mathrm{e}}^{\mathrm{a}}(\varepsilon)R_\chi}{2\pi A} - 2\beta^2\ln(2B) - 2\beta^2 - \frac{2}{B}} + 2B + 1\right) \tag{2.8}$$

Note that this method, although very accurate, is an approximation and the domain of validity for $0 < R_\chi < 1$ is not fully covered. The following condition has to be added: if the argument of the arccosine on the right-hand side of equation (2.8) is found to be lower than -1, then χ is set to exactly π. The highest probability of occurrence of the latter condition is reached for

electrons with energy ∼3 keV, and corresponds to only 1.33 times over 100,000 elastic collisions on average. For electrons with energies 1 and 10 MeV, the occurrence rates are 1.55 over one million and 3.2 times over one hundred million, respectively.

One can calculate the total elastic scattering cross section through the integration of equation (2.4):

$$\sigma_{\mathrm{e}}^{\mathrm{a}}(\varepsilon) = 2\pi \int_0^{\pi} \frac{d\sigma_{\mathrm{e}}}{d\Omega} \sin\chi \, d\chi \tag{2.9}$$

One finds:

$$\sigma_{\mathrm{e}}^{\mathrm{a}}(\varepsilon) = 2\pi A \left(-2\beta^2 \ln(2) + \frac{2(B\beta^2+1)}{B(B+1)} \right) \tag{2.10}$$

which is the elastic scattering cross section for nitrogen or oxygen atoms. When calculating the probability of elastic collisions of high-energy electrons with nitrogen or oxygen molecules the molecular cross section should be used: $\sigma_{\mathrm{e}}^{\mathrm{m}}(\varepsilon) \simeq 2\sigma_{\mathrm{e}}^{\mathrm{a}}(\varepsilon)$. In addition, for the calculation of the elastic scattering cross section using equation (2.10), from which the collision probability in the Monte Carlo code is found, we use the classical screening radius in the Thomas-Fermi model: $a \simeq 0.885 Z^{-1/3} a_0$. Indeed, comparisons of the total elastic scattering cross section given by equation (2.10) with the Evaluated Electron Data Library (EEDL) Cullen et al. [1991] at different energies for nitrogen atoms and with [Itikawa, 2006, Table 3] at 1 keV for nitrogen molecules (using

$\sigma_{\mathrm{e}}^{\mathrm{m}}(\varepsilon) \simeq 2\sigma_{\mathrm{e}}^{\mathrm{a}}(\varepsilon)$) have showed a very good agreement for this magnitude of the screening radius in the elastic cross section.

2.1.2 Photons

To be able to process the interactions of photons in our model, we must first generate them. For the sake of simplicity, we consider the bremsstrahlung emission to only happen between an electron and a particle of one of the two species composing our atmosphere. The cross sections and differential dross dection for the generation of bremsstrahlung photons are computed and interpolated/extrapolated from Seltzer and Berger [1986](tables for Z=7 and 8). The total cross sections are derived by integrating the extrapolated DCS on the whole range of energies considered, for each incident electron energy. The total bremsstrahlung cross section for the oxygen or nitrogen is computed as following:

$$\sigma_{\mathrm{brem}}^{\mathrm{a}}(E_e) = \int_{k=10^3}^{k=E_e} \frac{d\sigma_{\mathrm{brem}}}{dk} dk \tag{2.11}$$

where E_e is the incident electron energy, $\frac{d\sigma_{\mathrm{brem}}}{dk}$ is the bremsstrahlung DCS for the oxygen atom or nitrogen atom. As it is the case for other electron interactions, molecular cross-sections should be used when computing the probability of bremsstrahlung: $\sigma_{\mathrm{brem}}^{\mathrm{m}}(E_e) \simeq 2\sigma_{\mathrm{brem}}^{\mathrm{a}}(E_e)$. We note that the minimum incident electron energy considered for bremsstrahlung is 1 keV. This is also the minimum photon energy considered in our model. Hence, any photons with

an energy below 1 keV is discarded.

The photon transport is processed the same same way as in the case of electrons, using the null-collision method. As the electrons are far more likely to interact with the air, it is their maximum collision frequency that will dictate the timestep used in our simulation. Three types of interactions are processed: Compton scattering, photoelectric effect, and e^+e^- pair production. The cross-sections used for these interactions were taken from Berger et al. [2010].

For Compton scattering, the scattered photon energy and scattering angle are described respectively using the Klein-Nishina formula and the energy-momentum conservation condition [Lehtinen, 2000; Pilkington and Anger, 1971; Heitler, 1960]. The approximated formula used to compute the new energy can be written this way [Lehtinen, 2000]:

$$E'_\gamma = \frac{E_\gamma}{1 + sR + (2\frac{E_\gamma}{mc^2} - s)R^3} \tag{2.12}$$

$$s = \frac{E_\gamma}{mc^2 + 0.5625E_\gamma} \tag{2.13}$$

where E'_γ is the new photon energy, E_γ is the incident photon energy, and R is an uniform random number.

The scattering angle is computed relatively to the incident photon trajec-

tory using the formula:

$$\chi_\gamma = \arccos\left(1 + \frac{mc^2}{E_\gamma} - \frac{mc^2}{E'_\gamma}\right) \tag{2.14}$$

The azimuthal angle of scattering is uniformly distributed.

For the photoelectric effect, we assume that all of the incident photon energy is transferred into the photoelectron. The photoelectron emission angle is drawn from a lookup table made using equation (2.12) in Carron [2006]:

$$\frac{d\sigma}{d\Omega} \sim \frac{\sin^2\theta}{(1-\beta\cos\theta)^4}\left\{\frac{1}{\gamma} + \frac{1}{2}(\gamma-1)(\gamma-2)(1-\beta\cos\theta)\right\} \tag{2.15}$$

The pair production refer here to the production of an electron and a positron from a photon. In our model, we assume that the positron is immediately annihilated into two 511 keV photons. This simplification prevents phenomena such as positron feedback to occur, however e^+e^- pair production has shown to be negligible throughout our simulations compared to Compton effect and photoelectric effect because of the configuration studied (photoelectric effect), the second also contributing to the feedback mechanism, as the photons are able to propagate backwards over a non negligible distance before interacting.

2.2 Electromagnetic Particle-In-Cell (PIC) model

One of the difficulties of simulating plasmas is to correctly describe the electromagnetic interactions between charged particles. The simplistic solution

would be to compute at each timestep all the Coulombian interactions produced by each particle on all the other particles (i.e., solving the N-body problem), but this quickly becomes unbearable when the number of particles becomes relatively high. The PIC method proposes another solution: particles move freely according to the relativistic equations of motions, but the electromagnetic field they create is described and updated over a grid, and is then recomputed onto the particle locations via an interpolation technique. The computation gains come from the fact that the number of grid points can be strongly limited and each particle handled in simulations actually represent a great number of real particles (electrons in the present work). This is made possible through a careful discretization of Vlasov equation into characteristic curves resulting in the trajectories of these "macro-particles" or "computer-particles" in phase space.

The use of electromagnetic particle-in-cell code to model and simulate plasmas is described in Birdsall and Langdon [1991] and Hockney and Eastwood [1966] (see also the remarkably clear description given by Lehe [2014]) The method relies on solving Maxwell's equations, that will be used to update the electric and magnetic fields at each time step. Our model is a cylindrical axisymmetric implementation of the PIC method. We identify four steps in a cycle of the PIC code:

- Interpolation of fields onto the particles (Section 2.2.3)
- Update of the particle positions using the relativistic equation of motion (Section 2.2.1)
- Assignment of the particles charges and currents on the grid (Section 2.2.3)
- Update of the electromagnetic fields using Maxwell's equations (Section 2.2.2)

We detail these different steps in the following sections.

2.2.1 Equation of motion of the electrons

Describing the particle movements is straightforward, as we simply use the equations of motion, in the following form:

$$\frac{d\mathbf{p}_i}{dt} = q_e(\mathbf{E} + \mathbf{v}_i \times \mathbf{B}) \tag{2.16}$$

$$\frac{d\mathbf{x}_i}{dt} = \frac{\mathbf{p}_i}{\gamma m_e} \tag{2.17}$$

$$\gamma_i = \frac{1}{\sqrt{1 - \frac{|\mathbf{v}_i|^2}{c^2}}} = \sqrt{\frac{1 + |\mathbf{p}_i|^2}{(m_e c)^2}} \tag{2.18}$$

where $\mathbf{E}$ is the electric field, $\mathbf{B}$ the magnetic field, q_e the particle charge, $\mathbf{v}_i$, $\mathbf{p}_i$ and $\mathbf{x}_i$ are respectively the particle i velocity, momentum, and position

vectors, m_e the particle mass, and γ_i the Lorentz factor. The use of relativistic equations is required here, as the typical electron speed in a relativistic avalanche is around $0.9c$, with c the speed of light in vacuum. To discretize the equations, we use the relativistic Boris algorithm, as the naive approach results in breaking energy conservation and introduces significant errors on the cyclotron frequency. We first define $\eta_i = q_e|B^{n+1}|\Delta t/(2\gamma_i m_e)$. The Boris algorithm computes the momentum as follows:

$$p^{n+1}_{xyz,i} = p^{n}_{xyz,i} - \frac{q_e \Delta t}{2}\left(E^{n+1}_{xyz,i} + F^{n+1}_{\text{rad},i} \cdot \frac{p^{n}_{xyz}}{P_i}\right) \tag{2.19}$$

$$p^{*}_{xyz,i} = p^{n+1}_{xyz,i} + \frac{1}{|B^{n+1}|}\tan\eta_i \cdot \left(p^{n+1}_{yzx,i}B^{n+1}_{zxy,i} - p^{n+1}_{zxy,i}B^{n+1}_{yzx,i}\right) \tag{2.20}$$

$$p^{n+1}_{xyz,i} = p^{n+1}_{xyz,i} + \frac{1}{|B^{n+1}|}\frac{2\tan\eta_i}{1+\tan^2\eta_i}\left(p^{*}_{yzx,i}B^{n+1}_{zxy,i} - p^{*}_{zxy,i}B^{n+1}_{yzx,i}\right) \tag{2.21}$$

$$p^{n+1}_{xyz,i} = p^{n+1}_{xyz,i} - \frac{q_e \Delta t}{2}\left(E^{n+1}_{xyz,i} + F^{n+1}_{\text{rad},i} \cdot \frac{p^{n+1}_{xyz}}{P_i}\right) \tag{2.22}$$

where xyz is either x, y, or z, i is the index of the electron, n is the time index, E_i, B_i and $F_{rad,i}$ are respectively the interpolated electric and magnetic field at the location of particle i and the continuous radiative friction applied on this particle. In the present model, the production of individual photons does not affect the dynamics of the particles and this is why a radiative friction is included (especially for electrons with energies >10 MeV). It is taken from Berger et al. [2005]. We then update the velocity and position:

$$v_{xyz}^{n+1} = p_{xyz}^{n+1}/(\gamma m_e) \tag{2.23}$$

$$xyz^{n+1} = xyz^n + v_{xyz}^{n+1}\Delta t \tag{2.24}$$

2.2.2 Computation of the electromagnetic field

The electromagnetic field is computed using a finite-difference time-domain (FDTD) scheme on a grid at each timestep using the following Maxwell-Faraday and Maxwell-Ampere equations:

$$\frac{\partial \mathbf{B}}{\partial t} = -\nabla \times \mathbf{E} \tag{2.25}$$

$$\frac{\partial \mathbf{E}}{\partial t} = c^2(\nabla \times \mathbf{B} - \mu_0 \mathbf{J}) \tag{2.26}$$

where c is the speed of light in vaccuum, μ_0 the permeability of free space, and $\mathbf{J}$ is the conduction current density. This current density, as well as the particles densities and charge density are all computed on the same numerical grid as that used for the electromagnetic field. The current density $\mathbf{J}$ is calculated through summation of the current assigned onto the grid from computer particles (see Section 2.2.3) and the current densities of ions and low-energy electrons calculated using fluid equations (see Section 2.4).

To initialize the field, we use the Maxwell-Gauss equations:

$$\nabla \cdot \mathbf{E} = \frac{\rho}{\varepsilon_0} \tag{2.27}$$

$$\nabla \cdot \mathbf{B} = 0 \tag{2.28}$$

with ε_0 the permittivity of free space and ρ the charge density. In practice, the electric field is initialized with a Poisson equation, and a homogeneous field is added in the cases presented in this article. The magnetic field is initialized as equal to 0 on the whole domain. Equations (2.27) and (2.28) are considered as initial conditions if charge is conserved. If they are true at instant $t = 0$, they remain true at all instants, provided that the continuity equation for the charge is verified:

$$\frac{\partial \rho}{\partial t} + \nabla \cdot \mathbf{J} = 0 \tag{2.29}$$

It is hence critical that the numerical model ensures that the charge of the system is preserved (see Section 2.2.3), otherwise a Poisson equation corrector has to be implemented to establish consistency between the electric field and the charge density [Birdsall and Langdon, 1991, section 15.6].

The grid used is a Yee lattice, meaning a combination of two grids, one for the cells themselves, or cell centers, and another for the interfaces. The grids are staggered from one another, and thus two sets of coordinates are used. Different properties represented on the grid are placed at different positions

relative to the cell centers, which allows for consistency when, for example, updating the magnetic field at a point requires to know the rotational of the electric field at this point. The form of the grid used, as well as the different field components, are shown in Figure 2.1.

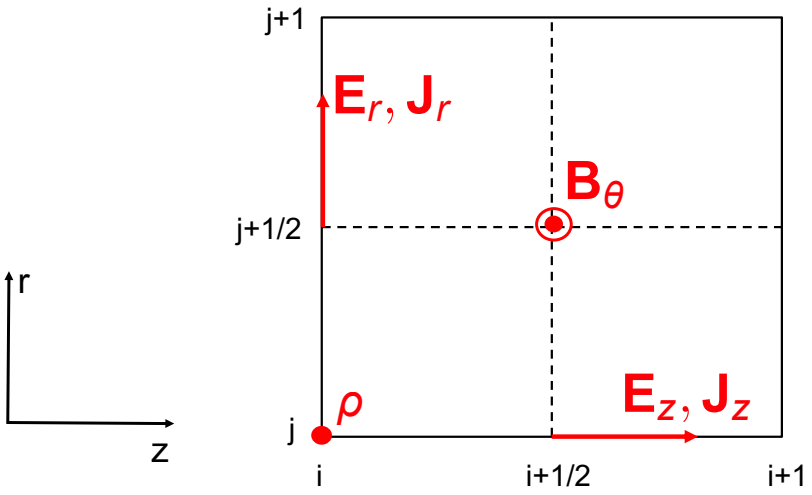

Figure 2.1: Representation of a cylindrical Yee lattice. The solid black lines represent the cell-centered grid, while the dashed black lines represent the interface grid. The interface grid is indexed using "half-coordinates" (+1/2). The different components of the computed fields are represented in red at their respective position on the lattice. The charge density ρ is scalar, and computed on cell centers. The components of the current density J_r and J_z are positioned at the interfaces.

Because of the axisymmetry of the model, we can restrain the computation of the different fields to the derivation of the components represented in Figure 2.1. If we assume the distance between two cell-centers is equal to Δz (resp. Δr), the distance between a cell center and its interfaces is $\frac{\Delta z}{2}$ (resp. $\frac{\Delta r}{2}$). On

this grid, the discretization for the electric field then goes as follows:

$$E_{r\,i,j+1/2}^{\;n+1} = E_{r\,i,j+1/2}^{\;n} - c^2\Delta t\left(\frac{B_{\theta\,i+1/2,j+1/2}^{\;n+1/2} - B_{\theta\,i-1/2,j+1/2}^{\;n+1/2}}{\Delta z} + \mu_0 J_{r\,i,j+1/2}^{\;n+1/2}\right) \tag{2.30}$$

$$b1_{i+1/2,j} = RIG_{j+1/2}B_{\theta\,i+1/2,j+1/2} - RIG_{j-1/2}B_{\theta\,i+1/2,j-1/2} \tag{2.31}$$

$$E_{z\,i+1/2,j}^{\;n+1} = E_{z\,i+1/2,j}^{\;n} + c^2\Delta t\left(\frac{b1_{i+1/2,j}}{RG_j\Delta r} - \mu_0 J_{z\,i+1/2,j}^{\;n+1/2}\right) \tag{2.32}$$

where E_z and E_r are the z and r components of the electric field, J_z and J_r the z and r components of current density, B_θ is the θ component of the magnetic field, RG and RIG are arrays with the r coordinates of respectively cell-centers and interfaces. $b1$ is an intermediate variable, and is not used elsewhere.

The magnetic field is also staggered in time compared to the electric field, which must be taken into account in the Maxwell equations. The general form of the magnetic field equation excluding boundaries is:

$$B_{\theta\,i,j}^{\;n+1/2} = B_{\theta\,i,j}^{\;n-1/2} + \Delta t\left(\frac{E_{z\,i,j}^{\;n} - E_{z\,i,j-1}^{\;n}}{\Delta r} - \frac{E_{r\,i,j}^{\;n} - E_{r\,i-1,j}^{\;n}}{\Delta z}\right) \tag{2.33}$$

It should be noted that the staggering in time must be taken into account in the particle movement as the particle move over integer timesteps. To do that, we average ${B_\theta}^{n-1/2}$ and ${B_\theta}^{n+1/2}$ to have the magnetic field at time $n\Delta t$.

2.2.3 Assignment of charges and currents and field interpolation

The passage from the particles to the cells of the grid is the core of the particle-in-cell method, and must be handled carefully, especially regarding charge conservation.

For the charge assignment, a first order scheme called cloud-in-cell (CIC) is used. The scheme is widespread in PIC-type simulations and described in Birdsall and Langdon [1991] and Hockney and Eastwood [1966]. On a 2-D grid, the idea is to distribute the charge among the four nearest cells by multiplying it with what is called a shape factor : each cell has its factor, which is comprised between 0 and 1, and the sum of the four factors is equal to 1. Graphically, the particle can be represented on a 2-D grid as a uniformly distributed "cloud", that is separated into four "sub-charges", as shown in Figure 2.2.

If we name the cells (i, j), $(i+1, j)$, $(i, j+1)$, and $(i+1, j+1)$ respectively 1, 2, 3, and 4, we can describe each shape factor by the following formula:

$$S_k = \frac{1}{\Delta z \Delta r} z_k^{\mathrm{loc}} r_k^{\mathrm{loc}} \tag{2.34}$$

where k is the cell index equal to 1, 2, 3, or 4, S_k is the shape (or form) factor, Δz and Δr are the interval between cells respectively in the z and r direction, as shown in Figure 2.2, and z_k^{loc} and r_k^{loc} are respectively the local coordinates

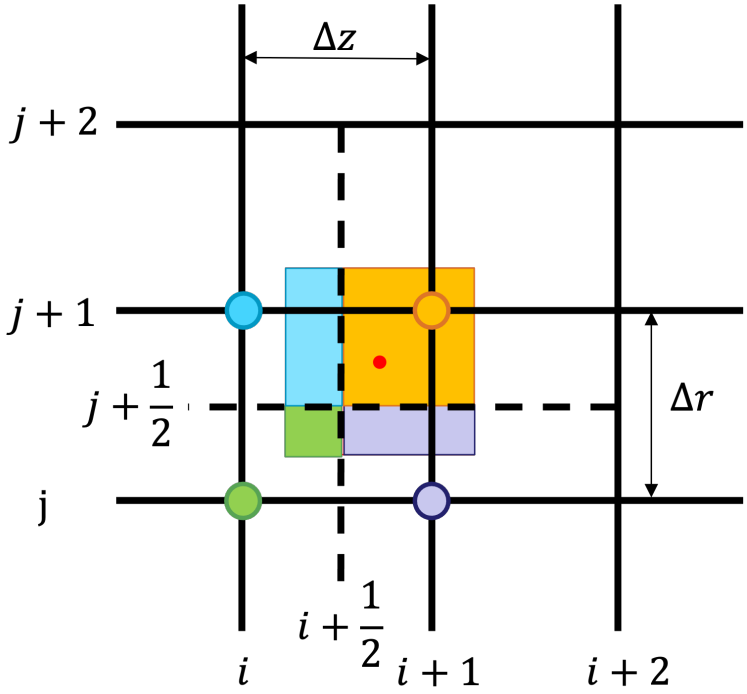

Figure 2.2: Deposition of the charge of one particle onto the grid. The solid lines represent the 'cell grid.' The dashed lines represent the 'interface grid.' The square around the particle has the dimensions of one cell. The four areas that form the square are used to attribute the values of the four form factors that are to be used to assign the charge to the four marked cells.

of the particle relative to the corresponding cell. We can write them as such:

$$z_{1,3}^{\mathrm{loc}} = z_i + \Delta z - z_p = z_{i+1} - z_p \tag{2.35}$$

$$z_{2,4}^{\mathrm{loc}} = z_p - z_i \tag{2.36}$$

$$r_{1,2}^{\mathrm{loc}} = r_j + \Delta r - r_p = r_{j+1} - r_p \tag{2.37}$$

$$r_{3,4}^{\mathrm{loc}} = r_p - r_j \tag{2.38}$$

where (z_p,r_p) is the absolute position of the particle in the simulation domain, and (z_i,r_j) are the coordinates of the corresponding cell.

The contribution of particles on the charge density assigned to each cell is

the shape factor multiplied by a "local" charge density $n_k = \frac{q_p}{V_{\text{cell}k}}$:

$$\rho_k = n_k S_k \tag{2.39}$$

where q_p is the particle charge and $V_{\text{cell}k}$ the volume of a cell. In a 2-D Cartesian grid, $V_{\text{cell}k}$ is usually constant. However, in the case of our cylindrical axisymmetrical grid, each cell is a torus of revolution with a square section $\Delta z \Delta r$ and a width depending on the position of the cell on the r-axis. If $0 \leq r_j \leq \frac{\Delta r}{2}$, then the shape of the cell is a cylinder. To take into account this geometry when computing the charge density, we use a different volume for each coordinate j on the r-axis:

$$V_{\text{cell}}(j) = \pi \Delta z (r_{j+1}^2 - r_j^2) \tag{2.40}$$

As said previously, the same scheme will be used to interpolate the field on the particle. Note that when interpolating the magnetic field on the particles, we take the average of $B^{n-1/2}$ and $B^{n+1/2}$ to obtain the value B^n at the current timestep $n\Delta t$ before making the interpolation. The fields applied to the particle will be the sum of the fields at each of the four nearest cells multiplied by the corresponding shape factors so as to avoid the introduction of spurious self-forces. Indeed, the PIC methods separates the calculation of particle motion and the evolution of fields. The fields are therefore not necessarily physically consistent with the position and motion of particles

and spurious behaviors such as a particle exerting a force on itself, the so-called self-force, as well as other inconsistencies can occur. To avoid such problems, the shape factor used for charge and current density assignment to the grid simply needs to be the same as that used for the field interpolation [Hockney and Eastwood, 1966]. It can be proven that in this case, self-forces and other inconsistencies cancel out. For this reason, the search for typical inconsistencies is a convenient way to sanity-check PIC simulation codes.

However, we can demonstrate that a current assigned though the CIC scheme does not automatically verify the continuity equation (e.g., see Lehe [2014]). Let us consider a 1D-grid with a cell size of Δz on which a particle of charge q_p is moving. The timestep is Δt. We use the cloud-in-cell assignment scheme for both the charge and the current density. The shape factor $S(z-z_p)$ is therefore expressed as $1 - \dfrac{|z - z_p|}{\Delta z}$ for $|z - z_p| < \Delta z$ and 0 otherwise, with z the position of the point being assigned, and z_p the particle position. The situation from $t = n\Delta t$ to $t = (n+1)\Delta t$ is represented in Figure 2.3.

To validate our scheme, we need to verify that the charge is conserved over all cells. Particularly, we can express charge conservation on the cell-center of position $k\Delta z$ as follows:

$$\frac{\rho_k^{n+1} - \rho_k^n}{\Delta t} + \frac{J_{z\,k+1/2}^{\,n+1/2} - J_{z\,k-1/2}^{\,n+1/2}}{\Delta z} = 0 \tag{2.41}$$

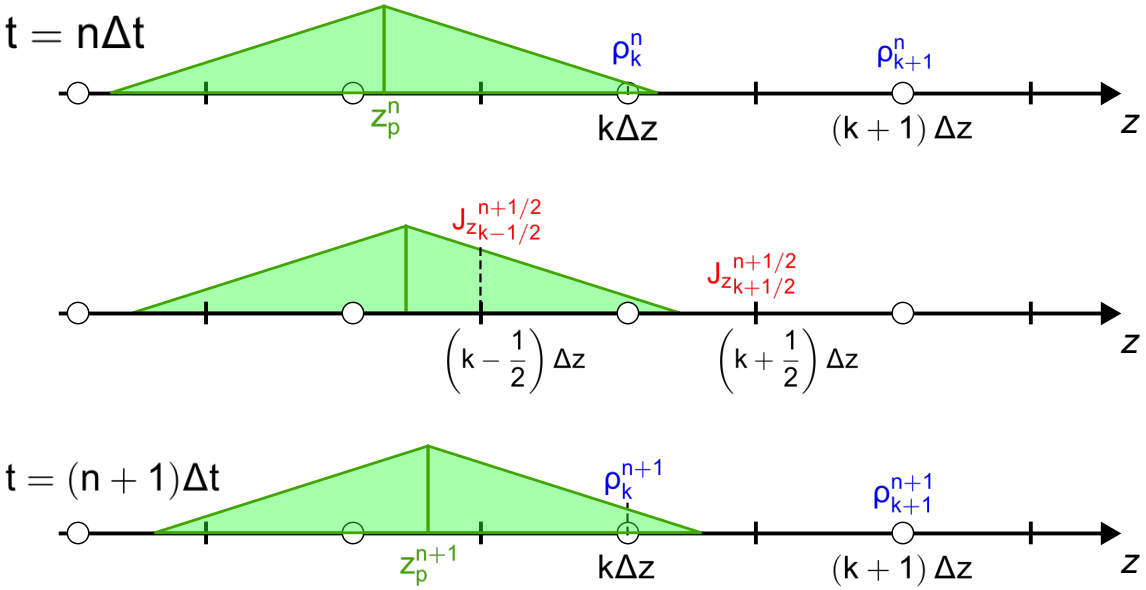

Figure 2.3: Representation of the movement of a particle at position z_p on a 1D-grid. The green area represents the shape of the cloud of the particle. On the grid are represented the cell-center positions $(k'\Delta z)$ on which are computed the charge density $\rho^{n'}_{k'}$ and the interface positions $((k'+1/2)\Delta z)$ on which are computed the current density $J_{z\,k'+1/2}^{\,n'+1/2}$

We can express ρ and J_z:

$$\begin{aligned}
\rho_k^n &= \frac{q_p}{\Delta z} S(k\Delta z - z_p^n) \\
&= \frac{q_p}{\Delta z}\left(1 - \frac{k\Delta z - z_p^n}{\Delta z}\right) && (2.42)\\
J_{z\,k-1/2}^{\,n+1/2} &= \frac{q_p}{\Delta z} v_z^{n+1/2}\left(1 - \frac{(k-1/2)\Delta z - z_p^{n+1/2}}{\Delta z}\right) && (2.43)\\
J_{z\,k+1/2}^{\,n+1/2} &= 0 && (2.44)
\end{aligned}$$

with $v_z^{n+1/2} = \dfrac{z_p^{n+1} - z_p^n}{\Delta t}$ and $z_p^{n+1/2} = \dfrac{z_p^n + z_p^{n+1}}{2}$.

We can write the two terms of the continuity equation:

$$\begin{aligned}
\frac{\rho_k^{n+1} - \rho_k^n}{\Delta t} &= \frac{q_p}{\Delta z \Delta t}\left(1 - \frac{k\Delta z - z_p^{n+1}}{\Delta z} - 1 + \frac{k\Delta z - z_p^n}{\Delta z}\right) \\
&= \frac{q_p}{\Delta z^2 \Delta t}\left(z_p^{n+1} - z_p^n\right) && (2.45)
\end{aligned}$$

$$\begin{aligned}
\frac{J_{z_{k+1/2}}^{n+1/2} - J_{z_{k-1/2}}^{n+1/2}}{\Delta z} &= 0 - \frac{q_p}{\Delta z} v_z^{n+1/2} \left(1 - \frac{(k-1/2)\Delta z - z_p^n}{\Delta z}\right) \\
&= -\frac{q_p}{\Delta z \Delta t} \left(z_p^{n+1} - z_p^n\right) \left(1 - k + \frac{1}{2} + \frac{z_p^{n+1/2}}{\Delta z}\right) \\
&= -\frac{q_p}{\Delta z^2 \Delta t} \left(z_p^{n+1} - z_p^n\right) \left(\left(\frac{3}{2} - k\right)\Delta z + z_p^{n+1/2}\right) \qquad (2.46)
\end{aligned}$$

As we can see when we compare equations (2.45) and (2.46), the sum of the two is not equal to 0 in all cases. Therefore, using the CIC scheme for the current assignment is not consistent with charge conservation.

A way to correct this discrepancy is to use a Poisson corrector on the electric field, cancelling the difference introduced by current assignment Birdsall and Langdon [1991]. However, the time cost makes it an inconvenient solution, so instead we use a specific current assignment scheme, described in Villasenor and Buneman [1992]. Like in the CIC scheme, the particle is described as a cloud with the shape of a cell and an uniform charge, however the shape factor is not computed using the distance of the particle to the computing points, but rather the amount of charge going through each interface, determined by the volume of the cloud going through it.

Provided that the CFL condition is verified, the movement over one timestep can only affect four interfaces at once (movement relative to the nearest interface point), seven interfaces at once (movement from one inter-

face point to another in either the axial or radial direction), or in the rarest cases ten interfaces at once (movement from one interface point to another in a diagonal direction).

We can quickly check that the CFL condition is verified: in most cases presented in this article, the cell dimension is $\Delta z = \Delta r = 8$ m, and the timestep used is $\Delta t = 3.4 \times 10^{-13}$ s. The Courant number is computed as such on our grid:

$$C = U_z \frac{\Delta t}{\Delta z} + U_r \frac{\Delta t}{\Delta r} \tag{2.47}$$

with U_z and U_r the z and r components of the velocity. We can maximize the Courant number by taking c as the value of each component of the speed, thus giving a value of $C = 2.5493 \times 10^{-5}$, which is way below 1, hence verifying the CFL condition.

The different types of movements are shown in Figure 2.4. We have verified that the last kind of movement (Figure 2.4(c)) is rare enough so that we can neglect them without a significant loss of charge conservation. The various runs performed have shown close to no such movement, with sometimes only one at the very beginning, and none afterward, validating this assumption.

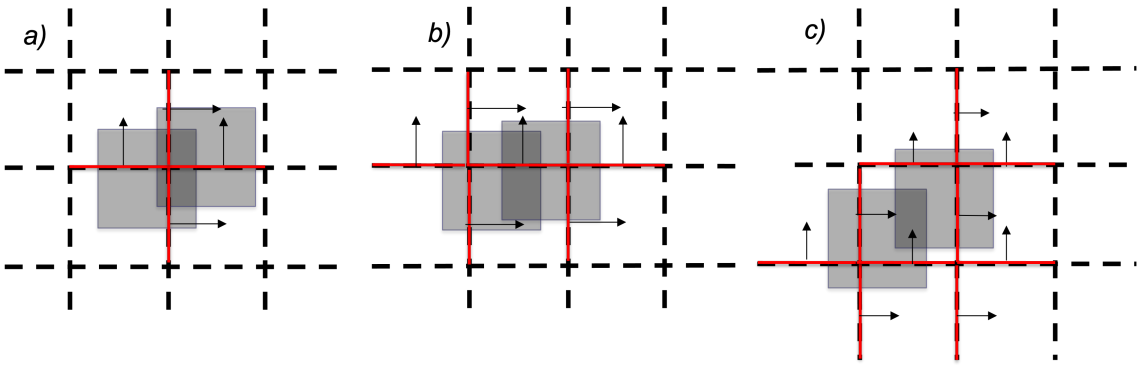

Figure 2.4: Three of the different types of movements considered in the Villasenor scheme. the dashed lines are the interfaces (forming the interface grid), the red lines and associated arrows show the interfaces through which a current is produced. The two squares represent the old and current position of the particle cloud. The movements here are exaggerated for clarity. a) four-boundary movement ; b) seven-boundary movement, on the horizontal direction ; c) ten-boundary movement. The two interfaces that are affected without touching the clouds in this movement are so because of the decomposition of the movement.

2.2.4 Validation of the particle-in-cell code using the simulation of an homogeneous relativistic plasma

Additionally to validation tests of the FDTD, Monte Carlo, and fluid parts alone, we have tested the coupling of fields and particles performed by the PIC method. For single particles, no self force was observed [Hockney and Eastwood, 1966]. For multiple particles, we have defined a homogeneous plasma of relativistic electrons and static ions.

In this simulation, we fill the domain ($z = 500$ m, $r = 150$ m here) with electrons, the velocities of which are drawn from a Maxwellian distribution of temperature $T = 2.57 \cdot 10^7$ K. The domain boundaries are defined as periodic. In the first run of this case, we put 40000 particles with a weight of $2 \cdot 10^{14}$,

giving us $8 \cdot 10^{18}$ electrons. We put as many ions to neutralize the plasma. The initial electromagnetic field is considered equal to zero. We then move some of the electrons to form a hole in the electron population in the (z,r) domain, hence creating a charged location that will serve as an initial perturbation. We let the simulation run for about 10 μs, and observed that the velocity distribution remains Maxwellian.

As noted by many authors, waves present a valuable tool to perform verification tests of plasma models [e.g., Palmroth et al., 2018]. Therefore, the main purpose of this test is to verify that we obtain the correct dispersion relation. The dispersion relation of electromagnetic waves in a plasma is described as follows:

$$\omega_{EM}(k) = \sqrt{\omega_p^2 + c^2 k^2} \tag{2.48}$$

where $\omega_{EM}(k)$ is the angular frequency in rad/s for the electromagnetic waves, ω_p the plasma frequency, c the speed of light, and k the wave number. However, the use of the Yee scheme with a staggered grid to compute the various components of the electromagnetic field induces changes in the behavior at higher frequencies and wave numbers approaching the Nyquist limit. It is in fact dictated by the relation dispersion of the Yee scheme [Kilian et al., 2017,

4.1]:

$$\left(\frac{2}{\Delta t}\right)^2 \sin^2\left(\frac{\omega \Delta t}{2}\right) = \omega_p^2 + c^2 \left(\frac{2}{\Delta z}\right)^2 \sin^2\left(\frac{k \Delta z}{2}\right) \tag{2.49}$$

To observe it, we apply a 2-D Fourier transform on time and one dimension of space. We show the result of the Fourier transform of the magnetic field in Figure 2.5.

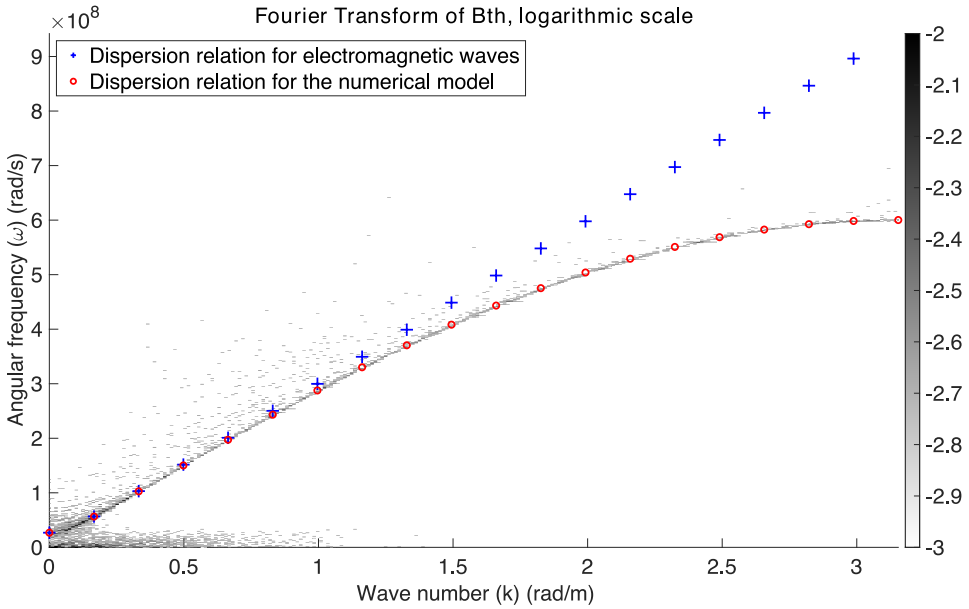

Figure 2.5: 2-D Fourier transform of the magnetic field. The two dimensions used are time and the z coordinate. To obtain the wave number, we averaged the field for each z coordinate on all r. The Fourier transform has been done with 10,000 files each separated in time by 3.34×10^{-9} s. The domain extends along the z-coordinate over 500 m. The plasma frequency $\omega_p = 2.6840 \times 10^7$ rad/s is obtained from the electron density used in this case.

On this figure, we also show the two analytical dispersion relations described above, superposed on the Fourier transform. We can clearly see the effect of the dispersion relation for electromagnetic waves in Figure 2.5 with the plasma frequency as a minimum. We notice a loss of consistency with

the dispersion relation for electromagnetic waves as k increases, as expected owing to the numerical dispersion induced by the FDTD computation. The fact that the observed dispersion relation exactly fits the expected numerical dispersion of the Yee scheme demonstrates the correct implementation of the code [Kilian et al., 2017; Palmroth et al., 2018]. However, care should be taken when interpreting numerical results for higher frequencies (> 50 MHz).

2.3 Remapping of particles

Keeping track of the exponential multiplication of runaway electrons requires to limit the number of super-particles in the simulation. Various techniques have been described in the literature to achieve this goal [Schmalzried et al., 2022]. In the present work, we use a simple resampling technique that we refer to as remapping.

Each super-particle amounts for a certain number of electrons, a property called weight and noted W. When a super-particle of weight W ionizes a molecule, the knocked-off electron is set with the the same weight as the incident particle, and the event can be viewed as "W electrons have ionized a molecule".

When the number of super-particles reaches a threshold number (equal to 10,000 in our simulations), a remapping is performed. It consists in the

merging of pairs of particles with one another, resulting in a particle with a weight equal to the sum of the two merged particles. Of course, such manipulation entails significant loss of information, so it cannot be applied simply by randomly merging any two particles. A sorting of particles must be made before the merging, to minimize the loss of information. Depending on the case, different sorting patterns can be used.

In order to save as much information as possible in the energy space, we use a remapping based on neighbours sorted in energy: we remap groups of particles present in the same grid cell, sorting them by energy in this area. It allows us to preserve to a certain extent information on energy and position.

2.4 Fluid model

Keeping track of the dynamics of electrons over the whole energy range of interest would require significant computational resources. In order to shorten simulation runs, all electrons with energies less than 1 keV and all ions are assimilated into a plasma fluid model. The density of low-energy electrons and ions are calculated from particles using form factors discussed previously. The fluid approach for low energy electrons over the space scales considered in this work is justified by the fact that 1 keV electrons slow down and thermalize over length scales much shorter than

the grid resolution. For example, the continuous slowing down approximation (CSDA) range of a 10 keV electron in ground-level air is only a few millimeters (calculated from the NIST Standard Reference Database 124, https://physics.nist.gov/PhysRefData/Star/Text/ESTAR.html), while the numerical grid used for the fluid model is the same as that used for the PIC code (see previously) that has a resolution on the order of 1 meter.

Secondary electrons are explicitly taken into account in the Monte Carlo code, and their contribution is therefore directly accounted for in the fluid electron density. If produced with energies above the ionization potential of molecules, these secondary electrons could result in more ionization. Thus, they are also considered to contribute to the fluid electron density as a linear function of their energy. Indeed, it is well-known that ionizing electrons loose an average energy of ∼34 eV per electron-ion pairs produced in air (e.g. [Knoll, 2000, Table 5.1, p. 132]), which is approximately constant as a function of energy. Simulations performed with the Monte Carlo code presented here as part of a preliminary work confirm this point. Each electron produced in the Monte Carlo code with energy E lower than 1 keV is thus considered to contribute to an amount of $E/(34\text{ eV})$ electrons and positive ions to the plasma fluid densities.

As the medium is highly collisional, the dynamics of electron and ion den-

sities is considered to evolve according to drift-diffusion equation, as usual in discharge physics (e.g., Bourdon et al. [2007]) and also used in the context of RREAs to simulate the effects of low-energy electrons and ions (e.g., Liu and Dwyer [2013]; Berge et al. [2022]):

$$\frac{\partial n_e}{\partial t} + \nabla \cdot n_e \vec{v_e} = (\nu_i - \nu_a) n_e \tag{2.50}$$

$$\frac{\partial n_p}{\partial t} + \nabla \cdot n_p \vec{v_p} = \nu_i n_e \tag{2.51}$$

$$\frac{\partial n_n}{\partial t} + \nabla \cdot n_n \vec{v_n} = \nu_a n_e \tag{2.52}$$

where n_e, n_n, and n_p are the electron, negative ion, and positive ion densities, respectively; ν_i is the electron-impact ionization frequency, and ν_a is the electron attachment frequency considering dissociative attachment producing a negative oxygen atom O^- (two-body attachment) and a three-body attachment producing a negative oxygen molecular ion O_2^-; and v_e, v_n, and v_p are the electron, negative ion, and positive ion drift velocities, respectively. Because of the magnitude of the densities and the timescales of interest in the present work, we neglect ion-ion recombination, electron-ion recombination, and the diffusion of ions (see [Berge et al., 2022, Section 2.1]). Given the electron densities obtained in the present study, diffusive fluxes of electrons are much lower than drift fluxes over the smallest length scale considered here, which is on the order of one meter. The diffusion term for electrons is therefore also

neglected.

As already noted in previous studies [Dwyer and Cummer, 2013; Berge et al., 2022], the dynamics of low energy electrons and ions is critical to the production of electromagnetic radiation in the LF range. The electron source terms and transport parameters are obtained from Morrow and Lowke [1997] and ion mobilities from Dhali and Williams [1987] (see [Berge et al., 2022, Section 2.1]).

As it removes free electrons over short time scales and produce negative ions that respond to the field over longer time scales than electrons, the electron attachment processes are of prime importance in the system studied. We use the two-body and three-body attachment rates as described by Morrow and Lowke [1997, Appendix]. However, for fields lower than 10^4 V/m at ground-level, the three body attachment given by Morrow and Lowke [1997] reach unphysical values (e.g., in comparison with [Kossyi et al., 1992, Section 2.4]). To avoid this issue and for the sake of simplicity, we cap the three-body attachment frequency at $10^8 N^2/N_0^2$ s^{-1}, where N is the local air density and N_0 is the ground-level density as shown in Figure 2.6.

The electric current density obtained from the fluid equations is added to the current density of computer particles when calculating the evolution of the electromagnetic field (see Section 2.2.2).

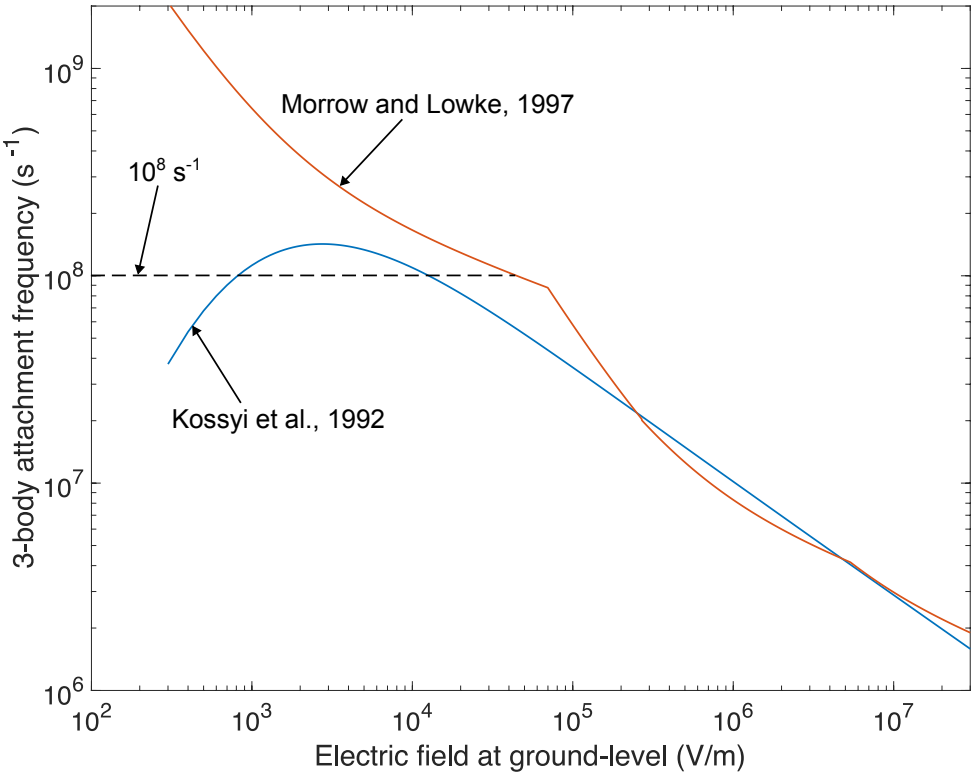

Figure 2.6: Comparison between three-body attachment rates at ground-level as functions of energy obtained from [Morrow and Lowke, 1997, Appendix] (red line) and [Kossyi et al., 1992, Section 2.4, equations (45)-(46)] (blue line). For the latter, the air temperature is chosen as $T = 273$ K and the electron temperature T_e is calculated through the Einstein relation using Morrow and Lowke [1997] diffusion and mobility coefficients at any given electric field. The black dashed line is the value chosen in the model presented here for electric fields below which the value given by Morrow and Lowke [1997] exceeds it.

2.5 Domain boundaries

The domain boundaries are, depending on the case, either conducting walls or periodic. The periodic boundary conditions are used in the test cases, when we only use the PIC part. The conducting boundary condition is one of the simplest, that is implemented simply by considering the electric and

magnetic fields equal to zero at the boundaries. It brings several issues, as the electromagnetic waves bounce on these boundaries, leading to non-physical effects if we let the simulation run for too long. However it remains negligible as long as the bouncing EM wave has not reached the RREA, which allows us to observe the electron avalanche for relatively long durations.

Chapter 3

Constraints on avalanche parameters

Contents

In order to study in depth the RREA, the self-consistent effects it is submitted to, and try to decipher its production mechanism, in this chapter we describe several simulations made with the self-consistent code. All simulations are made at an altitude of 12 km, with no variations of the air density and related parameters throughout the domain. In all simulation cases presented in this chapter, the electrons are injected at a given location (around the (0,0) point of the domain). The first section presents the results of two simulations

made without the photons fully described as particles, instead replaced by an averaging braking force (coming from the bremsstrahlung) slowing the electrons. The second section discusses the saturation observed in the simulation. The third section will focus on the number of electrons observed, showing and discussing the results of several simulations to study the stabilization observed in section 1.

The results presented in this chapter have been presented in Gourbin and Celestin [2024b] and Gourbin and Celestin [2024a].

3.1 First results

In this section, we present the results of simulated avalanches inside an homogeneous electromagnetic field over the whole domain. Two main cases are considered:

- In the first case, 1000 particles are initially injected with a weight of 10^8 each.

- In the second case, one particle of energy 1 MeV is injected in the starting area every 1000 timesteps. Each particle initially has a weight of 10^5 electrons. The injection rate is therefore about $\sim 3 \times 10^5$ electrons per nanosecond. The simulation initially begins with 10 particles, representing 10^6 electrons.

Since the observations made in both cases are similar in many ways, we focus more on the second case, as it is a bit more realistic: considering the leader based mechanism, we expect to have an important amount of electrons being injected over a short period of time inside the acceleration region. The first case is still used to point out some observations made, as some aspects of the simulations are clearer on this one. Nevertheless, since the model is the same in both cases, the mechanisms pointed in one ought to be present in both. The figures presenting the result of the initial injection case are in Appendix A.

The initial positions of electrons, for both cases, being electrons injected initially or continuously during the simulation, is randomly assigned onto a hemisphere of radius of 42 m at $z = 0$ m and $r = 0$ m. We set their initial energy at 1 MeV, their speed is computed from the energy and they are assumed to all go initially in the z-direction. As the avalanche propagates, it will be centered on the z-axis. The timestep is $\Delta t \simeq 3.40.10^{-13}$ s. For both cases, the background electric field is 1.1828×10^5 V/m (∼5 kV/cm at ground level), and homogeneous over the whole the domain.

For the sake of simplicity, we do not consider the production of photons and positrons explicitly in the present work. Phenomena associated with relativistic feedback [Dwyer, 2003] are therefore not included. Under the electric

field applied here (5 kV/cm at ground-level), relativistic feedback should have significant effects beyond a distance of $\sim$ 1200 m (at 12 km) [Dwyer, 2003; Skeltved et al., 2014]. However, for a closed system like in our configuration, it seems that this electric field magnitude would correspond to a distance of $\sim$4000 m [Pasko et al., 2023], which is close to the size of our simulation domain. Additionally, it is likely that the effects of relativistic feedback would not be significant over the relatively short timescales used in this study. It is also worth noting that the effect of a continuous injection of primary electrons are not unlike the effects of the production of new avalanches by photons and positrons. Similarly to the relativistic feedback, the continuous injection introduces another timescale to the system, additionally to that associated with RREA processes.

Figure 3.1 shows the electron energy distribution for the second case. The energy spectrum is consistent with the expected energy distribution in a RREA [e.g., Dwyer et al., 2012], and remains so throughout the simulation. Using a fitting procedure we find that the exponential cut in this case is at $\sim$7 MeV.

3.1.1 Low-energy electron density

The evolution of low-energy electron density (i.e., the electron density handled in the fluid approach) is shown Figure 3.2 and Figure 3.3 .

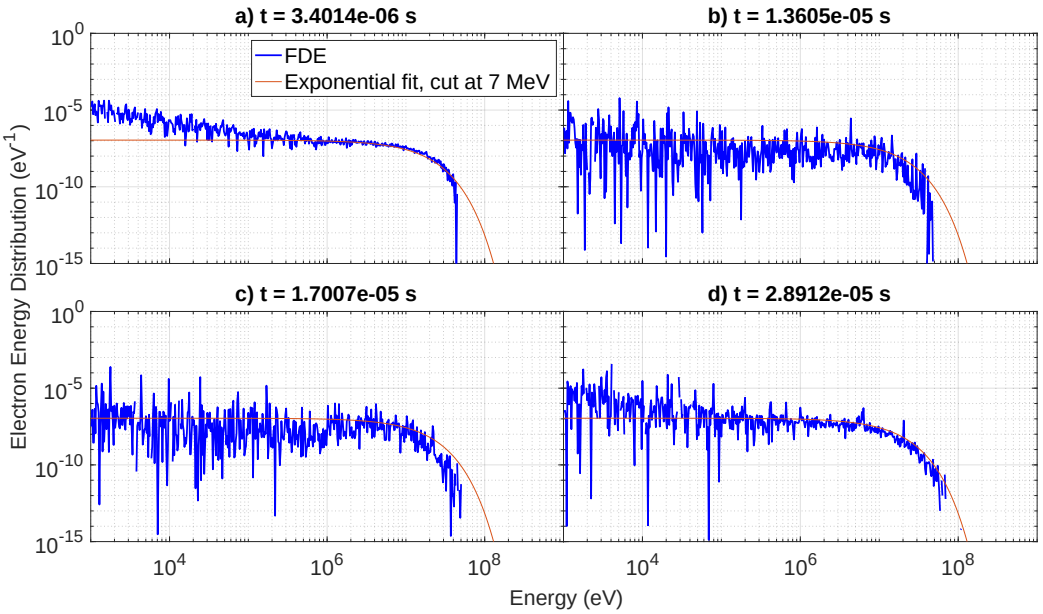

Figure 3.1: Energy distribution of the electrons above 1 keV, smoothed using a mean over 3.4014×10^{-7} s (i.e. 10 files), for a simulation with continuous injection of all the electrons.

During the first part of the propagation, the avalanche increases in density rapidly, while expanding slowly, following a typical diffusion trend (proportionally to $\sqrt{z}$) (panels **a** and **b** of Figure A.1 and A.2, and panel **a** of Figure 3.2 and 3.3). At a certain point in time, the electron avalanche reaches a critical density of approximately 10^{15} m^{-3} (panel **c**), and from which the electron density stops increasing, and the avalanche front starts expanding rapidly (panel **d**).

Once this saturation is reached, the continuous flux of electrons seems to come to a stop when arriving to the point where the density reaches saturation. We will see that it is due to the screening of the electric field in the avalanche

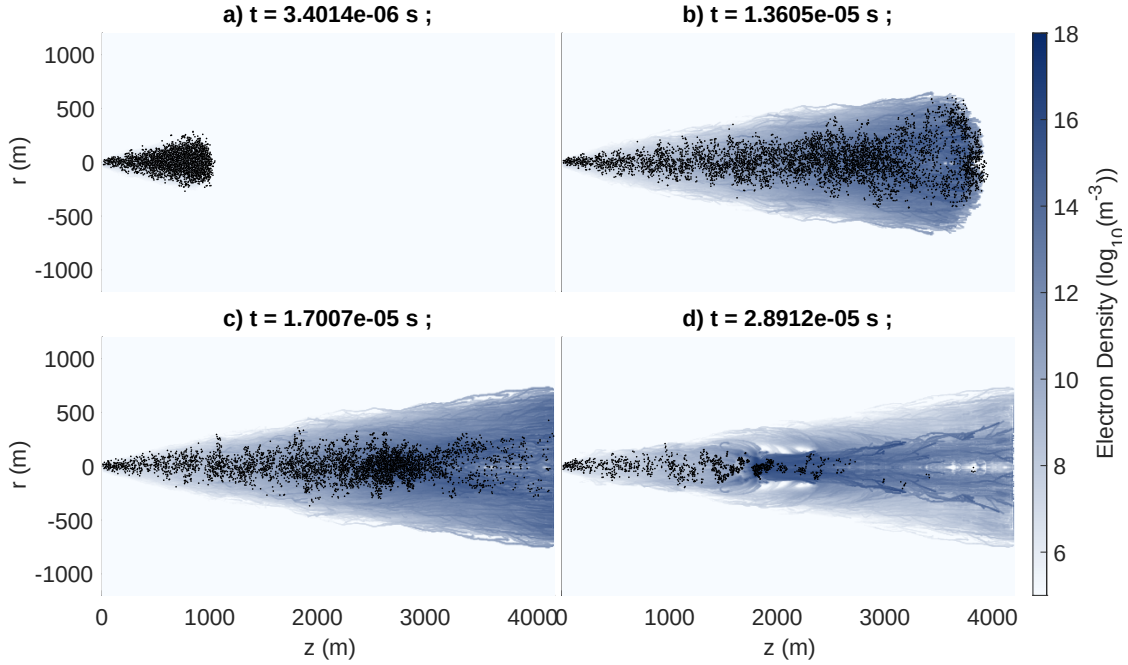

Figure 3.2: Cross-sectional view of the low-energy electron density at different moments of time (presented here in decimal logarithm). Simulation with a continuous injection of particles. Decimal logarithm of the density field of electrons and high-energy electron positions (black dots) are shown. The r-axis has been doubled for clarity. Because of that, each particle appears twice: at its original position and at its symmetric position about the z-axis.

trail. Because of that, electrons are agglomerating near the axis. Moreover, the density starts increasing beyond the previously observed limit, and form a structure that starts "propagating" backward on the trail of the avalanche.

We also notice on the right side of the avalanche (closer to the front), where no electron manages to reach, that the density starts decreasing. This can be more clearly seen in the initial injection case, on Figures A.1 and A.2 (Appendix A): after the high-energy electrons ionized the domain, the low-energy electron density starts decreasing. We have verified it is mainly due to

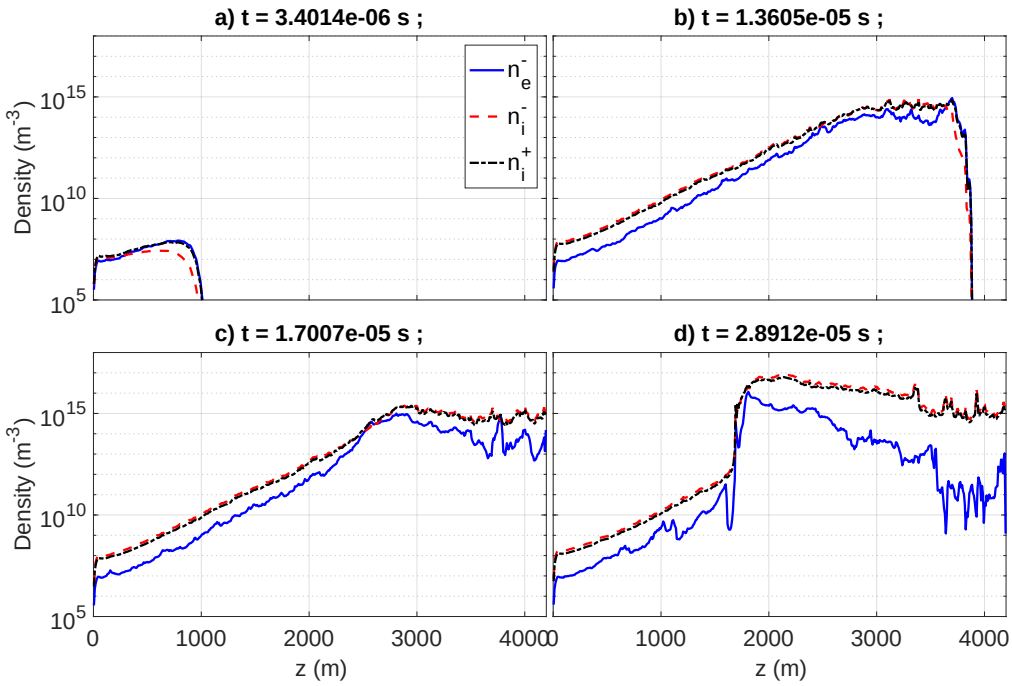

Figure 3.3: Electron and ion densities along the z-axis at different times for continuous injection (the densities shown in this figure are averaged in the r-direction between $r = 0$ m and $r = 67.2$ m). The time passed since the beginning of the run is indicated above each plot. The blue, red, and black line represent respectively the density of electrons, negative ions and positive ions.

the 3-body attachment process.

3.1.2 Electric field

The evolution of the electric field on the z-axis (in the center of the avalanche) is shown in Figure 3.4. This figure shows the values of the different components of the electric field, as well as the position of the energetic electrons (>1 keV), which gives us an approximation of the position of the avalanche front. Once the avalanche has reached saturation, we observe that the electron density is sufficient to quickly screen the electric field out at the front

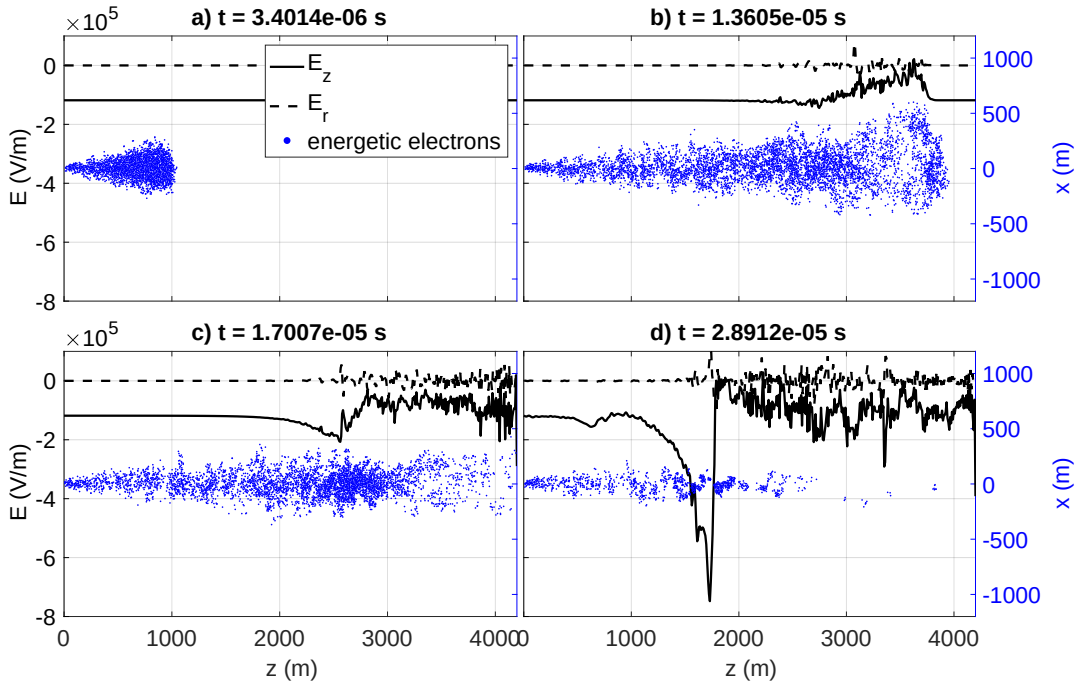

Figure 3.4: Electric field near the axis $r = 0$ m (center of the avalanche) at different times for a simulation with continuous injection. The r and z component of the electric field are shown as a function of z, as well as the (x, z) particle coordinates. E_z is shown on the axis, E_r is shown at $r = 8$ m.

(panels **c** and **d**). However, the depletion of the electron population due to the attachment cancels partially this effect, allowing the remaining electric field to still accelerate the electrons behind the front, which explains the groups of electrons still propagating there. We also observe the formation of a peak in the electric field at the position where the avalanche saturation was reached (around 1800 m), negative for E_z (panel **c** of Figure 3.4). The peak then starts moving backward (panel **d**). As it is a peak in the negative of the z-component of the field, it accelerate the electrons, which gain energy in this moving structure. This peak keeps increasing as the structure propagates

backwards, and screens the electric field in its trail.

3.1.3 Number of high-energy electrons

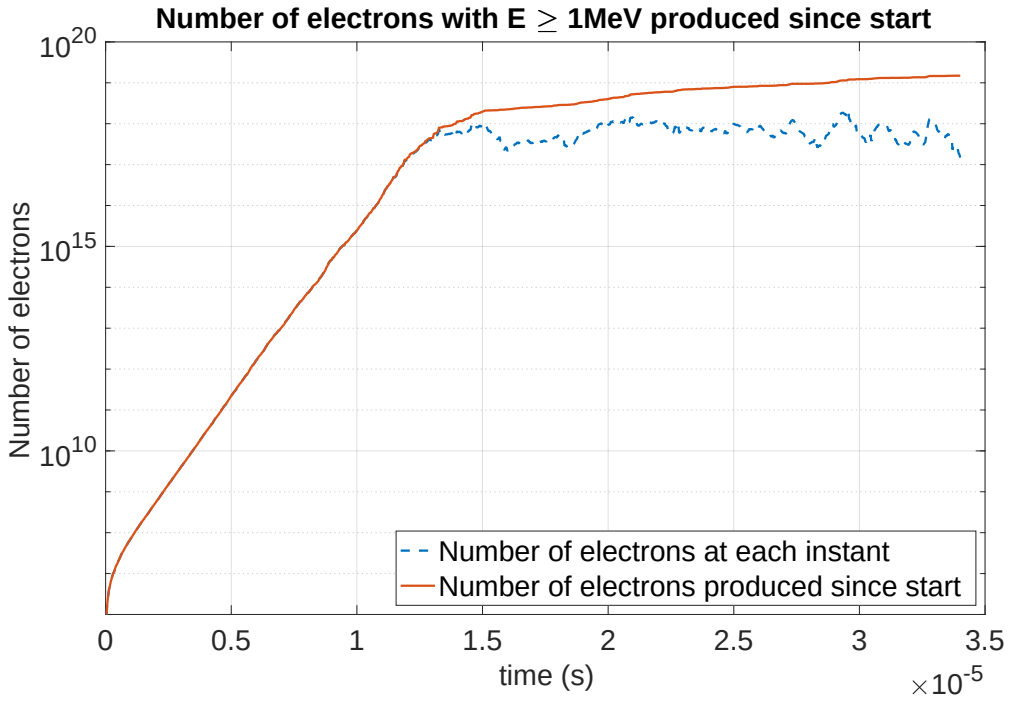

Figure 3.5: Number of electron with an energy higher than 1 MeV as a function of time, for the simulation with continuous injection.

The number of high-energy electrons can be seen in Figure 3.5. The number of electrons seems to slow its increase after a time. Comparisons with the profile of electron density (Figure 3.3) show that the change of behavior happens around the same time the avalanche saturates. It is interesting to see this behavior while electrons still are continuously injected into the domain. And so, we can determine the number of bremsstrahlung photons emitted by these electrons using equation (4) from Celestin et al. [2015] :

$$N_\gamma = \int_0^{+\infty} N_e(t)\langle\nu_\gamma\rangle(t)dt \tag{3.1}$$

where N_γ is the number of photons produced, $N_e(t)$ the number of electrons as a function of time, and $\langle\nu_\gamma\rangle(t)$ the photon production frequency per electron. At the end of the simulation, we obtain for this simulation 1.4295×10^{18} photons above 1 MeV produced, which is on the order of the expected number of photons in a TGF [Celestin et al., 2015, Table 1].

3.1.4 Electric Current

The current produced by the avalanche can be separated into two components:

- The conduction current, which corresponds to the current produced by the movement of electrons and other charged particles in time. It is computed as part of the current assignment procedure using the Villasenor scheme.

- The displacement current is produced by the variation of the electric field in time, and computed using the following formula:

$$\mathbf{j}_D = \varepsilon_0 \frac{\mathbf{E}^n - \mathbf{E}^{n-1}}{\Delta t} \tag{3.2}$$

where $\mathbf{j}_D$ is the displacement current, $\mathbf{E}^n$ and $\mathbf{E}^{n-1}$ are the electric field at time t^n and t^{n-1}, Δt the timestep and ε_0 the vacuum permittivity.

The current is plotted in Figure 3.6. We can see that at the front, both current components seems to be roughly equal to one another (one being positive and the other negative, which explains why the total current is of the order of 10^{-5} A). We notice that the displacement current is modified ahead of the avalanche. It is to be expected, as the electrons travel less than the speed of light, while electromagnetic waves travel at c. The fluctuation induced here is however too weak to have a visible effect on the electric field plot.

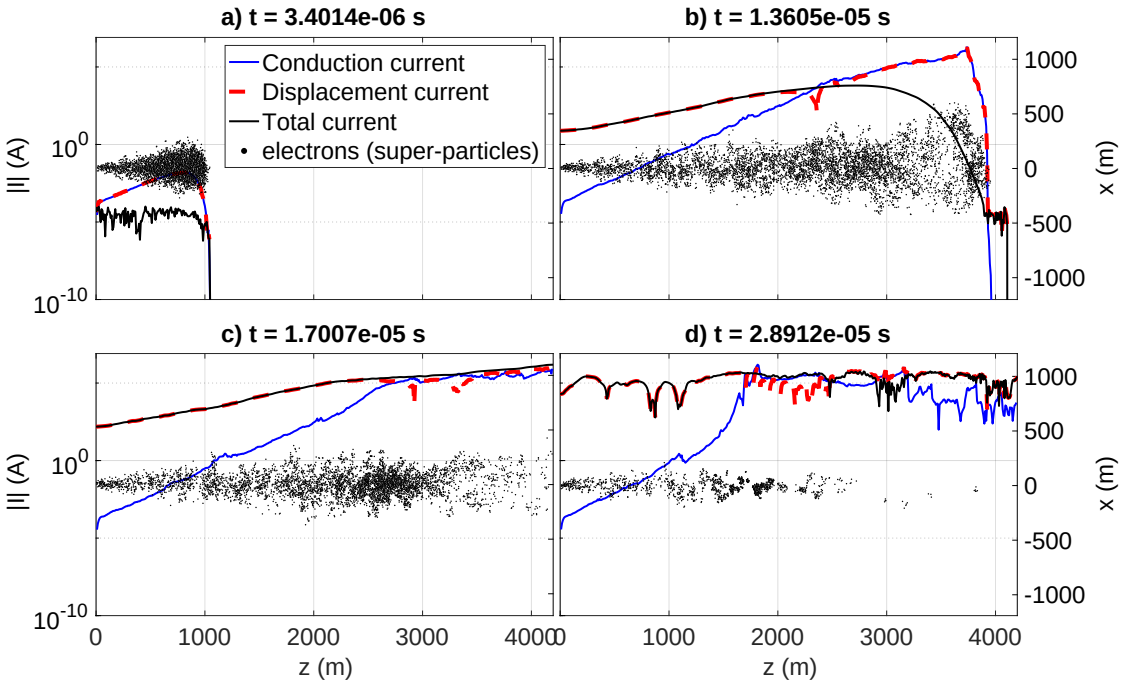

Figure 3.6: Absolute value of the total electric current and its components (conduction and displacement) produced at different moments of time for the case with a continuous injection.

Behind the avalanche front, attachment reduces the electron population, so the conduction current starts decreasing. It is however more visible in the

initial injection case, where no electron flux comes to sustain the conduction current (panel **c** and **d** of Figure A.6).

In this simplified simulation, the total current reaches values above 10^5 and even up to 10^6 amperes. Using a different model, Berge et al. [2022] showed that slow LF pulses reported by Pu et al. [2019] would correspond to peak current of ~ 100 kA.

The rise in displacement current appearing from the left of the domain occurs after the rebound of the initial electromagnetic wave on the radial boundary and is believed to be a numerical effect, as it appears when the electromagnetic wave induced by the first electrons launched inside the domain reaches the boundaries of our domain. However, it is important to precise that no effect has been observed whatsoever, being in the electric or magnetic field. All the effects described above in the electric field are explained by the physics of the problem. The displacement current is computed from the variation of the electric field in time, and in this case is provoked by the returning wave from the border that, while insignificant compared to the background electric field, occurs over a very short period of time, which lead to a misleadingly high displacement current.

This current still might have an effect on the induced magnetic field via the Maxwell-Ampere equation. On Figure 3.8, we can see that the radiated

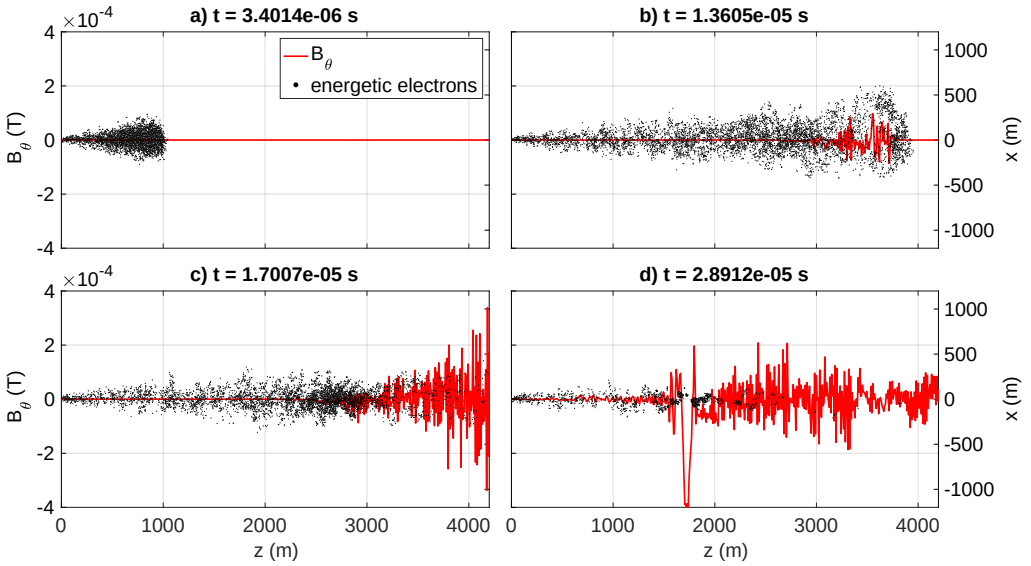

Figure 3.7: Induced magnetic field near the axis (inside the avalanche) computed from Maxwell Ampere equation, at different times of the simulation using continuous injection.

current reaches $\sim 1\ \mu$T. However, if we look at the induced magnetic field on Figure 3.7, we can see that it yields values going up to $\sim 100\ \mu$T. If we compute the cyclotron frequency of such field, we obtain $\frac{qB}{m} = 1.76 \times 10^7\ \text{s}^{-1}$. We compare it to the collision frequency, knowing that the timestep is defined by the highest collision frequency, we then obtain $\frac{1}{\Delta t} = 2.94 \times 10^{12}\ \text{s}^{-1}$. From that, we can conclude that an electron propagating in our domain will have had time to interact quite a number of time before feeling the effect of the magnetic field, and by then the numerous deviations will have made this effect irrelevant. We can then affirm that, although the displacement current seems to be significant, on the timescales considered, it does not have any significant effect on the avalanche.

3.1.5 Radiated field observed at a distance

We can compute the magnetic field at a horizontal distance $R = 150$ km from the point of emission, considering an antenna of height $H = 300$ m, using equation (7) from Uman et al. [1975] :

$$B_\phi(D,t) = \frac{\mu_0}{2\pi}\int_0^H \frac{\sin\theta}{R^2} i(z, t - R/c)dz + \frac{\mu_0}{2\pi}\int_0^H \frac{\sin\theta}{cR}\frac{\partial i(z, t - R/c)}{\partial t}dz \quad (3.3)$$

where $i(z, t - R/c)$ is the conduction current. Here, θ is considered to be equal to $\pi/2$ (hence $\sin\theta = 1$).

The two integrals of the equation are plotted in Figure 3.8, and labelled respectively the magnetostatic field and radiation field. When calculating the magnetic field at a distance from the electric current using Uman et al.'s equation, Berge et al. [2022] used the total current. Upon further inspection, only the conduction current should be included in Uman et al.'s integrals as per use of Lorenz retarded potentials [see also Shao, 2016]. We can estimate that the error caused by this oversight on the magnitude of the magnetic field reported by Berge et al. [2022] is ∼20%.

Since the ambient electric field is strong, homogeneous and infinite in the simulation, the form of the magnetic field is not expected to resemble the magnetic field associated with a TGF. We also note that the value reached by the magnetic field is far too high compared to measurements of slow LF

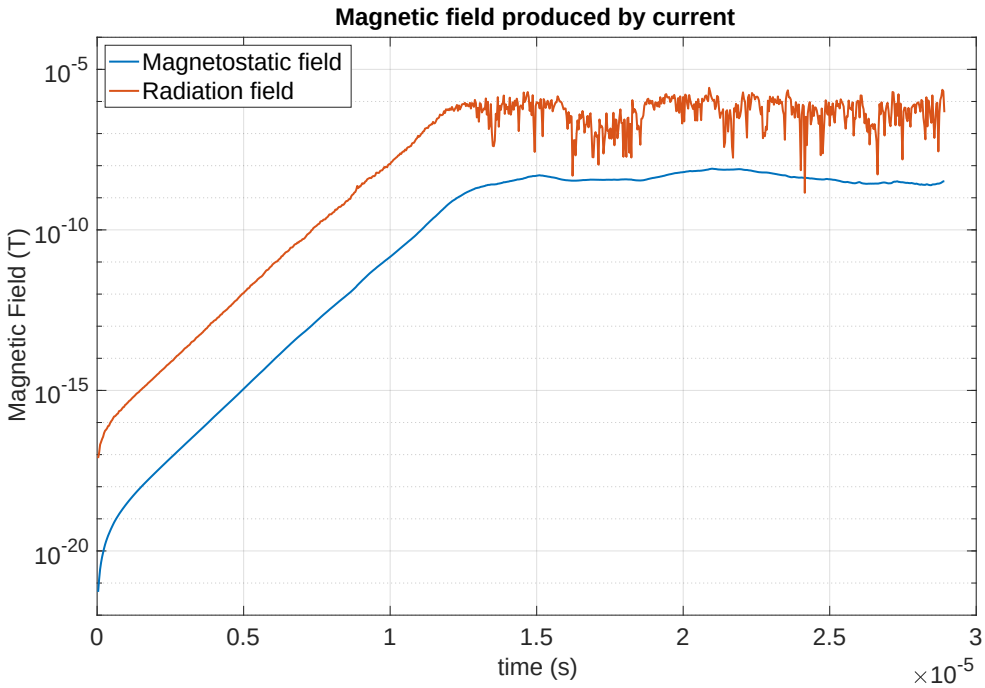

Figure 3.8: Magnetic field computed from the current, using equation (7) from Uman et al. [1975]. The radiation and magnetostatic parts of the magnetic field shown here correspond to the two integrals in that equation. The computation is made for a distance from the source of 150 km, for the case with continuous injection.

pulses [e.g., Pu et al., 2019]. It is however consistent with the current values presented in the previous section.

3.2 Saturation of the low-energy electron density

In both configurations studied, the saturation of the electron density can be explained by the increase of conductivity associated with a RREA. In the beginning, the increase in the electron and ion densities is controlled by the runaway electron avalanche and characterized by the avalanche time, while the relaxation of the electric field is related to the conductivity in the medium

through the Maxwell time. The latter also characterizes the time scale of the defocusing of a charged particle beam through Coulumbian repulsive forces. When the conductivity, driven by the low-energy electron density reaches a magnitude such that the Maxwell time approaches and exceeds the avalanche time, the field collapses faster than the time it takes for an avalanche to increase the density.

These two times are defined as followed:

$$\tau_{RREA} = \frac{\lambda}{V_{e^-}} \tag{3.4}$$

$$\tau_M = \frac{\varepsilon_0}{q_e \mu_e n_e} \tag{3.5}$$

where λ is the characteristic avalanche e-folding length, V_{e^-} is the electron speed, q_e is the electron charge, μ_e is the electron mobility, and n_e the electron density. Equalling those two timescales, we can thus find the density at which the Maxwell time reaches the avalanche time:

$$\begin{aligned} & \tau_M = \tau_{RREA} \\ \Rightarrow \quad & \tfrac{\varepsilon_0}{q_e \mu_e n_e} = \tau_{RREA} \\ \Rightarrow \quad & n_e = \frac{\varepsilon_0}{q_e \mu_e \tau_{RREA}} \end{aligned} \tag{3.6}$$

The term τ_{RREA} depends on the characteristic avalanche length λ, which itself depends on the electric field. For example, it can be found by using the

equation (2.3) in Dwyer et al. [2012]. We can also use our simulation results by plotting the theoretical increase in density for a given λ and compare it to the increase in the ion density in our simulation (before saturation) or to the peak of the electron density at different moments of time, as the electron density has a faster dynamics due to the attachment processes.

The electron density and the theoretical density are shown in Figure 3.9. Note that we are using the initial injection case here: because all the electrons are initially injected at once, and that no electrons comes after to produce something behind, the rise in the density is clearer, easier to fit, and the saturation is also more visible, as the backward propagating structure does not appear for this case.

For this simulation, we obtain a good fit for $\lambda \simeq 165$ m. The speed is assumed constant at $V_{e^-} = 0.89c$ [Coleman and Dwyer, 2006], with c the speed of light, so $\tau_{RREA} = 3.779 \times 10^{-8}$ s. We also have $\mu_e = 0.2719$ m^2/(V.s) [Morrow and Lowke, 1997] ; $q_e = 1.602 \times 10^{-19}$ C, and $\varepsilon_0 = 8.854 \times 10^{-12}$ F/m. It yields a saturation density $n_{\text{th}} = 3.2806 \times 10^{14}$ m^{-3}.

As shown in Figure 3.9 and 3.10, the observed saturation density is in good agreement with our computed value.

Following equation (3.6) the low-energy electron saturation density can be calculated for various electric field. The result is shown in Figure 3.11.

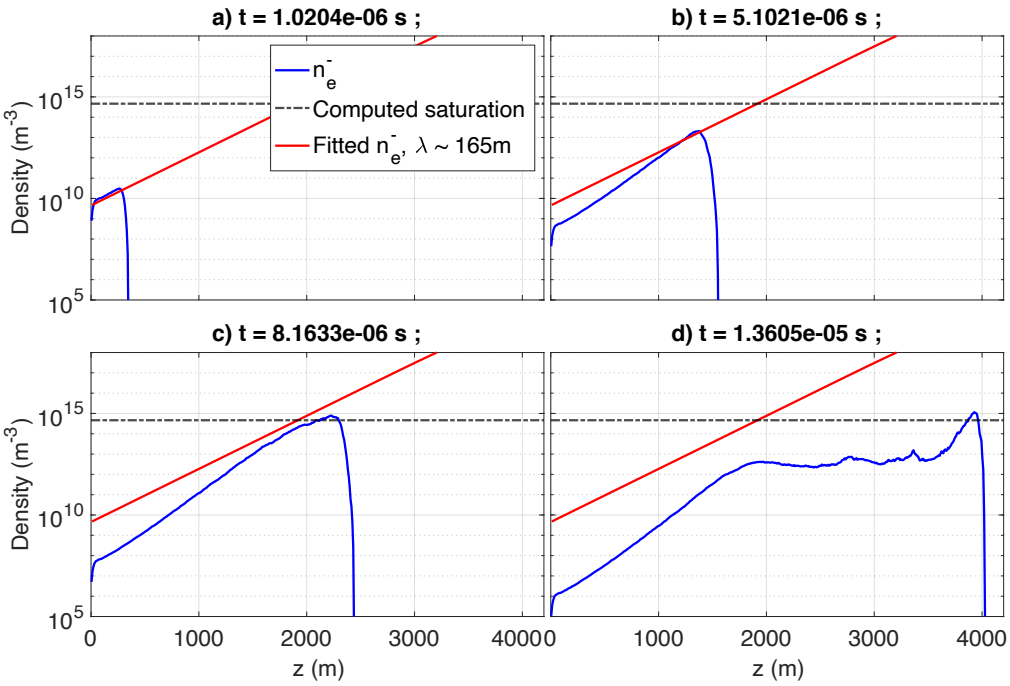

Figure 3.9: Electron density relative to position for initial injection (blue), and fitted density profile (red). The dash-dotted line is the saturation density computed with equation 3.6.

In the cases studied in the present chapter, the low-energy electron saturation density is reached at $\sim 3 \times 10^{14}$ m^{-3} while the runaway electron density is about four orders of magnitude lower, reaching $n_{\mathrm{r,s}} \sim 10^{10}$ m^{-3} at 12 km. It is expected that this runaway electron saturation density would follow a similar trend as the low-energy electron saturation density shown in Figure 3.11, and their order of magnitude (at 12 km) would hence not change significantly in realistic fields present in streamer zones of negative leaders.

In the conditions of the simulations presented here, the saturation of the RREA occurs when the number of runaway electrons is close to that expected

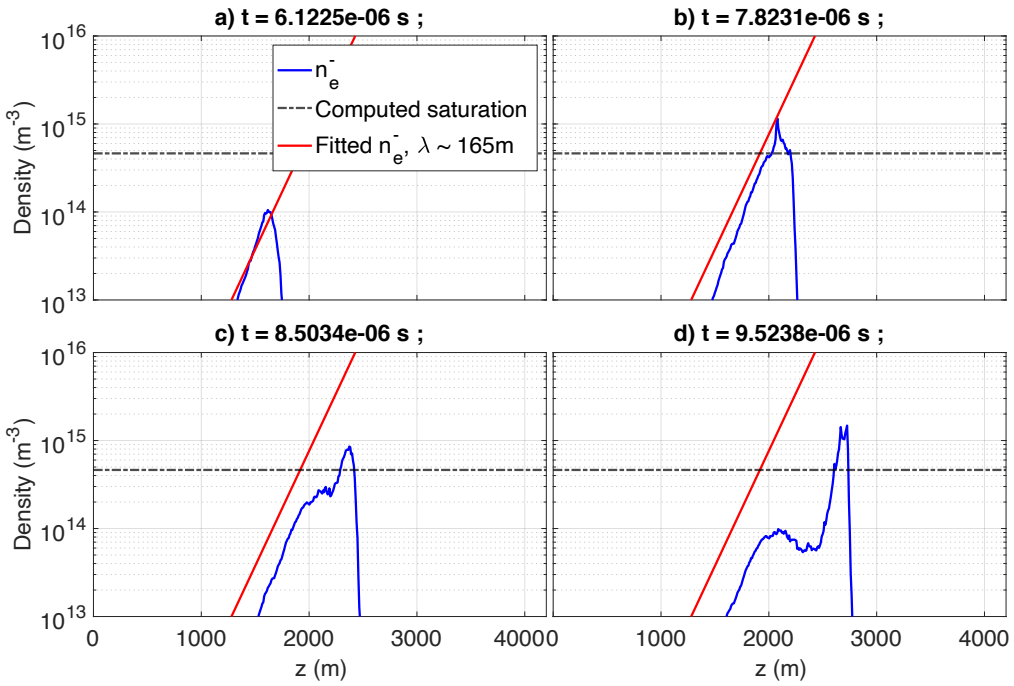

Figure 3.10: Zoom in density of Figure 3.9, and time-centered around the moment the saturation is reached.

in TGFs ($\sim 10^{18}$) and the growth of this number strongly slows down after that point (see Figure 3.5, and Figure A.5 for the initial injection case). This total number of runaway electrons is related to the radius of the avalanche when saturation is reached. Considering that saturation is reached at the source of TGFs, resulting in the collapse of the electric field, and assuming the number of runaway electrons involved in the TGF production as 10^{18}, the size of the avalanche should be on the order of $R \sim \left(\frac{3}{4\pi}\frac{10^{18}}{n_{\mathrm{r,s}}}\right)^{1/3} \sim 500$ m at 12 km.

We note that the balance between the avalanche time and the Maxwell time leading to a saturation of the electron density is reminiscent of streamer discharges in which a stable balance between the Maxwell time and the ion-

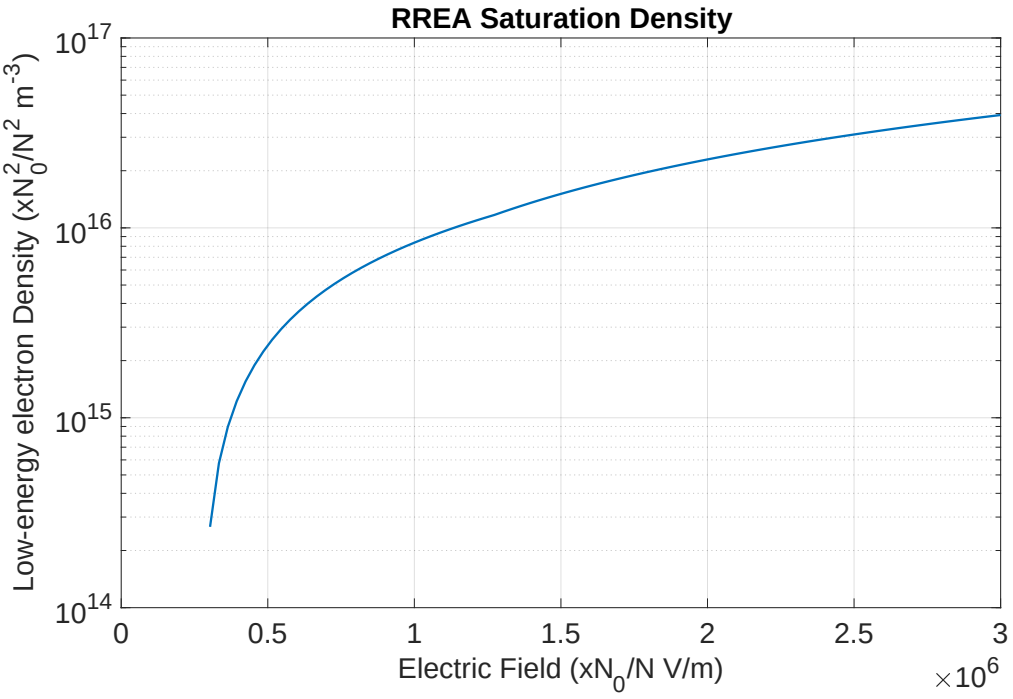

Figure 3.11: Saturation density as a function of the ambient electric field derived from equation (3.9). In the axis' legends, N stands for the local air density and N_0 stands for the air density at ground-level.

ization time is present in the streamer head for similar reasons [e.g., Wang and Kunhardt, 1990].

This saturation mechanism is different from that reported by Luque [2014] using a 1-D electrostatic model of a RREA. In particular, here the saturation in produced by the increase of the conductivity caused by the strong production of low-energy electrons by the RREA, and not by the effect of the runaway electrons on the field. In our simulations, the latter indeed carry much less charge density than secondary electrons.

In the case of a continuous injection, the backward-propagating structure

after the front explosion also follows an electric pulse, saturates the electron density in its wake, and screens the electric field behind it. The structure resembles that obtained by Liu and Dwyer [2013] and named relativistic feedback streamer. It is unclear the case presented by Liu and Dwyer [2013] also reached saturation. They indeed obtained ion densities on the same order of magnitude as that reported here, but the runaway electron density seems to be lower.

Those results could also be important in the context of lightning propagation, as RREAs seem to be able to produce significant densities in the vicinity of lightning discharges. For example, Bourdon et al. [2010] have shown that streamer discharge propagation is greatly influenced by the background electron density.

3.3 Constraining the number of electrons produced

As mentioned before, the saturation of electron density lead to another phenomenon: the limitation of the number of electrons.

Several articles [Dwyer and Smith, 2005; Gjesteland et al., 2015; Mailyan et al., 2016, 2019; Lindanger et al., 2021] place the number of electrons for the brightest TGFs between 10^{17} and 10^{19}, which is within the range of where we stand with our simulation. Several things could have an impact on the

number of high-energy electrons at the end of our simulations. For instance, the electric field has an impact not only on avalanche multiplication, but also on the dielectric relaxation time, that has been shown to cause the saturation of the low-energy electron density.

To better understand the phenomenon limiting the number of high-energy electrons, we decide to perform a series of self-consistent simulations, in a domain with a higher electric field but on a shorter length, recreating to an extent the conditions for avalanche inception in a streamer corona.

The work presented here is presented in Gourbin and Celestin [2024a].

3.3.1 Parameters of the simulations

The simulation domain in which the simulated avalanche propagates is cylindrical, axisymmetric for the electromagnetic field, with a height of 3 km and a radius of 1.2 km. The bottom part of the domain is subjected to an electric field of $16 \times \frac{N}{N_0}$ kV/cm, with N_0 the density of air at the ground and N the density of air at an altitude of 12 km, the altitude we chose for all the simulations. We refer to this zone as the acceleration zone. The electric field is set to zero for $z > 400$ m, making the zone between $z = 400$ m and $z = 3$ km a zone with no electric field initially, where electrons can still propagate, interact with the air, and influence the electromagnetic field around them. Seed electrons are injected continuously at a constant rate near the (0,0) point of

our domain, in the acceleration zone, through a section of radius 42 m. These seed electrons can be thought of as thermal runaway electrons injected by a lightning leader [e.g., Celestin et al., 2015] or relativistic-feedback-produced electrons [e.g., Dwyer, 2003]. The injection rate is a variable parameter between the different simulations. The different injection rates are listed in Table 3.1. The cases last long enough so that the avalanche reaches the end of the

Table 3.1: Electron injection rates used in the simulations

Injection rate (electrons/s)
2.94×10^{13}
2.94×10^{14}
2.94×10^{15}
2.94×10^{16}
2.94×10^{17}
2.94×10^{18}
2.94×10^{19}
2.94×10^{20}
2.94×10^{21}

acceleration zone and propagates beyond that point.

3.3.2 Results

The low-energy electrons densities can be seen Figure 3.12, where the various runs stopped at 1.7 μs, showing different stages regarding the RREA saturation state: The cases with an injection rate below 2.94×10^{17} electrons per second do not reach saturation before the end of the acceleration zone. The case with an injection rate of 2.94×10^{18} el/s is close to reaching it, and starts to display the backward propagating structure, between 200 m and 300 m.

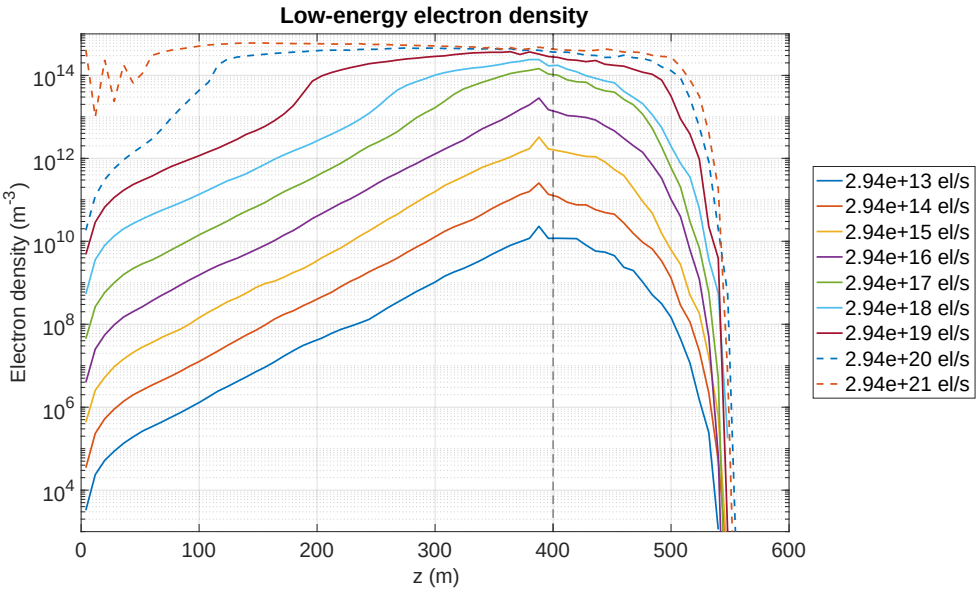

Figure 3.12: Low-energy electron density profile for different injection rates at the end of the simulations (t = 1.67 μs).

The three cases with higher injection rates all reach saturation before the first injected electrons leave the acceleration zone, and display different dynamics.

The number of high-energy electrons and resulting number of photons as a function of time is shown in Figure 3.13. In panel (a), we see the number of high-energy electrons in the simulation domain ($\geq$ 1 MeV) as a function of time.

For the cases with an injection rate below 2.94×10^{17} el/s, the number of high-energy electrons stops increasing when the avalanche reaches the electric field cut as the system reaches a steady state. When they arrive at this point, the electrons at the front quickly decelerate and lose all their energy. The maximum number of high-energy electrons thus only depends on the incoming

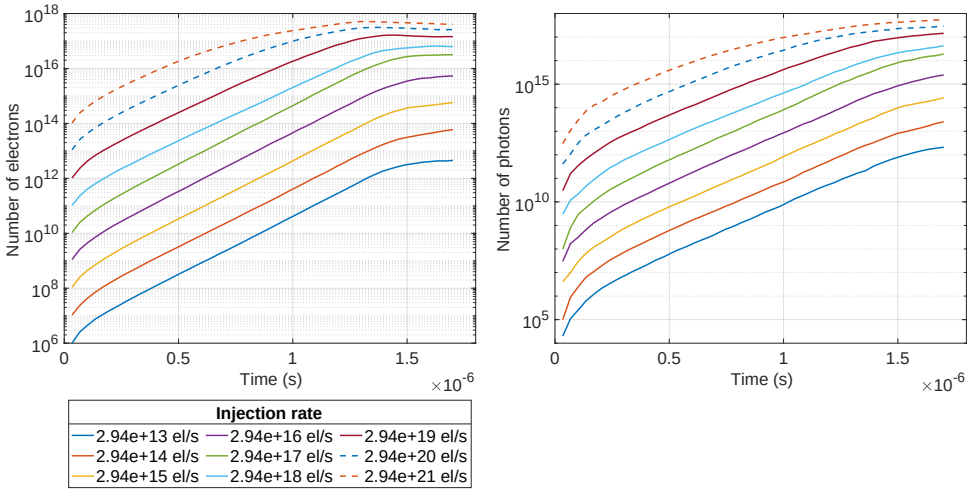

Figure 3.13: *Left*: Number of high-energy ($\geq$ 1 MeV) electrons as a function of time for different injection rates. *Right*: Number of photons ($\geq$ 1 keV) as a function of time for different injection rates.

flux and electrons produced throughout the acceleration zone.

For the cases with the three highest injection rates, we see that the number of high-energy electrons stabilizes before reaching the end of the acceleration zone. As seen in the previous section, this stabilization is caused by the mechanism of saturation and the associated collapse of the electric field, which constrains the number of electrons. An interesting feature is that, for these three cases, the number of high-energy electrons all lay between 10^{17} and 10^{18}, while the non-saturated cases all reached different magnitudes at the end of the simulations proportionally to the injection rate.

The right panel of Figure 3.13 shows the number of photons with an energy greater than 1 keV as a function of time for the different cases. While the

curves are slightly different from the number of electrons, they follow a similar pattern: the non-saturated cases show a slowdown of the photon number at different magnitudes proportionally to the injection rate, while the saturated cases all lay between 10^{17} and 10^{18} photons for an increase in the injection rate by two orders of magnitude. In Subsection 3.3.3, we argue that despite the different expected timescales and processes at play in real TGFs, a similar maximum number of high-energy electrons and photons to those in the saturated cases would be reached.

3.3.3 Constraints on the number of electrons

In all saturated cases, the number of energetic electrons and photons stabilizes around the same order of magnitude. In our simulations, this order of magnitude is near $10^{17} - 10^{18}$. This dynamics can be better viewed on Figure 3.14, where the number of high-energy electrons and photons at the end of simulations are shown as a function of the number of injected electrons. A break of the linearity of the system can be seen for cases reaching saturation (injection rates $> 3 \times 10^{17}$ el/s): while the number of high-energy electrons and photons at the end still slowly increase with the number of injected electrons, the increase is slowed down much more significantly, reaching for 5×10^{15} injected electrons, 4×10^{17} high-energy electrons at the end of the simulation.

The number of high-energy electrons can be compared with the estimates

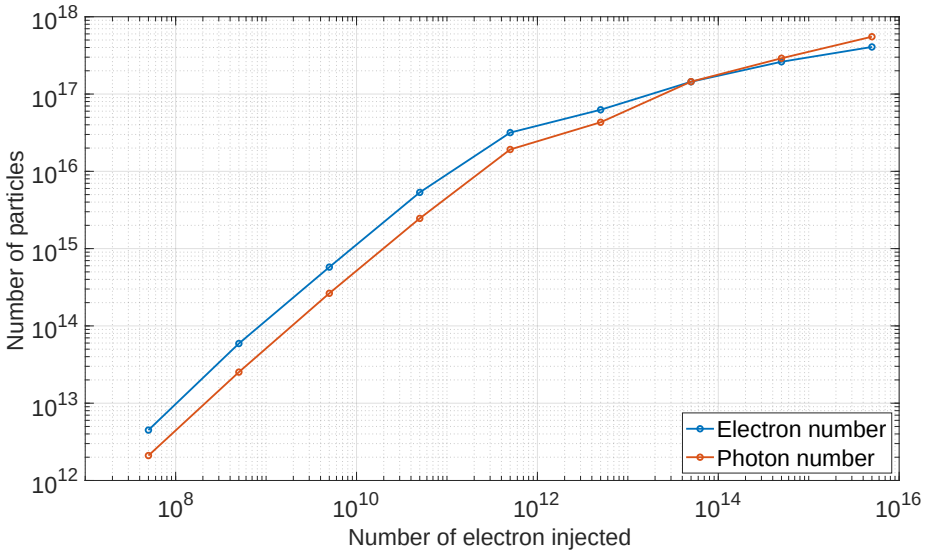

Figure 3.14: Number of electrons and photons at the end of the simulations as a function of the number of electrons injected in the domain throughout the duration of the simulations.

deduced from TGF observations (e.g., [Mailyan et al., 2016, Figure 8], [Mailyan et al., 2019, Figure 9]), where the number of high-energy electrons after propagation is evaluated as mainly between 10^{17} and 10^{19}, with almost none beyond 10^{20}. This seems to match well with the results of our saturated cases, where the electron number stagnates between 10^{17} and 10^{18}, especially considering that those articles use very bright TGFs (i.e., bright enough to allow individual spectral analysis).

While the first simulations presented at the beginning of this chapter can be considered as test cases, made with parameters favourable to the development of avalanches, the physical parameters used in this section are not unrealistic. For instance, the magnitude of the electric field and the length of

the acceleration region are close to those expected to be present in streamer zones of negative leaders [e.g., Raizer, 2000] in positive intracloud discharges (+IC) forming an electric potential drop of ∼300 MV [Celestin et al., 2015]. In such configuration, the amplification factor in the number of high-energy electrons is about 10^6 (e.g., see Figure 3.13), which results in the establishment of a RREA spectrum [Celestin et al., 2015].

In the present work, the magnitudes of the injection rates have been chosen to demonstrate both linear ($< 3 \times 10^{17}$ electrons/s) and saturation ($> 3 \times 10^{17}$ electrons/s) regimes. In the latter cases, RREAs lead to a quenching of the electric field over the timescale of the simulation ($\sim$ 1.6 μs) while the former cases are expected to quench the electric field over longer timescales (see below). In reality the typical total duration of TGFs as observed from space is closer to ∼100 µs with rise times of a few tens of microseconds [e.g., Fishman et al., 2011; Foley et al., 2014; Xu et al., 2019; Lindanger et al., 2020]. For the sake of simplicity, one can consider 15 μs as a characteristic timescale for the rise of the TGF source as derived from radio observations [e.g., Pu et al., 2019; Berge et al., 2022].

For a total number of high-energy electrons of $\sim 10^{17}$ in a TGF [e.g., Dwyer and Smith, 2005], considering an amplification factor of 10^6 and a rise time of ∼15 μs, the initial injection rate can therefore be considered to be on

the order of $\sim 10^{16}$ electrons/s (purple case in Figures 3.12 and 3.13). It is therefore expected that in reality, TGF sources do not necessarily reach the electron saturation regime.

It is critical to consider electron attachment processes in air at an altitude of 12 km. Under an electric field of magnitude $16 \times \frac{N}{N_0}$ kV/cm, electron attachment is dominated by the dissociative attachment process (2-body attachment of frequency ν_{att2b}) with a characteristic timescale of $\frac{1}{\nu_{att}} \sim 0.5$ μs, even though more generally $\nu_{att} = \nu_{att2b} + \nu_{att3b}$, where ν_{att3b} is the 3-body attachment frequency. Assuming an injection rate of 10^{16} electrons/s, it becomes clear that the low-energy electron density reaches a steady state at all locations in the simulation domain as an equality is reached between the ionization rate (produced by runaway electrons) and the attachment rate, this equality being reached over a duration on the order of $\frac{1}{\nu_{att}} \sim 0.5$ μs. Indeed, the dynamics of the low-energy electron density n_e is governed by the following equation at any given location:

$$\frac{dn_e}{dt} = \frac{F}{\lambda_i} - n_e \nu_{att} \tag{3.7}$$

where F is the local z-dependent flux of high-energy runaway electrons and $\lambda_i \sim 2$ mm is the total ionization mean free path for these electrons estimated from the ionization cross-section [e.g., Kim et al., 2000; Celestin and Pasko,

2010; Dwyer and Babich, 2011]. At the end of the acceleration region ($z = 400$ m), in the case with an injection rate of 2.94×10^{16} s^{-1}, the steady state is reached for $n_e = \dfrac{F_{z=400m}}{\lambda_i \nu_{att}} \sim 10^{13}$ m^{-3} (in good agreement with the results presented in Figure 3.12). Even though the electron density does not vary any longer, the flux of runaway electrons is still present after this time and so does the associated production of positive ions through ionization and negative ions through attachment. As a result of the flux of runaway electrons, the ion density increases linearly in time because ion recombination processes occur over a much longer timescale [see discussion in Berge et al., 2022, Section 2.1].

Gourbin and Celestin [2024b] showed that the electron saturation density caused by self-consistent effects occurs when the density is high enough so that the associated relaxation time is equaling the RREA characteristic growth time:

$$n_e^{sat} = \frac{\varepsilon_0}{q_e \mu_e \nu_{RREA}} \simeq 10^{15} \text{ m}^{-3} \quad ; \quad \nu_{RREA}^{-1} = 5.16 \times 10^{-7} \text{ s} \tag{3.8}$$

where q_e is the electron charge, μ_e is the electron mobility, and ν_{RREA} is the runaway electron production frequency. Figure 3.12 clearly shows that the quenching of the electric field is indeed rapidly observed for $n_e > 10^{14}$ m^{-3}. In fact, the saturation density n_e^{sat} may be thought of as an electron density upper limit. In general, the electric field is quenched over the dielectric relaxation time (also named Maxwell time) driven by the local conductivity, which is

mostly the result of the electron density and mobility (i.e., for $n_{\pm} < \frac{\mu_e}{\mu_{\pm}} n_e$, where $n_{\pm}$ is the density of positive and negative ions and $\frac{\mu_e}{\mu_{\pm}} \sim 100$) :

$$\tau = \frac{\varepsilon_0}{q_e \mu_e n_e} \tag{3.9}$$

Assuming that TGFs self-quench themselves, one can also use this timescale as a TGF characteristic rise time to estimate the corresponding maximum electron density, that is $\tau \sim 15$ μs. Equation (3.9) shows that in that case, $n_e \sim 10^{13}$ m^{-3}, which is also consistent with the case of an injection rate of 10^{16} electron/s (see Figure 3.12).

The number of high-energy electrons can be written as:

$$N_e = F_{z=400m} \cdot S \cdot \tau \tag{3.10}$$

where S is the area of the RREA at the end of the acceleration region.

As previously discussed, owing to the steady state of the electron density $F = n_e \nu_{att} \lambda_i$. Substituting F and τ (equation (3.9)) in equation (3.10), one obtains an expression for the total number of high-energy electrons in a TGF that does not depend on the low-energy density or the injection rate:

$$N_e = \frac{\varepsilon_0 \lambda_i \nu_{att}}{q_e \mu_e} \cdot S \tag{3.11}$$

For a broad range of electric fields, this expression yields $N_e \sim 10^{17}$. It is valid in subcritical conditions (electron density lower than saturation density)

and simply comes from the assumption that the TGF quenches itself over a duration equal to the dielectric relaxation timescale caused by the production of secondary electrons. It is presumably the reason why previous works using self-consistent calculations have obtained a consistent number of TGF photons despite significant differences in the configurations, parameters, and methods employed [e.g., Dwyer, 2012; Liu and Dwyer, 2013; Gourbin and Celestin, 2024b].

The role of the conductivity increase and corresponding dielectric relaxation of the field in TGF dynamics was already explicitly mentioned and demonstrated in previous works [e.g., Dwyer, 2012]. However, to our knowledge, it is the first time that such an analysis leading to a compact equation (3.11), resulting in a consistent number of high-energy electrons at the TGF source is conducted. Dwyer [2007] derived a formula for the fluence, that yields relatively close results, although it was in the context of relativistic feedback (Equation (39)).

We cannot exclude that the shortest observed TGFs ($\tau \lesssim 10$ μs) reach the electron saturation regime. In such supercritical conditions, the expected number of high-energy electrons is also appreciably constant at $\sim 10^{17}$ (e.g., see Figure 3.13). In the present work, this would correspond to the cases with initial injection rates $> 2.94 \cdot 10^{18}$ electrons/s. This naturally indicates that

TGFs cannot be shorter than ~ 1 μs as determined from the RREA timescale.

The existence of a maximum electron density $n_e^{sat} \sim 10^{15}$ m^{-3} reachable in a TGF and a corresponding minimum TGF timescale of ~ 1 μs (RREA rate for a field of $16 \times \frac{N}{N_0}$ kV/cm at 12 km) are also demonstrated for the first time by the present work.

Even with more realistic TGFs consistent with maximum electron densities of $n_e \sim 10^{13}$ m^{-3}, we can infer a strong impact of the preionization on subsequent leaders and streamers propagation dynamics and hence the related radio observations. Because the cross-section of the RREA at the end of the avalanche is controlled by the diffusion of runaway electrons, the above analysis points to the compactness of TGF sources with radii $\lesssim 200$ m.

3.4 Concluding remarks

Using self-consistent simulations, we managed to highlight several effects not reported before in other model studies:

- Due to the balance between ionization in the avalanche and dielectric relaxation, a saturation density exists and acts as an upper limit for the avalanche.

- This saturation density yields interesting consequences, as it also limits the umber of high-energy electrons present at each instant, effectively

limiting the brightness of the TGF, at magnitudes similar to the ones observed in the brightest TGFs.

- These limits also imply a lower limit on TGF timescale, as under such condition, he reaches the expected brightness in about 1 μs.

- By generalizing these limits, assuming that the TGF will always eventually self-quench, we derive a formula for the number of electrons, consistently resulting in a number of the order of 10^{17}, weakly dependent on the electric field.

- In the case of typical TGFs, we can infer a strong impact of the preionization on subsequent leader/streamer dynamics following the emission of TGFs.

Chapter 4

Relativistic Feedback Mechanism

Contents

In this chapter, we focus on one of the two main mechanisms proposed to produce runaway seed electrons triggering RREAs: the relativistic feedback mechanism. This mechanism relies on backward propagating particles that can eventually create new free runaway electrons around the area where the first avalanche started, thus starting new avalanches [Dwyer, 2003]. This mechanism allows for the production of a great number of electrons while starting with relatively few runaway electrons. It is especially relevant in cases where the background electric field is not much higher than the relativistic runaway threshold field.

Dwyer [2003] describes two types of feedback. One possible case of feedback is driven by photons: an electron can create a photon by bremsstrahlung

emission that would go backwards, either directly or after being redirected through Compton scattering, independently of the electric field. It then could create new electrons through Compton scattering, photoelectric emission, or positron-electron (e^+e^-) pair production. The other case of feedback is driven by positrons: created through e^+e^- pair production, it would be accelerated in the backward direction due to its positive charge, back to the start of the RREA region, where it would free an electron via hard elastic scattering [e.g., see Pasko et al., 2023].

We present in the next section a study of the feedback threshold, where we aim to find an estimation of the critical electric field for the mechanism. The second section focuses on the properties of the mechanism, its ability to sustain RREAs, and on the validity of the relativistic feedback model in different environments. As stated in Chapter 2, our model does not include the creation and propagation of positrons, and it is instead considered that it annihilates immediately into two 511 keV photons. While this technically prevents positron feedback to occur, given the relatively small lengths of the acceleration region covered in the present study, counts of the various photon interactions in our simulations have shown that e^+e^- pair production, if existing at all, was negligible compared to Compton scattering and photoelectric effect.

We precise that the results presented in this chapter are preliminary, and require further research.

4.1 Feedback threshold

In order to assess the feasibility of the relativistic feedback mechanism in RREA initiation, we perform a series of simulations to determine the critical field above which it occurs.

4.1.1 Methods

As a preliminary study, we ran simulations with our self-consistent model to quantify what value of the electric field would allow the feedback to occur, and sustain multiple RREAs over time. By looking at the number of electrons produced since start, we can determine if the mechanism is successful at amplifying RREAs. However, an issue regarding the simulation had to be addressed: as the RREA occurs and the number of electrons starts increasing exponentially, the particle remapping algorithm starts forming particle electrons with very significant weights. The problem comes from the fact that each created photon is a computer particle that has the same weight as the electron that created it. With the same logic, an electron created by a photon will have the same weight as the incident photon. Because of that, a single computer photon could start a RREA that represents orders of magnitude

more electrons than the first one. While this is not an issue in the previous chapter, as we were focusing on a single avalanche, where all particles are concentrated in one structure, the possibility of relativistic feedback depends on the behaviour of individual particles, and as such, the weight of the particle becomes highly relevant. While a great number of simulations would still provide a correct representation on average, the coarse graining caused by remapping removes the significance of one single run.

To avoid this problem, we instead decided to compare the number of electrons produced by the first avalanche (also named primary RREA in this chapter), with the number of secondary electrons, produced by secondary avalanches initiated by secondary electrons that were created by photon interactions in a second step. The second step of the photon transport is realized using a Monte Carlo model that is much more efficient than the null-collision technique (see Celestin and Pasko [2012] ; Østgaard et al. [2008]). We place the system at an altitude of 12 km, on a domain of size $z \times r = 400$ m $\times$ 500 m. The whole domain will be submitted to various electric fields in order to quantify the feedback threshold.

The method can be summarized as follows:

1. **Propagation of the primary RREA:** We launch a single electron (particle of weight 1) from the start of our domain (near the (0,0) point),

and let it propagate. As it does, it ionizes and creates new electrons, forming a RREA. It also creates photons via bremsstrahlung, and we record the position where the photons were created, as well as their velocity components, their energy and their weight. In this stage, photons are just produced with a energy, momentum, and location, but are not allowed to propagate. The run lasts until all primary electrons have left the domain ($z > 400$ m), and we count at the end the maximum number of electrons produced N_e^p.

2. **Propagation of the created photons:** We then enter the photons data we recorded as input into another code, that will take care photon transport, and process their interactions. The photons here can propagate either in the region $z < 400$ m, or as far as they can. As they do, they can interact through Compton scattering, photoelectric effect or e^+e^- pair production. This code does not take electron propagation into account, and instead records the relevant data of the created electrons: their positions, velocity components, energy, and weight. For each photon, the run lasts until it crossed the boundary domain, or until it reaches an energy < 1 keV.

3. **Propagation of the secondary electrons:** Lastly, we propagate the newly created electrons, which act as secondary source electrons, in the

same configuration as in the first step, until they all leave the domain, and we look at the maximum number of secondary electrons produced N_e^s.

A summary of the method is shown in Figure 4.1.

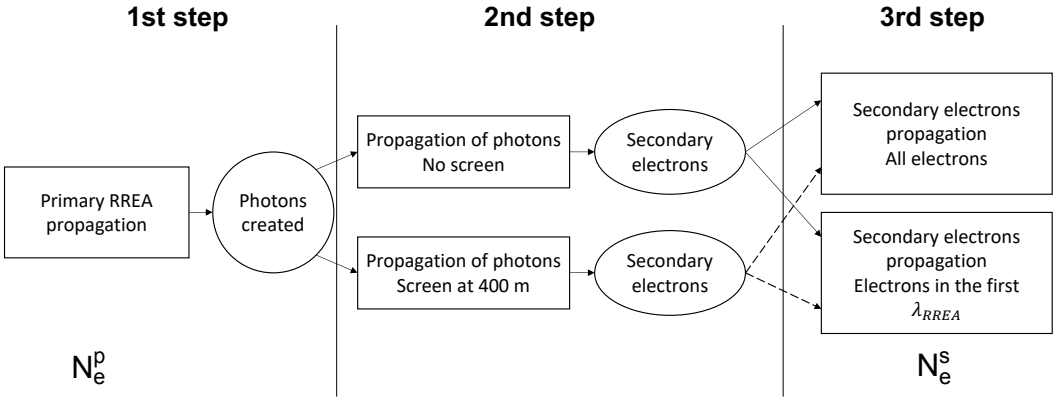

Figure 4.1: Summary of the method used for the evaluation of the feedback threshold. N_e^p and N_e^s are respectively the number of primary and secondary electrons produced. For each step, different configurations may be used. For each N_e^p, we thus obtain four different N_e^s.

By comparing N_e^s with the number obtained at the end of the first step N_e^p, we can determine if the relativistic feedback mechanism was successful or not, i.e., if the number of electrons produced in the third step N_e^s is higher that the number produced in the first step N_e^p, that means that the feedback managed to renew and increase the number of runaway electrons. On the contrary, if $N_e^s < N_e^p$, that means that the feedback is not enough to renew and amplify the RREA, and so that we are below the feedback threshold.

To assess how different configurations can influence our results, a second

photon propagation case is made for each primary avalanche, in which we add a screen at $z = 400$ m in the second-step calculation that blocks the photons reaching it. We now have at the end of step 2 two sets of secondary electrons for each primary avalanche.

Another point to address is the fact that secondary electrons are produced over the whole domain, and therefore not all of them are able to generate a significant amount of bremsstrahlung photons before leaving the simulation domain. We can in particular imagine a case where most secondary electrons are produced towards the end of the domain, near $z = 400$ m. In that case, they may very well start avalanching, all of them producing enough electrons to go beyond the number reached in the primary RREA, but a the same time producing relatively few photons, and of lower energy than in the first step. In that case, we would end up with a case where $N_{\mathrm{e}}^{\mathrm{s}} > N_{\mathrm{e}}^{\mathrm{p}}$, and thus, according to our criteria, that would validate the relativistic feedback mechanism, but in reality RREAs would not be sustained over repeated cycles. This would presumably be the case for a photo-electron production length lower than the RREA length.

To address this issue, we run another case in the third step, in which only the secondary electrons located in the first avalanche length (between z =0 m and z =λ_{RREA}) are propagated. Since the number of electrons we

work with here is relatively low, we do not expect a significant change in the electric field, and so we can assume that, if a secondary RREA starts near the starting location of the primary one, it should be able to provide roughly the same amount of photons and electrons as the primary RREA. This gives us a better confidence in our results, although by significantly reducing the number of secondary source electrons used. All configurations used are displayed in Figure **??**.

4.1.2 Results and discussion

We ran simulations over a range of electric field that is expected to be around the feedback threshold [Dwyer, 2003; Skeltved et al., 2014; Pasko et al., 2023].

The results are presented Figure 4.2. The number of secondary electrons produced can be compared to the number of primary electrons. For an electric field of $10 \times N/N_0$ kV/cm, secondary avalanches fail to reach a number of electrons equal to N_e^p. At $12 \times N/N_0$ kV/cm, the case with no screen where all electrons are taken into account manages to amplify the amount of electrons above the amount produced in the first step. However, the other cases are still below by several orders of magnitude. In particular, the case with no screen but taking into account only the secondary source electrons in the first avalanche length is below threshold. Presumably, one reason is that most avalanching electrons are produced near the edge of the domain, blurring the

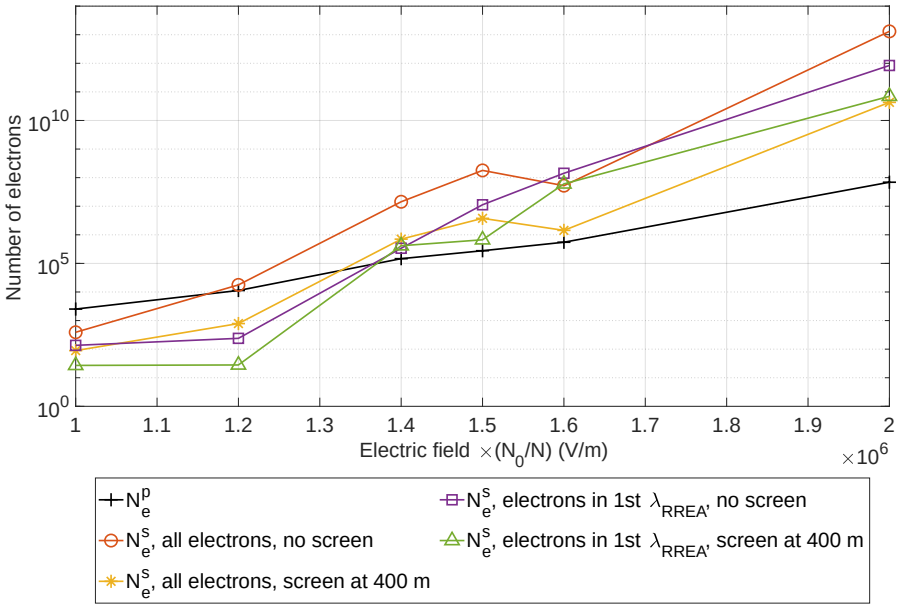

Figure 4.2: Results of the simulations ran following the methods summarized Figure 4.1. The black line represent the number of primary electrons N_e^p, produced during the first step. The other lines represent the number of secondary electrons N_e^s, produced during the third step, for different configurations.

field above which a full-fledged feedback is sustained. Another reason is the randomness of the approach.

In all other cases, for $E \geq 14 \times N/N_0$ kV/cm, all simulations of secondary RREAs produces a greater number of secondary electrons than there were primary electrons. Thus, it should be safe to assume that, in these cases, $14 \times N/N_0$ kV/cm exceeds the critical field.

Deriving a precise value of the critical field is difficult in this case, as the random aspect of the Monte Carlo technique not only plays a determining role on whether or not a new avalanche starts, but also on the position where

photons and photo-electrons are created and toward where they propagate. This explains the disparities between the different configurations used, and why no proper fit seems to be applicable to these cases.

While it prevents us to give a definitive value on the critical field, we can evaluate around where it stands. Looking at Figure 4.1, we can derive two values that can act as minimum and maximum threshold values. The minimum threshold is marked by the case "all electrons, no screen", for which N_e^s is higher than N_e^p at the lowest electric field among the four cases. It yields a critical field $E_{th}^{min} = 11.6$ kV/cm. On the other side, the case which is last to reach its critical field is the case "electrons in 1st λ_{RREA}, screen at 400 m". It makes sense, since it is the case which put the most constraints on the number of secondary electrons, by limiting the number of photons, and then cutting the number of photo-electrons produced. It yields a critical field $E_{th}^{max} = 13.7$ kV/cm.

These two cases are relevant, as they are respectively similar to the configurations used in Dwyer [2003]; Skeltved et al. [2014] for E_{th}^{min}, and Pasko et al. [2023] for E_{th}^{max}. [Dwyer, 2003, Figure 3] predicts a critical field of 9.5 kV/cm, which was also the value found by Skeltved et al. [2014] using another model. On the other hand, Pasko et al. [2023] deduces for this length a critical electric field of 15.6 kV/cm. It is clear, in their case, where each study used their own

respective model, and in our case, where we used one model with different configurations, that the configuration of the domain in which simulations are performed is critical to assess the feedback threshold.

4.2 Feedback properties

In order to study the importance of relativistic feedback over different timescales, and try to better understand its properties and constraints, we ran self-consistent simulations with our model, starting from one runaway electron, and artificially changing the probability of collision for photons P_{coll} (e.g., see details pertaining the null-collision method in Moss et al. [2006]). We ran three simulations: all of them have a domain of $z \times r$ =400 m $\times$ 500 m at an altitude of 12 km, start with initially one runaway electron at (0,0), with no injection afterwards, and has a background electric field over the whole domain of $20 \times N/N_0$ kV/cm. The first simulation (case 1) has the true P_{coll}. The second (case 2) has a probability of collision $P_{\text{coll}} \times 10$, and the third (case 3) has a probability of collision $P_{\text{coll}} \times 100$. The simulations are left to run long enough to assert whether the feedback mechanism is able to sustain the RREA, of until there is no particle left. The results of the simulations are shown Figure 4.3, 4.4 and 4.5, respectively for case 1, 2 and 3.

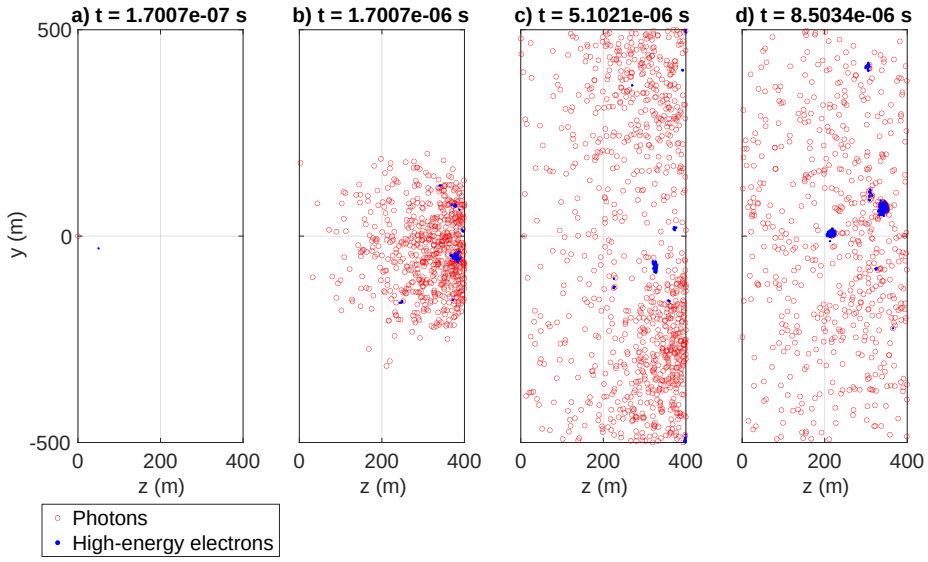

Figure 4.3: Evolution of the simulation in a case when P_{coll} remains unchanged. the red circles represent photons, while the blue dots represent energetic electrons.

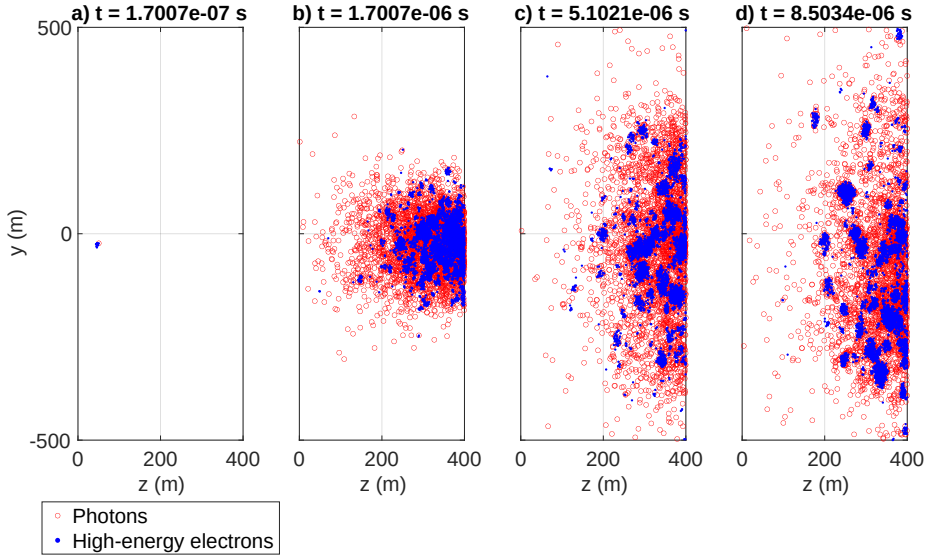

Figure 4.4: Evolution of the simulation in a case when P_{coll} is multiplied by 10. the red circles represent photons, while the blue dots represent energetic electrons.

In case 1, we see the relativistic feedback occurring as expected. Indeed, Dwyer [2003]; Skeltved et al. [2014]; Pasko et al. [2023] and our results in

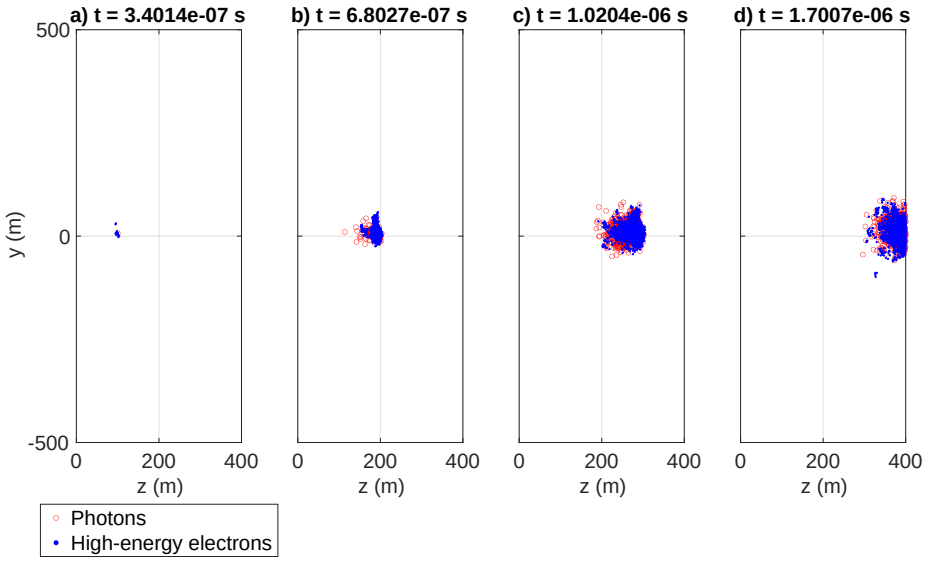

Figure 4.5: Evolution of the simulation in a case when P_{coll} is multiplied by 100. the red circles represent photons, while the blue dots represent energetic electrons.

the previous section all situated the critical electric field for feedback to be below that value. We see photons propagating backwards, and starting new avalanches at different locations of the domain. In case 2, the relativistic feedback mechanism is significantly amplified, as we could have expected. Indeed, by multiplying the probability of collision by 10, we increase the probability of photo-electron production, and so runaway electron production. We note that most photons and electrons remain located on the right half of the domain. In case 3, something peculiar happens: while the primary RREA does develop normally, emitted photons seem to remain trapped inside the main body of the avalanche, rarely escaping more than a few meters away before disappearing. Because of that, all the produced electrons remain confined inside the

primary avalanche, and the RREA was not self-sustained over time.

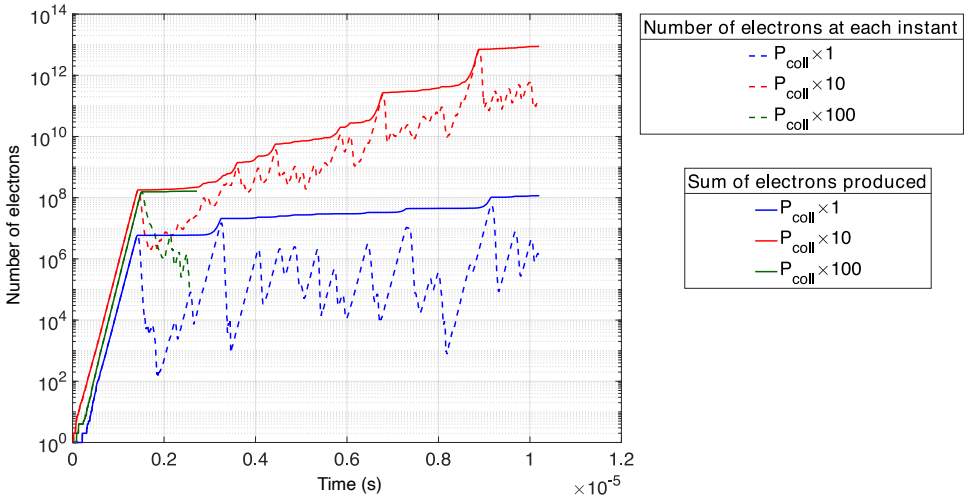

Figure 4.6: Number of high-energy electrons (> 1 MeV) in our domain as a function of time, and produced since start, for three different simulations, using different P_{coll}.

The number of energetic electrons for each case is shown Figure 4.6. Since electrons disappear and reappear continuously over time as a result of going out of the domain and being produced by photon collisions respectively, the number of electrons produced since start is a good indicator about the efficiency of relativistic feedback: if this number stagnates, it means the feedback has no effect. If it increases, it means it is successfully increasing the RREA intensity.

The trend while the primary RREA is still in the domain is the same for the three cases. It means that, while the first avalanche is still going on, it is electron interactions that leads to RREA intensification. Once this

avalanche gets out of the domain, the feedback process takes over. We notice that the increase happens in steps. This is mostly due to the discrete effect induced by remapping, as described in the previous section: a particularly "heavy-weight" photon is emitted backwards via bremsstrahlung, and start an avalanche with one "heavy-weight" electron, which creates particles of the same weight, making the produced RREA lead the increase of the number of electrons, like the primary one. Considering the time and the number of timesteps the simulations lasted, we assume that if we were to take each electron as an individual particle in our simulation, the overall increase from start to finish would be similar, but smoother.

The increase due to relativistic feedback is much slower than the increase due to the primary avalanche. For case 1 which uses the standard P_{coll}, relativistic feedback increases the number of electrons produced by one order of magnitude in 10 μs. Starting from 10^7 electrons, for an electric field of 20 ($\times N/N_0$) kV/cm, it would requires about 100 μs to reach 10^{17} energetic electrons. Considering how intense the electric field is in these simulations, and that we usually consider a TGF rise time of $\sim$ 15 μs, it questions whether the relativistic feedback mechanism would be sufficient to explain TGF observations [e.g., Mailyan et al., 2016]. It also seems that the number of primary electrons reached by the first avalanche will also plays an important part re-

garding the dynamics of the system. This highlights the importance of the length of the acceleration region: a longer acceleration region not only reduces the feedback threshold [Dwyer, 2003; Skeltved et al., 2014; Pasko et al., 2023], but also allows the primary RREA to reach a higher number of electrons before fading out.

For case 3, it appears that, by increasing the probability of collision by a hundred, we have decreased the photon mean free path length below the characteristic longitudinal extent of the RREA, making the relativistic feedback mechanism non-sustainable over time (for a finite acceleration region). This recalls the "problem case" mentioned in the previous section, where most photo-electrons produced would be near the edge of the acceleration domain, because this is exactly what happens here: the photon production is more intense when the RREA is more developed, so near the end of the acceleration region. Hence the majority of photons are in this region, and because of their modified probability of collision, they can't propagate beyond a distance $\sim \lambda_{RREA}$. Thus, even though they may be as much, or perhaps even more, photo-electrons produced, than primary electrons (case where $N_e^s \geq N_e^p$ in the previous section), they effectively are unable to start new RREAs.

While this result was obtained by manually changing a parameter otherwise constrained by the environment, it does not mean this situation is

completely unrealistic. While this may not be really relevant in air, it has an obvious theoretical importance and might be relevant to other gases. It also shows the limits of a multi-steps method as used in Dwyer [2003] or in the previous section. The relativistic feedback mechanism appears to be a complex spatio-temporal problem, and its temporal aspect especially cannot be ignored. Acknowledging this, self-consistency seems to be more relevant than ever if we wish to properly describe it.

4.3 Discussion

To increase our confidence in our feedback threshold estimations, and perhaps obtain a proper trend as a function of the electric field, we would need to perform at least several simulations for each case and electric field, but also evaluate the validity and trustworthiness of each case, especially regarding the cases using only source electrons inside the first avalanche length. For 10 and 12 kV/cm, it had reduced the number of electrons to several tens, and sometimes none had enough energy to restart a RREA. Considering the simulations at 12 kV/cm, where the main difference in the results is of three orders of magnitude, and that one of the cases does produce feedback, it is important to consider carefully the configuration used before drawing a conclusion.

Regarding the results presented in Section 4.2, they open the question of the feasibility of the relativistic feedback mechanism in various environments. Further research is required in order to reach more conclusive results. Previous works focused on positron feedback and deemed it significant, so it would be wise to include it in future self-consistent simulations, to assess its effect on RREA propagation and sustaining.

4.4 Conclusions

- We showed that it is important to account only for fully-fledged RREAs when quantifying the relativistic feedback threshold field. This point is instantiated by the fact that positive feedback can be non-self-sustaining (see case 3 in Section 4.2).

- The limited region of space for photon propagation can explain differences between thresholds obtained by Dwyer [2003] and Skeltved et al. [2014], with those obtained by Pasko et al. [2023], at least partially.

- We have also pointed out that relativistic feedback is unlikely to be the only seeding mechanism for RREAs when typical lengths and timescales believed to be present in TGFs are considered (at least in the linear regime).

Chapter 5

General Conclusions

5.1 Summary

In the course of this Ph.D. research, we first developed a new model for simulating relativistic runaway electron avalanches (RREAs). In order to address the need for simulations able to reproduce a wide variety of phenomena (such as RREAs, bremsstrahlung, radio emissions, etc.), we have chosen to develop a fully self-consistent model. Indeed, the electrostatic approximation may not be able to accurately represent the phenomena in which energetic electrons propagates with a speed nearing the speed of light, and so we instead use an electromagnetic model, hence guaranteeing a causal description of the system. The model makes use of multiple numerical techniques, such as:

- A Monte Carlo method, which models the collisional dynamics of photons and electrons. It constrains the timestep by the use of the null-collision method, and uses cross section data and analytical formulas to simulate the dynamics of each particle.

- An electromagnetic particle-in-cell (PIC) method, that allows the simulation of interactions between the electromagnetic field and charged par-

ticles. The particle-in-cell code uses the Maxwell-Ampere and Maxwell-Faraday equations to update the electromagnetic field at each timestep, contrary to most previous models, which use the electrostatic approximation and solve the Poisson equation.

- A fluid part, which is in charge of modelling the physics of ions and low-energy (< 1 keV) electrons, limiting the number of individual particles the model has to process.

- A remapping algorithm, which merges particles (photons and energetic electrons), limiting the number of particles the model has to compute, by attributing a statistical weight to computer particles.

The complete model allows for a time-resolved high-resolution simulation of the RREA process and associated phenomena. Validating the continuity equation at each instant is primordial for the PIC scheme to remain stable, so we use a specific current assignment scheme: the Villasenor scheme, and an specific field interpolation scheme: the cloud-in-cell (CIC) scheme. We tested the model for validation by simulating a perturbation in a warm homogeneous plasma, and confirmed that our model was working as intended.

Using our newly developed model, we design simple configurations to simulate RREAs in various environments, and from the results we draw several

conclusions:

- When reaching a certain density, the RREA self-quenches and the electrons density stops increasing. This observed saturation is due to the balance between the creation of new free electrons by ionization of air molecules, and coulombian forces repelling electrons from each other. This balance is translated into the equality between the avalanche characteristic time, τ_{RREA}, and the dielectric relaxation time, or Maxwell time, τ_M. This equality allows us to determine a formula for the electron saturation density: $n_e = \dfrac{\varepsilon_0}{q_e \mu_e \tau_{RREA}}$.

- We observe that the saturation of electron density leads to the stabilization of the number of high-energy (>1 MeV) electrons. By assuming that any TGF will eventually self-quench because of a high-electron density, we find that the RREA will yield a number of high-energy electrons following this formula: $N_e = \dfrac{\varepsilon_0 \lambda_i \nu_{att}}{q_e \mu_e} \cdot S$. For an assumed compact source, this formula gives a number of electrons $N_e \sim 10^{17}$ over a wide range of electric fields, which is consistent with observations of high-intensity TGFs.

- The self-quenching assumption for TGFs implies that the electron saturation density is an upper limit. Because of the timescale of the relax-

ation of the field (Maxwell time), inversely proportional to the electron density, this implies a lower limit on TGF duration, of $\sim$1 μs, according to the speed at which the saturation is reached.

- Taking the self-quenching of TGF into consideration, we can infer a strong impact on leader and streamer dynamics in lightning propagation.

It is worth noting that the model configurations leading to those results were emulating the conditions inside the streamer corona at the tip of a leader, with high electric fields over a short domain, and high amount of electrons injected.

In parallel, we intended to evaluate the feasibility of the relativistic feedback mechanism, and to characterize it. In order to compare our results with previous estimations, we devised a multi-step protocol, to estimate the feedback critical electric field, above which the feedback is able to amplify the RREA. Preliminary results show that differences in configurations will have a significant impact on the result. The case where photons are free to propagate as far as they can, and where all photo-electrons are taken into account yields a value of the feedback threshold of 11.6 kV/cm. On the other hand, the case where photons are blocked at $z = 400$ m, and where only photo-electrons within the first λ_{RREA} remain, yields a critical field of 13.7 kV/cm. It appears that a significant fraction of photo-electrons were produced closer to

the end of the acceleration region rather than the starting location of the first RREA. Not only that, but blocking the photons at 400 m prevents photons from going beyond and then turning back, which limits further the number of photo-electrons in the second case. However, secondary RREAs in the second case are all starting near the start of the acceleration region where the first RREA started, ensuring that they can fully develop and then sustain the feedback over multiple cycles. Although it requires more simulations to arrive at a more accurate value, it shows that the method should be able to reach a precise and accurate result. Running multiple simulations for each case should reduce the randomness of the results, and allow to reach more precise and accurate values.

Using our model, we perform self-consistent simulations in configurations allowing the feedback to happen, and we make the collision probability of photons vary, in order to demonstrate the need to take into account only full-fledged RREAs when studying the self-sustainability and thresholds of feedback processes. From the results, we observe that, using standard parameters, the relativistic feedback mechanism amplifies RREAs at a slow rate even at very high electric fields. It implies that feedback is unlikely to act alone in the brightest and shortest TGFs. By manually increasing the probability of collision of photons, we reach a point where their mean free path length is

decreased too much to allow photons to leave the avalanche, hence preventing the formation of new RREAs. This is a case where, although the feedback is positive according to the criteria we previously used, it is non-self-sustaining. With this case, we thus highlight the importance of taking into account all aspects (spatial and temporal) of the relativistic feedback when studying it.

5.2 Perspectives

The model developed in this thesis is highly flexible and allows for a wide variety of simulations. However, improvements are required to further expand the understanding of TGFs.

The boundary conditions used, although simple, are sufficient for the cases considered in this study (short timescales). However, when the need arises for longer, more accurate simulations, they will need to be replaced by open boundary conditions, such as perfectly matched layer (PML) [Lehe et al., 2022], to prevent instabilities due to electromagnetic waves bouncing on the borders of the domain.

To allow for faster simulations, parallelization will need to be implemented. While each method used in our model have been parallelized efficiently before, the complexity is in implementing an efficient parallelization for the combination of all of them altogether.

5.2. Perspectives

As mentioned in previous chapters, e^+e^- pair production is not completely modelled, and positrons are not taken into account as particles in the model yet. Following the conclusion of the previous chapter, it becomes important to implement this aspect, in order to assess the true importance of positron feedback in making RREAs.

When the model will have been sufficiently improved, further studies will be available to us: by doing longer simulations, with more refined meshes, reproducing the observed radio emissions (from the low-frequency (LF) range to the very high-frequency (VHF) range) will be within the model's reach. As concluded in Chapter 4, the study of the relativistic feedback mechanism can benefit from a more in-depth analysis, with more simulations and an assessment of how domain configurations influence the result. Non-linear regimes also need to be explored, to assess the effects it could have on RREA self-sustaining mechanisms.

This model, while still incomplete, presents a new way of simulating RREAs, and shows the necessity of self-consistent simulations in order to do so.

Chapter 6

Résumé en français - French summary

Contents

6.1 Introduction

Les flash de rayons gamma terrestres (ou TGF, pour Terrestrial Gamma-ray Flash) sont des émissions intenses et très brèves de rayons gamma émises pendant les orages. La première observation de ce phénomène est reportée dans Fishman et al. [1994], et depuis de nombreuses observations ont pu être réalisées. Le TGF tient sa source au coeur des nuages d'orages. Des observations ont permit de contraindre sa durée à un ordre de $\sim$ 100 μs [Fishman et al., 2011]. Il se traduit par l'émission de 10^{17} à 10^{19} photons gamma [Dwyer and Smith, 2005; Gjesteland et al., 2015; Mailyan et al., 2016, 2019; Lindanger et al., 2021], ceux-ci pouvant atteindre une énergie de $\sim$40 MeV [Briggs et al.,

2010]. L'altitude d'émission de ces photons gamma a été estimée entre 10 et 15 km [Dwyer and Smith, 2005]. La plupart des TGFs sont émis vers le haut, d'où les nombreuses observations satellites, cependant des TGFs émis vers le bas ont également été découverts [Dwyer et al., 2004; Abbasi et al., 2018; Belz et al., 2020].

En parallèle des observations de rayons gamma, des émissions optiques [e.g., Heumesser et al., 2021; Skeie et al., 2022] et radio sur une grande gamme de fréquences ont également été observées et associées aux TGFs. Parmi eux, les pulses énergétiques intranuages (Energetic In-cloud Pulses (EIPs), [e.g., Lyu et al., 2016; Tilles et al., 2020]), les pulses lents basse fréquence (slow LF pulses, [e.g., Lyu et al., 2016; Tilles et al., 2020]), et les émissions à très hautes fréquences (VHF emissions, [e.g., Lyu et al., 2018]).

Comprendre les TGFs est essentiel, non seulement à une meilleure compréhension des événements orageux et des processus physiques ayant lieux durant ceux-ci, mais également afin d'estimer le potentiel danger que ces rayonnements énergétiques peuvent présenter, notamment pour les vols commerciaux et leurs passagers. On a estimé leur nombre à 400 000 par an [Briggs et al., 2013], mais ce nombre a récemment été mis en doute par la campagne ALOFT [Østgaard et al., 2023], dont les résultats préliminaires ont reportés l'observation de nombreux TGFs n'ayant pas pu être observés par d'autres

instruments, ce qui met en doute ce nombre. Des études de dosimétries ont été menées afin d'estimer le risque auquel les équipages de vols commerciaux s'exposent [e.g., Pallu, 2022], néanmoins les incertitudes sur la fréquence des TGFs présentent un obstacle majeur.

Il fait consensus que les TGFs sont créés à partir d'avalanches d'électrons runaway relativistes (ou RREA, pour Relativistic Runaway Electron Avalanche). L'idée est qu'un électron suffisamment énergétique plongé dans un champ électrique peut gagner plus d'énergie par ce champ qu'il n'en perd par collision avec les molécules de l'air: il devient "runaway". Cela lui permet d'atteindre des énergies de plusieurs MeV, et ainsi ioniser le milieu, libérant des électrons dont certains deviennent à leur tour runaway, ce qui finit par créer la RREA. En même temps, il créé des photons gamma par rayonnement de freinage, aussi appelé bremsstrahlung. Néanmoins la manière dont est créée cette avalanche fait débat. En effet, afin de produire une RREA suffisamment intense pour correspondre aux observations de TGFs, il faudrait une RREA avec un grand nombre d'électrons sources, soumis à un champ très élevé sur des distances de plusieurs kilomètres. Deux théories pourraient expliquer la production de RREAs assez intenses:

- Le mécanisme de feedback relativiste (relativistic feedback mechanism), qui repose sur l'émission de photons et positrons en direction de la zone

de départ de la première RREA, ce qui leur permet d'initier de nouvelles avalanches, multipliant la quantité d'électrons runaway produits, jusqu'à en obtenir suffisamment.

- Le mécanisme de runaway thermique (thermal runaway, ou leader based), qui repose sur la création de RREAs lors de la propagation d'éclairs: au bout d'une structure conductrice de gas ionisé appelée leader, des filaments de plasmas appelés streamers apparaissent, formant une zone où le champ électrique est très intense. Dans cette zone, une grande quantité d'électrons peut être injectée à partir du leader, ce qui pourrait initier une RREA suffisamment intense pour créer un TGF.

Pour le moment, nous manquons d'informations pour réussir à valider ou invalider l'une ou l'autre des théories. Le mécanisme thermal runaway n'estpas incompatible avec le feedback relativiste, mais il est habituellement considéré pour des zones d'accélération plus courtes [Pasko et al., 2023].

De nombreux modèles numériques ont été réalisés afin de mieux comprendre la RREA, ainsi que les émissions associées. Plusieurs sont parvenus à modéliser de manière précise la RREA [e.g., see Dwyer, 2021; Berge et al., 2022], et beaucoup de propriétés sont maintenant connues. Néanmoins, la plupart des émissions radio associées n'ont pas encore pu être reproduites, et beaucoup de questions demeurent.

Afin de mieux comprendre le mécanisme des RREAs, nous avons créé un nouveau modèle auto-consistent, s'appuyant sur une méthode de particle-in-cell (PIC) électromagnétique afin de simuler pleinement les interactions entre les particules chargées et le champ électromagnétique. Le détail de la méthode est présenté dans la section 6.2. Les premiers résultats et l'étude des caractéristiques des RREAs sont présentés dans la section 6.3. L'étude du mécanisme de feedback relativiste est présenté dans la section 6.4.

6.2 Méthodes

Le modèle utilisé regroupe de multiples méthodes numériques afin d'être le plus exhaustif possible.

Une méthode Monte Carlo est utilisée pour simuler les collisions des photons et des électrons pendant la simulation. Cette partie du modèle est basée sur le modèle Monte Carlo développé par Celestin and Pasko [2011]. Le modèle comprend 3 dimensions de l'espace des configurations, 3 dimensions de l'espace des vitesses, est relativiste, et simule la dynamique des électrons et photons sur des énergies allant de la fraction d'eV à la centaine de MeV. Cela étant dit, nous nous limitons à suivre la propagation d'électrons de haute énergie (>1 keV), les autres étant traités dans un modèle fluide. On considère l'air comme une mixture composée à 80% de diazote et 20% de dioxygène.

Une grande variété de collisions est prise en compte dans le modèle:

- Les excitations rotationnelles, vibrationnelles, électroniques, ainsi que les processus dissociatifs pour l'O_2 sont calculées à partir de tables de sections efficaces.

- L'ionisation, modélisée via le modèle de Bethe relativiste (relativistic binary-encounter-Bethe (RBEB)).

- L'attachement à deux et trois corps, bien qu'il ne devrait pas être significatif pour les énergies considérées (> 1 keV).

- Les collisions élastiques. On se place dans un cas à haute-énergie (>500 eV), et le collisions avec les molécules sont considérées comme similaires avec les collisions élastiques avec atomes. On considère que $\sigma_{\mathrm{e}}^{\mathrm{m}}(\varepsilon) \simeq 2\sigma_{\mathrm{e}}^{\mathrm{a}}(\varepsilon)$.

- Le bremsstrahlung est modélisé en extrapolant les sections efficaces de Seltzer and Berger [1986] sur l'ensemble des énergies considérées.

- L'effet Compton est décrit en utilisant la formule de Klein-Nishina et la conservation de la quantité de mouvement [Lehtinen, 2000; Pilkington and Anger, 1971; Heitler, 1960].

- L'effet photoélectrique est considéré comme transférant l'intégralité de

l'énergie du photon à l'électron, et l'angle d'émission est calculé en utilisant la formule 2.15.

- La production de paires positron-électron (e^+e^-) est simplifiée en considérant que le positron émis est immédiatement annihilé en deux photons de 511 keV. Pour la plupart des cas considérés dans cette étude, la production de paires est négligeable comparée aux deux autres interactions du photon, aussi cette approximation ne devrait pas avoir beaucoup d'effet.

Le code particle-in-cell est décrit clairement et en détail dans Lehe [2014]. L'objectif est de calculer aussi précisément que possible les interactions coulombiennes entre particules chargées. Le champ électromagnétique est modélisé sur une grille, la charge et le courant dû aux particules chargées sont assignés sur cette grille en utilisant des schémas d'assignation spécifiques. Une fois le champ électromagnétique mis à jour, il est interpolé à la position des particules chargées en utilisant des schémas d'interpolation similaires aux schémas d'assignation. Pendant la durée d'un pas de temps, le code PIC va effectuer 4 tâches:

1. Interpolation du champs électromagnétique sur les particules, en utilisant le schéma "nuages dans cellules" (Cloud in cell (CIC)).

2. Mouvement des particules chargées, en utilisant les équations de Newton relativistes, ainsi que l'algorithme de Boris.

3. Assignation de la charge et du courant des particules chargées à la grille, en utilisant pour la charge le schéma CIC, et pour le courant le schéma de Villasenor. L'emploi d'un schéma spécifique pour le courant est nécessaire afin de garantir la conservation de la charge.

4. Mise à jour du champ électromagnétique sur la grille, en utilisant une version discrète des équations de Maxwell-Ampère et Maxwell-Faraday. Un schéma "finite-difference time-domain" (FDTD) est utilisé. Les différents composants du champ électromagnétique sont calculés à différentes positions sur une maille de Yee. Le champ magnétique est également décalé dans le temps par rapport au champ électrique. Au moment d'interpoler, nous prenons donc la moyenne sur deux pas de temps du champ magnétique pour avoir une valeur sur l'instant considéré.

On valide le modèle en simulant un plasma et en vérifiant que l'on retrouve bien la relation de dispersion attendue pour une simulation PIC (cf Figure 2.5).

Une partie fluide prend en charge les ions ainsi que les électrons de basse-énergie (<1 keV). Leur mouvement est régit par des équations de "drift-

diffusion"

Afin de pouvoir suivre les électrons alors qu'ils croissent de manière exponentielle, une technique d'échantillonage appelée remappage (ou "remapping") est utilisée. Chaque particule suivie correspond à un certain nombre d'électrons, qui est le "poids" statistique W de la particule. Lorsque le nombre de particules dépasse un certain nombre, les particules sont triées, par positions et énergies voisines, puis fusionnées entre elles avec leur plus proche voisin. Les données de la particule résultante sont choisies au hasard parmi les deux particules initiales, pondérées par leur poids, et le poids de la nouvelle particule est l'addition du poids des particules initiales.

Les limites du domaine sont conductrices. Des instabilités peuvent apparaître dû au fait que les ondes électromagnétiques vont être réfléchies par les bords. Cependant, les simulations étudiées dans cette thèse sont suffisamment courtes, et le domaine de simulation est suffisamment étendu, pour que l'on puisse ignorer les effets dû aux réflexions du champ électromagnétique. Dans certains cas tests, des limites périodiques sont implémentées afin d'éviter la perte d'électrons.

6.3 Contraindre les paramètres de la RREA

Avec notre modèle, nous avons réalisé plusieurs simulations afin de mieux cerner le processus de RREA. Les premières simulations sont effectuées sur un domaine $z \times r = 4200$ m $\times 1200$ m. L'altitude choisie est de 12 km, et l'ensemble du domaine est soumis à un champ de $5 \times N/N_0$ kV/cm, où N_0 est la densité de l'air au niveau du sol, et N la densité de l'air à l'altitude considérée. Les électrons sont injectés soit continuellement tout le long de la simulation, soit tous injectés initialement au début de la simulation. Nous avons laissés tourner les simulations suffisamment longtemps pour laisser le temps à l'avalanche de traverser tout le domaine. A l'issue de ces simulations, nous avons observés plusieurs phénomènes intéressants:

- La densité d'électrons de basse énergie (< 1 keV) semble saturer autour de 10^{15} m^{-3}.
- Lorsque la saturation est atteinte, le champ est complètement écranté.
- Le nombre d'électrons de haute énergie (> 1 MeV) semble se stabiliser autour de 10^{17} lorsque la saturation de densité est atteinte.
- Le courant produit par l'avalanche atteint 10^6, et le champ magnétique associé mesuré à 150 km atteint des valeurs de l'ordre de ~ 1 μT.

Le courant et le champ magnétique sont bien au-delà des valeurs mesurées,

ce qui est dû au fait que les cas étudiés ici sont peu réalistes: le champ électrique appliqué à tout le domaine est intense, homogène, et infini.

L'écrantage du champ électrique semble indiquer que la saturation de densité a à voir avec les interactions électromagnétiques. Cette saturation peut être expliquée en considérant l'équilibre entre les forces coulombiennes qui repoussent les électrons entre eux, et le phénomène d'ionisation qui crée continuellement de nouveaux électrons libres. Ils sont respectivement caractérisés par le temps de relaxation diélectrique, ou temps de Maxwell $\tau_M = \dfrac{\varepsilon_0}{q_e \mu_e n_e}$, où ε_0 est la permittivité du vide, q_e la charge de l'électron, μ_e la mobilité de l'électron et n_e la densité d'électrons, et le temps caractéristique de l'avalanche $\tau_{RREA} = \dfrac{\lambda}{V_{e^-}}$, où λ est la longueur caractéristique de l'avalanche et V_{e^-} la vitesse des électrons. En considérant l'égalité entre les deux, on peut en déduire une formule pour la densité: $n_e = \dfrac{\varepsilon_0}{q_e \mu_e \tau_{RREA}}$. Cette formule donne pour notre cas $n_e = 3.2806 \times 10^{14}$ m^{-3}, ce qui est de l'ordre de la valeur observée dans la simulation.

Afin d'expliquer la stabilisation du nombre d'électrons, nous effectuons d'autres simulations, dans un domaine $z \times r = 3000$ m $\times 1200$ m, où la zone entre $z = 0$ et $z = 400$ m est soumise à un champ de $16 \times N/N_0$ kV/cm, ce qui en fait une zone d'accélération pour les électrons injectés. Les électrons sont injectés continûment à un taux constant durant la simulation. Les dif-

férentes simulations sont effectuées en faisant varier ce taux d'un cas à l'autre. Nous confirmons que la stabilisation précédemment observée est bien due à la saturation. De plus, en supposant que l'avalanche finit toujours par faire s'effondrer le champ électrique, nous parvenons à déduire une formule pour le nombre d'électrons produit par la RREA: $N_e = \frac{\varepsilon_0 \lambda_i \nu_{att}}{q_e \mu_e} \cdot S$, où S est la section latérale de l'avalanche à la fin de la zone d'accélération, λ_i la longueur de libre parcours moyen associée à l'ionisation et ν_{att} la fréquence d'attachement. On obtient la valeur $N_e \sim 10^{17}$, très peu dépendante du champ électrique, et correspondant aux valeurs observées dans les TGFs les plus intenses.

6.4 Mécanisme de feedback relativiste

Les résultats présentés dans ce chapitre sont préliminaires.

Nous cherchons dans ce chapitre à mieux comprendre le mécanisme de feedback relativiste. Nous commençons par essayer de déduire le champ seuil (ou critique) au-delà duquel ce mécanisme est efficace à amplifier la RREA. Les simulations sont effectuées dans un domaine $z \times r = 400$ m $\times 500$ m, à une altitude de 12 km. Les champs électriques sont homogènes sur tout le domaine. Nous suivons le protocole suivant:

1. Une première avalanche est simulée, commençant initialement avec un électron à 1 MeV, sans propagation des photons, mais où on enregistre

leur coordonnées lorsqu'ils sont créés par bremsstrahlung ainsi que leur données physiques. Les simulations durent jusqu'à ce qu'ils n'y aient plus d'électrons dans le domaine. On enregistre à la fin combien d'électrons ont été créés.

2. Les photons sont ensuite propagés via un autre modèle, et on enregistre les données physiques des électrons créés ainsi que leur position de création.

3. Enfin, ces nouveaux électrons sont à leur tour propagés de la même manière qu'à la première étape, jusqu'à ce qu'il n'y ait plus d'électrons dans le domaine, et on enregistre à la fin combien d'électrons ont été créés.

Les simulations sont effectuées à différents champs électriques. Si le nombre d'électrons créés à la troisième étape est supérieur au nombre d'électrons créés à la première étape, c'est que le champ électrique est suffisant pour permettre au feedback relativiste de fonctionner. Nous effectuons les simulations dans différentes configurations, en rajoutant un écran qui absorbe les photons qui se propagent au-delà de 400 m, ou bien en ne lançant la troisième étape qu'avec les électrons présents dans la première longueur d'avalanche. Nous pouvons ainsi constater comment ces configurations influent sur le résul-

tat. Les différentes configurations donnent des résultats variés, allant d'une valeur du champ seuil de 11.6 kV/cm pour le cas sans écran et en prenant en compte tous les photo-électrons, à 13.7 kV/cm pour le cas avec écran en ne prenant en compte que les photo-électrons présents dans la première longueur d'avalanche. Ces configurations sont rappellent dans une certaine mesure Dwyer [2003] et Skeltved et al. [2014], qui trouvent une valeur de 9.5 kV/cm, et Pasko et al. [2023], qui parvient à une valeur 15.6 kV/cm, respectivement. Définir une tendance est compliqué, dû à l'aspect aléatoire du Monte Carlo. Néanmoins, la variabilité entre les différentes configurations montrent l'importance de celle-ci dans la détermination de ce champ seuil. D'autres simulations devront être effectuées afin d'obtenir des valeurs plus précises, et d'étudier plus en profondeur comment chaque configuration influe sur le résultat.

Nous avons ensuite effectué des simulations auto-cohérentes dans le même domaine, avec un champ de $20 \times N/N_0$ kV/cm, afin d'étudier les propriétés du feedback. Nous notons que l'accroissement du nombre d'électrons dû au mécanisme de feedback relativiste est bien plus faible que celui dû à l'avalanche elle-même. Quand bien même la taille de la région d'accélération pourrait influer sur ce résultat, il apparaît qu'il serait compliqué pour le feedback seul de former et d'amplifier les RREAs. De plus, nous notons que, si l'on augmente

suffisamment la probabilité de collision des photons, leur libre parcours moyen devient trop court pour permettre au photons de retourner dans la zone de départ de l'avalanche initiale, ce qui donc empêche le phénomène de feedback de se produire.

Même si ce résultat a été obtenu en modifiant manuellement un paramètre autrement contraint par l'environnement, il permet de constater une situation problématique, dans laquelle la plupart des photo-électrons sont produit vers la fin de la zone d'accélération, plutôt qu'au voisinage de la zone de départ de la première RREA. Dans ce cas, la méthode utilisé pour déterminer le champ seuil peut conclure à un feedback positif, alors que celui-ci ne serait pas auto-entretenu. Cela démontre la pertinence du cas dans lequel seul les photo-électrons présent dans la première longueur d'avalanche sont considérés. Plus généralement, ce cas met en avant le fait que le mécanisme de feedback relativiste est un phénomène complexe, dont tous les aspects spatiaux et temporels doivent être pris en compte.

Là également, une étude plus approfondie est nécessaire afin d'obtenir des résultats plus précis. Nous rappelons enfin que notre modèle ne modélise pas les positrons. D'autres études ayant conclu à l'importance du feedback par positrons, il serait judicieux de l'implémenter pour de futures études, afin d'étudier son réel impact.

6.5 Conclusions Générales

Le modèle utilisé est inédit par son auto-cohérence et par la large gamme de phénomènes physiques qu'il est ainsi capable de simuler.

Grâce à ce modèle, nous observons certains propriétés liés à la propagation d'une RREA, telle que la saturation de densité, qui peut s'expliquer par l'équilibre entre les forces coulombiennes et l'ionisation de l'avalanche. Nous parvenons également à expliquer la stabilisation du nombre d'électrons des TGFs intenses en supposant que la RREA finit toujours par effondrer le champ électrique, et retrouvons les valeurs observées pour ce nombre d'électrons.

Afin d'étudier le mécanisme de feedback relativiste, nous mettons au point une méthode afin de déterminer le champ critique au-delà duquel ce mécanisme est efficace à amplifier la RREA. La méthode permet d'arriver à de premiers résultats, avec des champs seuil minimum et maximum de 11.6 et 13.7 kV/cm respectivement. Les variations du champ seuil d'une configuration à l'autre mettent en lumière l'importance de la configuration utilisée. En effectuant des simulations auto-consistentes, nous notons que le mécanisme de feedback accroît lentement le nombre d'électrons comparé à la première RREA. De plus, nous mettons en évidence la complexité de ce phénomène, l'importance de prendre en compte tous ses aspects spatio-temporels, et les limites qu'une approche trop simple peut présenter pour le caractériser.

En travaillant sur les conditions limites du modèle et son optimisation, nous espérons pouvoir effectuer de plus longues simulations, et parvenir à reproduire les ondes radios observées en association avec les TGFs. Modéliser les positrons en tant que particules sera nécessaire afin d'étudier plus en profondeur le mécanisme de feedback relativiste. Une fois ces améliorations effectuées, une étude plus approfondie des stages non-linéaire des RREAs (saturation, écrantage), et les conséquences sur les mécanismes de maintien de la RREA, pourra être effectuée.

Appendices

Appendix A

Instantaneous initial injection

We display here the results for the case with an initial, instantaneous injection, mentioned in Chapter 3.

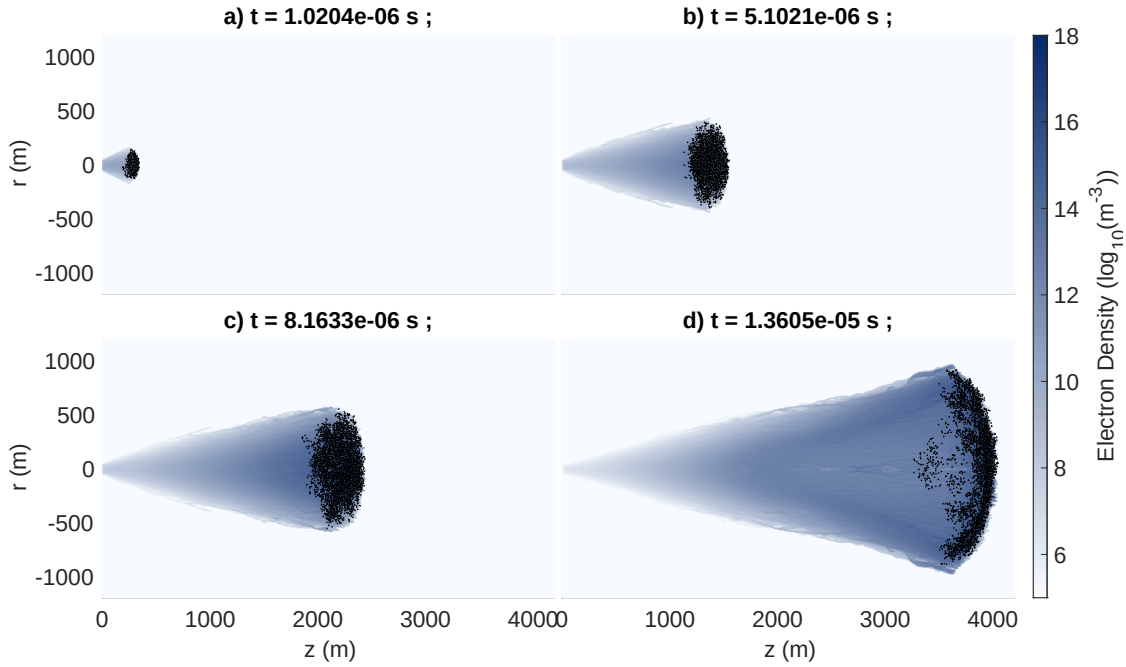

Figure A.1: Cross-sectional view of the low-energy electron density [$\log_{10}$(particle/m^3)] at different times. The high-energy electrons appear as black dots. The time passed since the beginning of the run is indicated at the top of each plot. The r-axis has been mirrored for clarity, as the model is axisymmetric. However, the high-energy electrons are shown in cartesian coordinates (x,z), to avoid doubling the number of points. One of the approximation our model entails is that each particle, which is a point, project its charge and current as a ring on our grid.

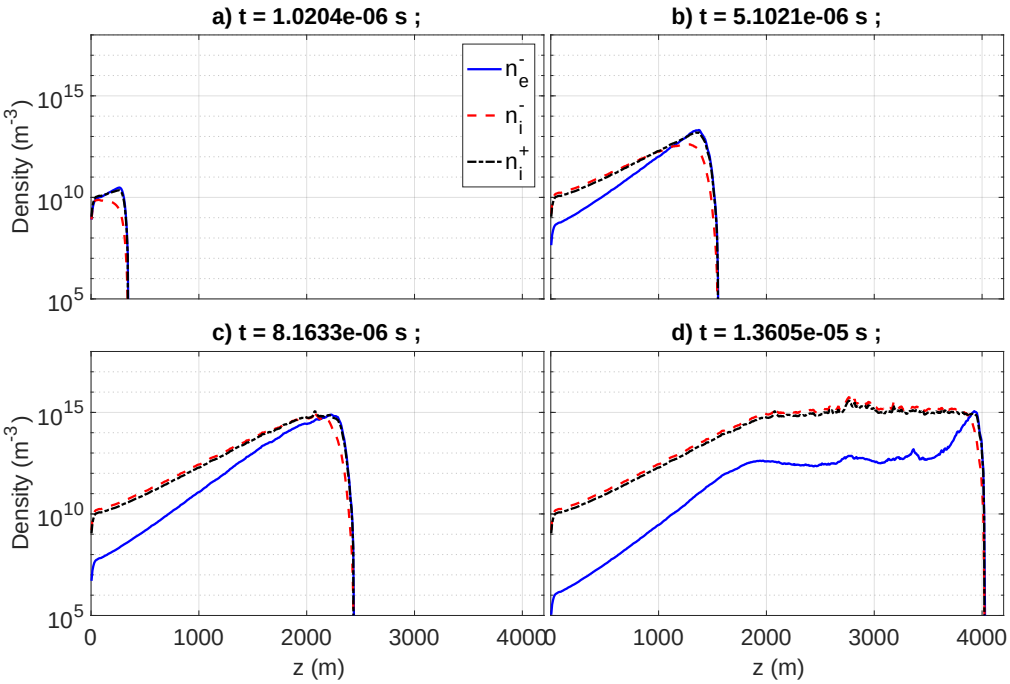

Figure A.2: Electron and ion densities along the z-axis at different times for initial injection (the densities shown in this figure are averaged in the r-dimension between $r = 0$ m and $r = 67.2$ m). The time passed since the beginning of the run is indicated above each plot. The blue, red, and black lines represent respectively the density of electrons, negative ions, and positive ions.

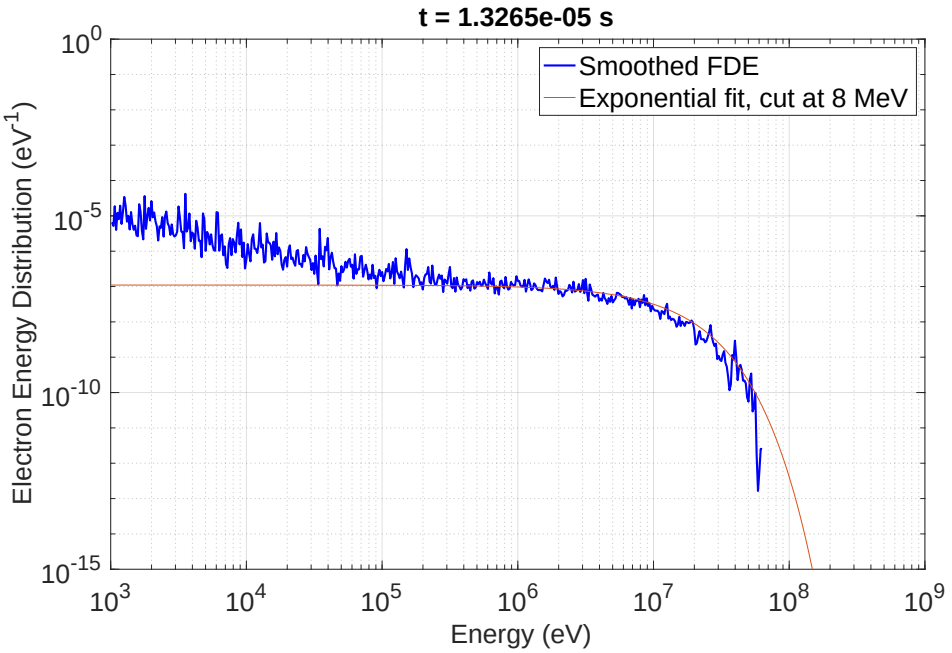

Figure A.3: Electron energy distribution for the case with initial injection.

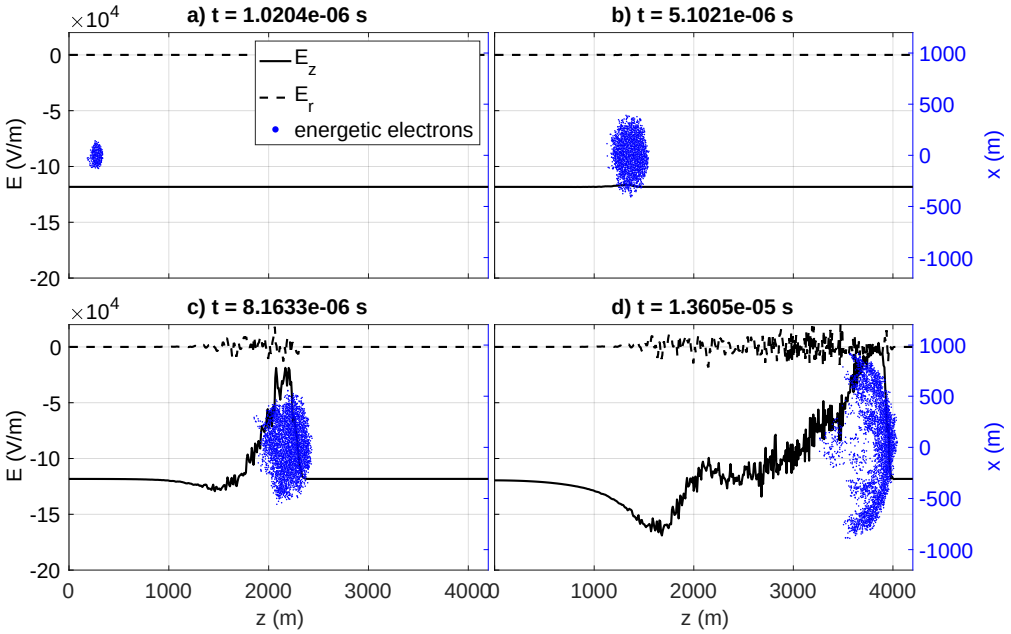

Figure A.4: Electric field near the axis $r = 0$ m (center of the avalanche) at different times for a simulation with initial injection. The r and z component of the electric field are shown as a function of z, as well as the (x, z) particle coordinates. E_z is shown on the axis, E_r is shown at $r = 8$ m.

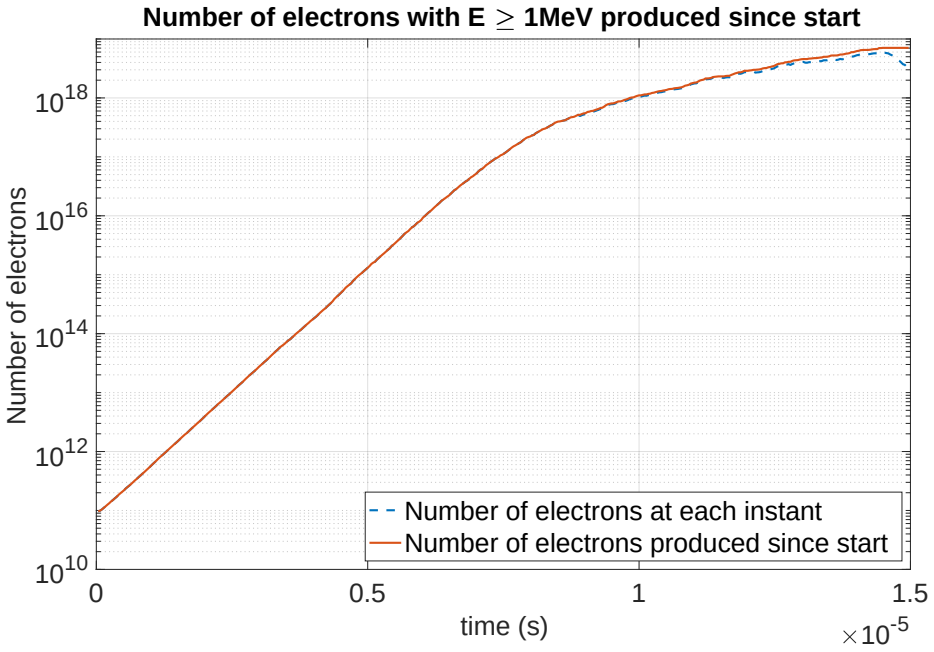

Figure A.5: Number of electron with an energy higher than 1 MeV as a function of time, for the simulation with initial injection.

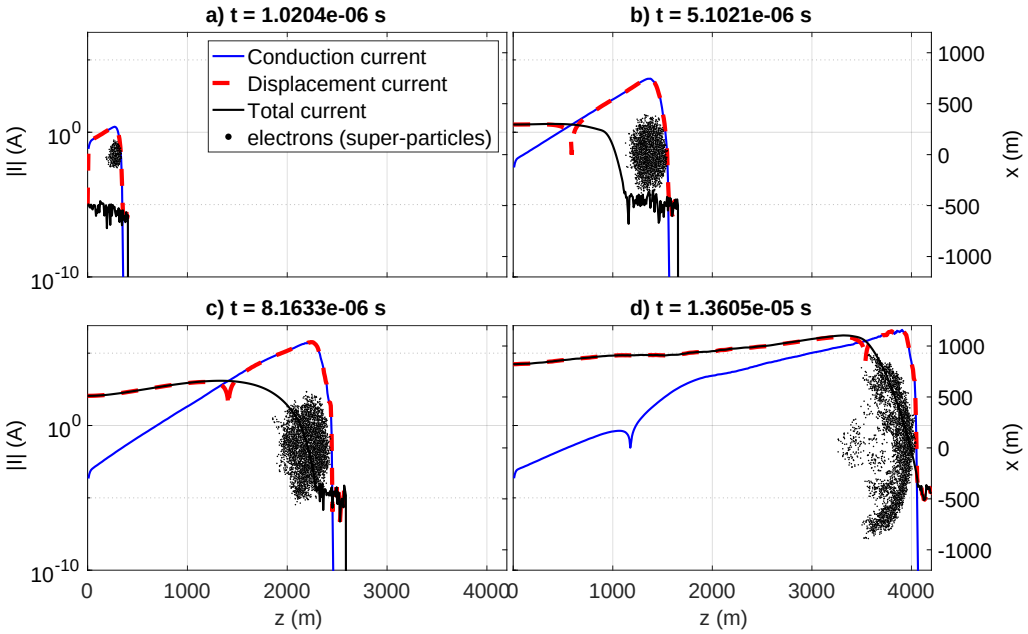

Figure A.6: Absolute value of the total electric current and its components (conduction and displacement) produced at different moments of time for the case with an initial injection.

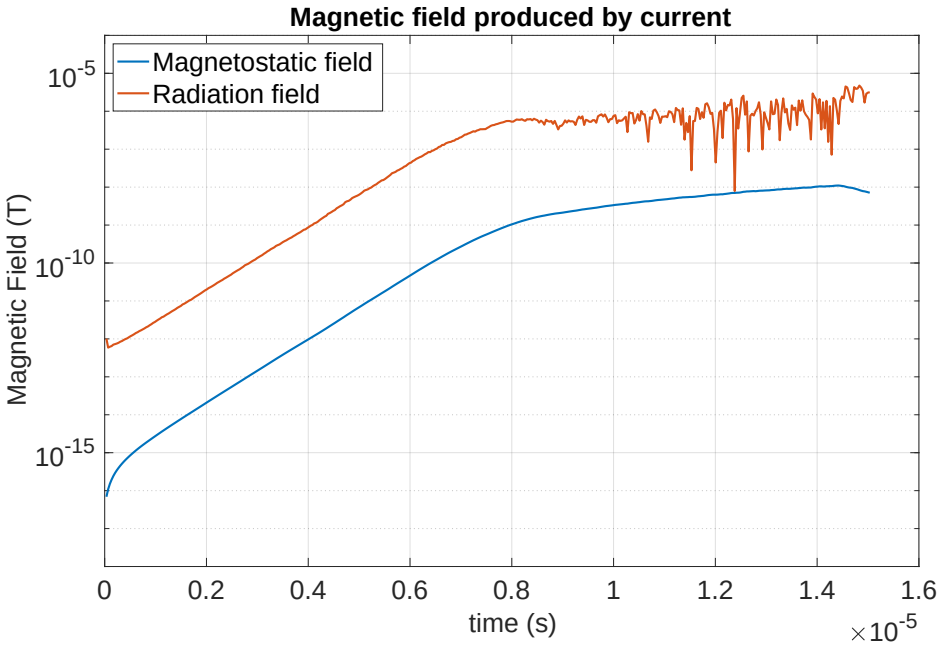

Figure A.7: Magnetic field computed from the current, using equation (7) from Uman et al. [1975]. The radiation and magnetostatic parts of the magnetic field shown here correspond to the two integrals in that equation. The computation is made for a distance from the source of 150 km, for the case with continuous injection.

Bibliography

Abbasi, R. U. et al. (2018). Gamma ray showers observed at ground level in coincidence with downward lightning leaders. *Journal of Geophysical Research: Atmospheres*, 123(13):6864–6879. (Cited on pages 2 and 106.)

Belz, J. W. et al. (2020). Observations of the origin of downward terrestrial gamma-ray flashes. *Journal of Geophysical Research: Atmospheres*, 125(23):e2019JD031940. (Cited on pages 2 and 106.)

Berge, N. and Celestin, S. (2019). Constraining downward terrestrial gamma ray flashes using ground-based particle detector arrays. *Geophysical Research Letters*, 46(14):8424–8430. (Cited on page 2.)

Berge, N., Celestin, S., Garnung, M. B., Xu, W., Marshall, R. A., and Cummer, S. A. (2022). Modeling low-frequency radio emissions from terrestrial gamma ray flash sources. *Journal of Geophysical Research: Atmospheres*, 127(5). (Cited on pages 4, 7, 41, 42, 56, 58, 72, 74 and 108.)

Berger, M., Hubbell, J., Seltzer, S., Chang, J., Coursey, J., Sukumar, R., Zucker, D., and Olsen, K. (2010). XCOM: Photon cross sections database. *National Institute of Standards and Technology*. (Cited on page 19.)

Berger, M. J., Coursey, J. S., Zucker, M. A., and Chang, J. (2005).

Stopping-Power and Range Tables for Electrons, Protons, and Helium Ions. NIST Standard Reference Database 124, http://www.nist.gov/pml/data/star/index.cfm. (Cited on page 23.)

Birdsall, C. and Langdon, A. (1991). *Plasma physics via computer simulations*. CRC Press. (Cited on pages 21, 25, 28 and 33.)

Bourdon, A., Bonaventura, Z., and Celestin, S. (2010). Influence of the pre-ionization background and simulation of the optical emission of a streamer discharge in preheated air at atmospheric pressure between two point electrodes. *Plasma Sources Science and Technology*, 19(3):034012. (Cited on page 65.)

Bourdon, A., Pasko, V. P., Liu, N. Y., Célestin, S., Ségur, P., and Marode, E. (2007). Efficient models for photoionization produced by non-thermal gas discharges in air based on radiative transfer and the helmholtz equations. *Plasma Sources Science and Technology*, 16(3):656–678. (Cited on page 41.)

Bowers, G. S., Smith, D. M., Kelley, N. A., Martinez-McKinney, G. F., Cummer, S. A., Dwyer, J. R., Heckman, S., Holzworth, R. H., Marks, F., Reasor, P., Gamache, J., Dunion, J., Richards, T., and Rassoul, H. K. (2018). A terrestrial gamma-ray flash inside the eyewall of hurricane patricia. *Jour-*

nal of Geophysical Research: Atmospheres, 123(10):4977–4987. (Cited on page 3.)

Briggs, M. S., Fishman, G. J., Connaughton, V., Bhat, P. N., Paciesas, W. S., Preece, R. D., Wilson-Hodge, C., Chaplin, V. L., Kippen, R. M., von Kienlin, A., Meegan, C. A., Bissaldi, E., Dwyer, J. R., Smith, D. M., Holzworth, R. H., Grove, J. E., and Chekhtman, A. (2010). First results on terrestrial gamma ray flashes from the Fermi Gamma-ray Burst Monitor. *Journal of Geophysical Research: Space Physics*, 115:A07323. (Cited on pages 2 and 105.)

Briggs, M. S., Xiong, S., Connaughton, V., Tierney, D., Fitzpatrick, G., Foley, S., Grove, J. E., Chekhtman, A., Gibby, M., Fishman, G. J., McBreen, S., Chaplin, V. L., Guiriec, S., Layden, E., Bhat, P. N., Hughes, M., Greiner, J., von Kienlin, A., Kippen, R. M., Meegan, C. A., Paciesas, W. S., Preece, R. D., Wilson-Hodge, C., Holzworth, R. H., and Hutchins, M. L. (2013). Terrestrial gamma-ray flashes in the fermi era: Improvedobservations and analysis methods. *Journal of Geophysical Research: Space Physics*, 118(6):3805–3830. (Cited on pages 4 and 106.)

Carron, N. J. (2006). *An Introduction to the Passage of Energetic Particles through Matter*. CRC Press. (Cited on pages 15 and 20.)

Celestin, S. and Pasko, V. P. (2010). Soft collisions in relativistic runaway electron avalanches. *Journal of Physics D: Applied Physics*, 43. (Cited on pages 8, 13 and 73.)

Celestin, S. and Pasko, V. P. (2011). Energy and fluxes of thermal runaway electrons produced by exponential growth of streamers during the stepping of lightning leaders and in transient luminous events. *Journal of Geophysical Research: Space Physics*, 116:A03315. (Cited on pages 7, 11 and 109.)

Celestin, S. and Pasko, V. P. (2012). Compton scattering effects on the duration of terrestrial gamma-ray flashes. *Geophysical Research Letters*, 39:L02802. (Cited on page 82.)

Celestin, S., Xu, W., and Pasko, V. P. (2012). Terrestrial gamma ray flashes with energies up to 100 mev produced by nonequilibrium acceleration of electrons in lightning. *Journal of Geophysical Research: Space Physics*, 117(A5). (Cited on page 5.)

Celestin, S., Xu, W., and Pasko, V. P. (2015). Variability in fluence and spectrum of high-energy photon bursts produced by lightning leaders. *Journal of Geophysical Research: Space Physics*, 120:10. (Cited on pages 7, 13, 53, 54, 67 and 72.)

Chanrion, O. and Neubert, T. (2008). A PIC-MCC code for simula-

tion of streamer propagation in air. *Journal of Computational Physics*, 227(15):7222–7245. (Cited on page 4.)

Coleman, L. M. and Dwyer, J. R. (2006). Propagation speed of runaway electron avalanches. *Geophysical Research Letters*, 33:L11810. (Cited on page 61.)

Cullen, D., Perkins, S., and Seltzer, S. (1991). Tables and graphs of electron interaction cross 10 eV to 100 GeV derived from the LLNL evaluated electron data library (EEDL), Z = 1–100. *Lawrence Livermore National Laboratory*, 31. (Cited on page 17.)

Dhali, S. K. and Williams, P. F. (1987). Two-dimensional studies of streamers in gases. *Journal of Applied Physics*, 62(12):4696–4707. (Cited on page 42.)

Dwyer, J. R. (2003). A fundamental limit on electric fields in air. *Geophysical Research Letters*, 30(20):2055. (Cited on pages 6, 10, 47, 48, 67, 79, 86, 88, 90, 94, 95, 96 and 118.)

Dwyer, J. R. (2007). Relativistic breakdown in planetary atmospheres. *Physics of Plasmas*, 14(4):042901. (Cited on pages 4, 6, 15 and 76.)

Dwyer, J. R. (2008). Source mechanisms of terrestrial gamma-ray flashes. *Journal of Geophysical Research: Atmospheres*, 113:D10103. (Cited on pages 5 and 6.)

Dwyer, J. R. (2010). Diffusion of relativistic runaway electrons and implications for lightning initiation. *Journal of Geophysical Research: Space Physics*, 115(A3). (Cited on page 14.)

Dwyer, J. R. (2012). The relativistic feedback discharge model of terrestrial gamma ray flashes. *Journal of Geophysical Research: Space Physics*, 117(A2). (Cited on page 76.)

Dwyer, J. R. (2021). Terrestrial gamma-ray flashes initiated by positive leaders. *Physical Reviews D*, 104:043012. (Cited on pages 4 and 108.)

Dwyer, J. R. and Babich, L. P. (2011). Low-energy electron production by relativistic runaway electron avalanches in air. *Journal of Geophysical Research: Space Physics*, 116(A9). (Cited on page 74.)

Dwyer, J. R. and Cummer, S. A. (2013). Radio emissions from terrestrial gamma-ray flashes. *Journal of Geophysical Research: Space Physics*, 118(6):3769–3790. (Cited on pages 6 and 42.)

Dwyer, J. R., Liu, N., and Rassoul, H. K. (2013). Properties of the thundercloud discharges responsible for terrestrial gamma-ray flashes. *Geophysical Research Letters*, 40(15):4067–4073. (Cited on page 3.)

Dwyer, J. R., Rassoul, H. K., Al-Dayeh, M., Caraway, L., Wright, B., Chrest, A., Uman, M. A., Rakov, V. A., Rambo, K. J., Jordan, D. M., Jerauld,

J., and Smyth, C. (2004). A ground level gamma-ray burst observed in association with rocket-triggered lightning. *Geophysical Research Letters*, 31:L05119. (Cited on pages 2 and 106.)

Dwyer, J. R. and Smith, D. M. (2005). A comparison between monte carlo simulations of runaway breakdown and terrestrial gamma-ray flash observations. *Geophysical Research Letters*, 32(22). (Cited on pages 1, 2, 5, 8, 65, 72, 105 and 106.)

Dwyer, J. R., Smith, D. M., and Cummer, S. A. (2012). High-Energy Atmospheric Physics: Terrestrial Gamma-Ray Flashes and Related Phenomena. *Space Science Reviews*, 173:133–196. (Cited on pages 5, 8, 48 and 61.)

Dwyer, J. R., Smith, D. M., Uman, M. A., Saleh, Z., Grefenstette, B., Hazelton, B., and Rassoul, H. K. (2010). Estimation of the fluence of high-energy electron bursts produced by thunderclouds and the resulting radiation doses received in aircraft. *Journal of Geophysical Research: Atmospheres*, 115(D9). (Cited on page 4.)

Fishman, G. J., Bhat, P. N., Mallozzi, R., Horack, J. M., Koshut, T., Kouveliotou, C., Pendleton, G. N., Meegan, C. A., Wilson, R. B., Paciesas, W. S., Goodman, S. J., and Christian, H. J. (1994). Discovery of Intense Gamma-

Ray Flashes of Atmospheric Origin. *Science*, 264:1313–1316. (Cited on pages 1 and 105.)

Fishman, G. J., Briggs, M. S., Connaughton, V., Bhat, P. N., Paciesas, W. S., von Kienlin, A., Wilson-Hodge, C., Kippen, R. M., Preece, R., Meegan, C. A., and Greiner, J. (2011). Temporal properties of the terrestrial gamma-ray flashes from the Gamma-Ray Burst Monitor on the Fermi Observatory. *Journal of Geophysical Research: Space Physics*, 116(A7). (Cited on pages 2, 72 and 105.)

Foley, S., Fitzpatrick, G., Briggs, M. S., Connaughton, V., Tierney, D., McBreen, S., Dwyer, J. R., Chaplin, V. L., Bhat, P. N., Byrne, D., Cramer, E., Fishman, G. J., Xiong, S., Greiner, J., Kippen, R. M., Meegan, C. A., Paciesas, W. S., Preece, R. D., Kienlin, A., and Wilson-Hodge, C. (2014). Pulse properties of terrestrial gamma-ray flashes detected by the Fermi Gamma-Ray Burst Monitor. *Journal of Geophysical Research (Space Physics)*, 119:5931–5942. (Cited on page 72.)

Gjesteland, T., Østgaard, N., Laviola, S., Miglietta, M. M., Arnone, E., Marisaldi, M., Fuschino, F., Collier, A. B., Fabró, F., and Montanya, J. (2015). Observation of intrinsically bright terrestrial gamma ray flashes from the mediterranean basin. *Journal of Geophysical Research: Atmo-*

spheres, 120(23):12,143–12,156. (Cited on pages 2, 65 and 105.)

Gourbin, P. and Celestin, S. (2024a). On the self-quenching of relativistic runaway electron avalanches producing terrestrial gamma ray flashes. *Geophysical Research Letters*, 51(10). (Cited on pages 46 and 66.)

Gourbin, P. and Celestin, S. (2024b). Self consistent modeling of relativistic runaway electron beams giving rise to terrestrial gamma-rays flashes. *Journal of Geophysical Research: Space Physics*, 129(5). (Cited on pages 11, 46, 74 and 76.)

Gurevich, A. V., Milikh, G. M., and Roussel-Dupre, R. (1992). Runaway electron mechanism of air breakdown and preconditioning during a thunderstorm. *Physics Letters A*, 165:463–468. (Cited on page 5.)

Heitler, W. (1960). *The Quantum Theory of Radiation*. International series of monographs on physics. Clarendon Press. (Cited on pages 19 and 110.)

Heumesser, M., Chanrion, O., Neubert, T., Christian, H. J., Dimitriadou, K., Gordillo-Vazquez, F. J., Luque, A., Pérez-Invernón, F. J., Blakeslee, R. J., Østgaard, N., Reglero, V., and Köhn, C. (2021). Spectral Observations of Optical Emissions Associated With Terrestrial Gamma Ray Flashes. *Geophysical Research Letters*, 48(4):e0700. (Cited on pages 3, 7 and 106.)

Hockney, R. W. and Eastwood, J. W. (1966). *Computer Simulation Using Particles*. (Cited on pages 21, 28, 31 and 35.)

Hwang, W., Kim, Y.-K., and Rudd, M. E. (1996). New model for electron-impact ionization cross sections of molecules. *The Journal of Chemical Physics*, 104(8):2956. (Cited on page 13.)

Itikawa, Y. (2006). Cross Sections for Electron Collisions with Nitrogen Molecules. *Journal of Physical and Chemical Reference Data*, 35:31. (Cited on page 17.)

Kambara, H. and Kuchitsu, K. (1972). Measurement of Differential Cross Sections of Low-Energy Electrons Elastically Scattered by Gas Molecules. I. Apparatus. *Japanese Journal of Applied Physics*, 11:609. (Cited on page 14.)

Kilian, P., Muñoz, P. A., Schreiner, C., and Spanier, F. (2017). Plasma Waves as a Benchmark Problem. *Journal of Plasma Physics*, 83(1):707830101. (Cited on pages 36 and 38.)

Kim, Y.-K., Santos, J. P., and Parente, F. (2000). Extension of the binary-encounter-dipole model to relativistic incident electrons. *Physical Reviews A*, 62:052710. (Cited on pages 13 and 73.)

Knoll, G. F. (2000). *Radiation detection and measurement*. John Wiley & Sons, Fourth edition. (Cited on page 40.)

Kossyi, I. A., Kostinsky, A. Y., Matveyev, A. A., and Silakov, V. P. (1992). Kinetic scheme of the non-equilibrium discharge in nitrogen-oxygen mixtures. *Plasma Sources Science and Technology*, 1(3):207–220. (Cited on pages 42 and 43.)

Lehe, R. (2014). *Improvement of laser-wakefield accelerators: towards a compact free electron laser*. PhD thesis, Ecole Polytechnique. (Cited on pages 21, 31 and 111.)

Lehe, R., Blelly, A., Giacomel, L., Jambunathan, R., and Vay, J.-L. (2022). Absorption of charged particles in perfectly matched layers by optimal damping of the deposited current. *Physical Reviews E*, 106:045306. (Cited on page 102.)

Lehtinen, N. G. (2000). *Relativistic runaway electrons above thunderstorms*. PhD thesis, Stanford University. (Cited on pages 19 and 110.)

Lehtinen, N. G., Bell, T. F., and Inan, U. S. (1999). Monte carlo simulation of runaway mev electron breakdown with application to red sprites and terrestrial gamma ray flashes. *Journal of Geophysical Research: Space Physics*, 104(A11):24699–24712. (Cited on page 4.)

Lindanger, A., Marisaldi, M., Maiorana, C., Sarria, D., Albrechtsen, K., Østgaard, N., Galli, M., Ursi, A., Labanti, C., Tavani, M., Pittori, C., and

Verrecchia, F. (2020). The 3rd agile terrestrial gamma ray flash catalog. part i: Association to lightning sferics. *Journal of Geophysical Research: Atmospheres*, 125(11):e2019JD031985. (Cited on page 72.)

Lindanger, A., Marisaldi, M., Sarria, D., Østgaard, N., Lehtinen, N., Skeie, C. A., Mezentzev, A., Kochkin, P., Ullaland, K., Yang, S., Genov, G., Carlson, B. E., Köhn, C., Navarro-Gonzalez, J., Connell, P., Reglero, V., and Neubert, T. (2021). Spectral analysis of individual terrestrial gamma-ray flashes detected by asim. *Journal of Geophysical Research: Atmospheres*, 126(23):e2021JD035347. (Cited on pages 2, 65 and 105.)

Liu, N. and Dwyer, J. R. (2013). Modeling terrestrial gamma ray flashes produced by relativistic feedback discharges. *Journal of Geophysical Research: Space Physics*, 118(5):2359–2376. (Cited on pages 4, 41, 65 and 76.)

Luque, A. (2014). Relativistic runaway ionization fronts. *Physical Review Letters*, 112:045003. (Cited on pages 4 and 64.)

Lyu, F., Cummer, S. A., Briggs, M., Marisaldi, M., Blakeslee, R. J., Bruning, E., Wilson, J. G., Rison, W., Krehbiel, P., Lu, G., Cramer, E., Fitzpatrick, G., Mailyan, B., McBreen, S., Roberts, O. J., and Stanbro, M. (2016). Ground detection of terrestrial gamma ray flashes from distant radio signals. *Geophysical Research Letters*, 43(16):8728–8734. (Cited on pages 3 and 106.)

Lyu, F., Cummer, S. A., Krehbiel, P. R., Rison, W., Briggs, M. S., Cramer, E., Roberts, O., and Stanbro, M. (2018). Very high frequency radio emissions associated with the production of terrestrial gamma-ray flashes. *Geophysical Research Letters*, 45(4):2097–2105. (Cited on pages 3 and 106.)

Mailyan, B. G., Briggs, M. S., Cramer, E. S., Fitzpatrick, G., Roberts, O. J., Stanbro, M., Connaughton, V., McBreen, S., Bhat, P. N., and Dwyer, J. R. (2016). The spectroscopy of individual terrestrial gamma-ray flashes: Constraining the source properties. *Journal of Geophysical Research: Space Physics*, 121(11):11,346–11,363. (Cited on pages 2, 65, 71, 93 and 105.)

Mailyan, B. G., Xu, W., Celestin, S., Briggs, M. S., Dwyer, J. R., Cramer, E. S., Roberts, O. J., and Stanbro, M. (2019). Analysis of individual terrestrial gamma-ray flashes with lightning leader models and fermi gamma-ray burst monitor data. *Journal of Geophysical Research: Space Physics*, 124(8):7170–7183. (Cited on pages 2, 65, 71 and 105.)

Marisaldi, M., Argan, A., Ursi, A., Gjesteland, T., Fuschino, F., Labanti, C., Galli, M., Tavani, M., Pittori, C., Verrecchia, F., D'Amico, F., Østgaard, N., Mereghetti, S., Campana, R., Cattaneo, P., Bulgarelli, A., Colafrancesco, S., Dietrich, S., Longo, F., Gianotti, F., Giommi, P., Rappoldi, A., Trifoglio, M., and Trois, A. (2015). Enhanced detection of terrestrial gamma-ray

flashes by agile. *Geophysical Research Letters*, 42(21):9481–9487. (Cited on page 2.)

Marisaldi, M., Fuschino, F., Labanti, C., Galli, M., Longo, F., Del Monte, E., Barbiellini, G., Tavani, M., Giuliani, A., Moretti, E., Vercellone, S., Costa, E., Cutini, S., Donnarumma, I., Evangelista, Y., Feroci, M., Lapshov, I., Lazzarotto, F., Lipari, P., Mereghetti, S., Pacciani, L., Rapisarda, M., Soffitta, P., Trifoglio, M., Argan, A., Boffelli, F., Bulgarelli, A., Caraveo, P., Cattaneo, P. W., Chen, A., Cocco, V., D'Ammando, F., De Paris, G., Di Cocco, G., Di Persio, G., Ferrari, A., Fiorini, M., Froysland, T., Gianotti, F., Morselli, A., Pellizzoni, A., Perotti, F., Picozza, P., Piano, G., Pilia, M., Prest, M., Pucella, G., Rappoldi, A., Rubini, A., Sabatini, S., Striani, E., Trois, A., Vallazza, E., Vittorini, V., Zambra, A., Zanello, D., Antonelli, L. A., Colafrancesco, S., Gasparrini, D., Giommi, P., Pittori, C., Preger, B., Santolamazza, P., Verrecchia, F., and Salotti, L. (2010). Detection of terrestrial gamma ray flashes up to 40 MeV by the AGILE satellite. *Journal of Geophysical Research: Space Physics*, 115:A00E13. (Cited on page 2.)

Moore, C. B., Eack, K. B., Aulich, G. D., and Rison, W. (2001). Energetic radiation associated with lightning stepped-leaders. *Geophysical Research Letters*, 28(11):2141–2144. (Cited on page 7.)

Morrow, R. and Lowke, J. J. (1997). Streamer propagation in air. *Journal of Physics D: Applied Physics*, 30(4):614–627. (Cited on pages 42, 43 and 61.)

Moss, G. D., Pasko, V. P., Liu, N., and Veronis, G. (2006). Monte carlo model for analysis of thermal runaway electrons in streamer tips in transient luminous events and streamer zones of lightning leaders. *Journal of Geophysical Research: Space Physics*, 111(A2). (Cited on pages 4, 5, 7, 12, 13, 14 and 89.)

Østgaard, N., Gjesteland, T., Stadsnes, J., Connell, P. H., and Carlson, B. (2008). Production altitude and time delays of the terrestrial gamma flashes: Revisiting the Burst and Transient Source Experiment spectra. *Journal of Geophysical Research: Space Physics*, 113:A02307. (Cited on page 82.)

Pallu, M. (2022). *Estimation of the radiation risk to aircrew and aircraft passengers associated with atmospheric electricity events such as terrestrial gamma ray flashes and gamma ray glows*. PhD thesis. Thèse de doctorat dirigée par Célestin, Sébastien Sciences de l'Univers Orléans 2022. (Cited on page 107.)

Pallu, M., Celestin, S., Trompier, F., and Klerlein, M. (2021). Estimation of radiation doses delivered by terrestrial gamma ray flashes within leader-

based production models. *Journal of Geophysical Research: Atmospheres*, 126(8):e2020JD033907. (Cited on page 4.)

Pallu, M., Celestin, S., Trompier, F., and Klerlein, M. (2023). Radiation risk assessment associated with terrestrial gamma ray flashes for commercial flights. *Journal of Geophysical Research: Atmospheres*, 128(6):e2022JD037569. (Cited on page 4.)

Palmroth, M., Ganse, U., Pfau-Kempf, Y., Battarbee, M., Turc, L., Brito, T., Grandin, M., Hoilijoki, S., Sandroos, A., and von Alfthan, S. (2018). Vlasov methods in space physics and astrophysics. *Living Reviews in Computational Astrophysics*, 4(1):1. (Cited on pages 36 and 38.)

Pasko, V. P., Celestin, S., Bourdon, A.; Janalizadeh, R., and Jansky, J. (2023). Conditions for inception of relativistic runaway discharges in air. *Geophysical Research Letters*, 50(7):e2022GL102710. (Cited on pages 4, 6, 8, 10, 48, 80, 86, 88, 90, 94, 96, 108 and 118.)

Pilkington, G. R. and Anger, C. D. (1971). A Monte Carlo analysis of the passage of auroral X-rays through the atmosphere. *Planetary and Space Science*, 19(9):1069–1085. (Cited on pages 19 and 110.)

Pu, Y., Cummer, S. A., Lyu, F., Briggs, M., Mailyan, B., Stanbro, M., and Roberts, O. (2019). Low frequency radio pulses produced by terrestrial

gamma-ray flashes. *Geophysical Research Letters*, 46(12):6990–6997. (Cited on pages 3, 56, 59 and 72.)

Raizer, Yuri P., E. M. B. (2000). *Lightning Physics and Lightning Protection*. CRC Press, Boca Raton. (Cited on page 72.)

Saleh, Z., Dwyer, J., Howard, J., Uman, M., Bakhtiari, M., Concha, D., Stapleton, M., Hill, D., Biagi, C., and Rassoul, H. (2009). Properties of the x-ray emission from rocket-triggered lightning as measured by the thunderstorm energetic radiation array (tera). *Journal of Geophysical Research: Atmospheres*, 114(D17). (Cited on page 7.)

Santos, J. P., Parente, F., and Kim, Y.-K. (2003). Cross sections for K-shell ionization of atoms by electron impact. 36(21):4211. (Cited on page 13.)

Schaal, M. M., Dwyer, J. R., Saleh, Z. H., Rassoul, H. K., Hill, J. D., Jordan, D. M., and Uman, M. A. (2012). Spatial and energy distributions of x-ray emissions from leaders in natural and rocket triggered lightning. *Journal of Geophysical Research: Atmospheres*, 117(D15). (Cited on page 7.)

Schmalzried, A., Luque, A., and Lehtinen, N. (2022). Enhancing higher-energy spectral resolution for electron particle simulations in air. *Computer Physics Communications*, 277:108366. (Cited on page 38.)

Seltzer, S. M. and Berger, M. J. (1986). Bremsstrahlung energy spectra from

electrons with kinetic energy 1 keV–10 GeV incident on screened nuclei and orbital electrons of neutral atoms with Z = 1–100. *Atomic Data and Nuclear Data Tables*, 35(3):345–418. (Cited on pages 18 and 110.)

Shao, X.-M. (2016). Generalization of the lightning electromagnetic equations of uman, mclain, and krider based on jefimenko equations. *Journal of Geophysical Research: Atmospheres*, 121:3363–3371. (Cited on page 58.)

Shyn, T. W., Stolarski, R. S., and Carignan, G. R. (1972). Angular Distribution of Electrons Elastically Scattered from N_2. *Physical Review A: General Physics*, 6:1002. (Cited on page 14.)

Skeie, C. A., Østgaard, N., Mezentsev, A., Bjørge-Engeland, I., Marisaldi, M., Lehtinen, N., Reglero, V., and Neubert, T. (2022). The Temporal Relationship Between Terrestrial Gamma-Ray Flashes and Associated Optical Pulses From Lightning. *Journal of Geophysical Research: Atmospheres*, 127(17):e2022JD037128. (Cited on pages 3 and 106.)

Skeltved, A. B., Østgaard, N., Carlson, B., Gjesteland, T., and Celestin, S. (2014). Modeling the relativistic runaway electron avalanche and the feedback mechanism with GEANT4. *Journal of Geophysical Research: Space Physics*, 119(11):9174–9191. (Cited on pages 6, 48, 86, 88, 90, 94, 96 and 118.)

Smith, D. M., Dwyer, J. R., Hazelton, B. J., Grefenstette, B. W., Martinez-McKinney, G. F. M., Zhang, Z. Y., Lowell, A. W., Kelley, N. A., Splitt, M. E., Lazarus, S. M., Ulrich, W., Schaal, M., Saleh, Z. H., Cramer, E., Rassoul, H., Cummer, S. A., Lu, G., Shao, X.-M., Ho, C., Hamlin, T., Blakeslee, R. J., and Heckman, S. (2011). A terrestrial gamma ray flash observed from an aircraft. *Journal of Geophysical Research: Atmospheres*, 116(D20). (Cited on page 3.)

Tilles, J. N., Krehbiel, P. R., Stanley, M. A., Rison, W., Liu, N., Lyu, F., Cummer, S. A., Dwyer, J. R., Senay, S., Edens, H., Fan, X., Brown, R. G., and Wilson, J. (2020). Radio Interferometer Observations of an Energetic in-Cloud Pulse Reveal Large Currents Generated by Relativistic Discharges. *Journal of Geophysical Research: Atmospheres*, 125(20):e32603. (Cited on pages 3 and 106.)

Uman, M. A., McLain, D. K., and Krider, E. P. (1975). The electromagnetic radiation from a finite antenna. *American Journal of Physics*, 43(1):33–38. (Cited on pages 58, 59 and 129.)

Villasenor, J. and Buneman, O. (1992). Rigorous charge conservation for local electromagnetic field solvers. *Computer Physics Communications*, 69(2):306–316. (Cited on page 33.)

Wang, M. C. and Kunhardt, E. E. (1990). Streamer dynamics. *Physical Review A*, 42(4):2366–2373. (Cited on page 64.)

Wilson, C. T. R. (1925). The Acceleration of β-particles in Strong Electric Fields such as those of Thunderclouds. *Mathematical Proceedings of the Cambridge Philosophical Society*, 22(4):534–538. (Cited on page 5.)

Xu, W., Celestin, S., and Pasko, V. P. (2012). Source altitudes of terrestrial gamma-ray flashes produced by lightning leaders. *Geophysical Research Letters*, 39:L08801. (Cited on page 1.)

Xu, W., Celestin, S., and Pasko, V. P. (2014). Modeling of x-ray emissions produced by stepping lightning leaders. *Geophysical Research Letters*, 41(20):7406–7412. (Cited on page 7.)

Xu, W., Celestin, S., and Pasko, V. P. (2015). Optical emissions associated with terrestrial gamma ray flashes. *Journal of Geophysical Research: Space Physics*, 42. (Cited on pages 3 and 13.)

Xu, W., Celestin, S., Pasko, V. P., and Marshall, R. A. (2019). Compton scattering effects on the spectral and temporal properties of terrestrial gamma-ray flashes. *Journal of Geophysical Research: Space Physics*, 124(8):7220–7230. (Cited on page 72.)

Xu, W., Marshall, R. A., Celestin, S., and Pasko, V. P. (2017). Modeling

of x-ray images and energy spectra produced by stepping lightning leaders. *Journal of Geophysical Research: Atmospheres*, 122(21):11,776–11,786. (Cited on page 7.)

Østgaard, N. et al. (2023). Results from the aloft mission: a flight campaign for tgf and gamma-ray glow observations over central america and the caribbean in july 2023. In *AGU Fall Meeting 2023, San Francisco*. Session AE22A: Energetic Radiation from Lightning and Thunderstorms I Oral (Michael Briggs, Brant Carlson, Amitabh Nag) ; Abstract AE22A-03. (Cited on pages 3, 4 and 106.)

Pierre GOURBIN

Modélisation auto-consistente d'avalanches d'électrons runaway relativistes produisant des flashs gamma terrestres

Résumé :

Les flashs de rayons gamma terrestres (TGFs) sont des émissions très intenses et très brèves de rayons gamma se produisant durant les orages. Rapportés pour la première fois en 1994, de nombreuses recherches ont été menées afin de comprendre ses propriétés et origines. Il y a consensus quant au fait que les TGFs sont produits dans les nuages d'orage par des avalanches d'électrons runaway relativistes (RREAs): un électron soumis à un champ électrique suffisamment élevé peut gagner plus d'énergie du champ qu'il n'en perd via les collisions avec les molécules de l'air, devenant ainsi runaway. Il peut ainsi se propager et ioniser l'air, libérant de nouveaux électrons, dont certains sont runaway, formant ainsi une avalanche d'électrons runaway. Il y a cependant débat quant au contexte de l'initiation des RREAs dans les nuages orageux. Deux théories sont considérées à ce jour. Le mécanisme de feedback relativiste repose sur la propagation vers l'arrière de photons et de positrons produits par une première RREA, lesquels pourraient produire de nouvelles avalanches au voisinage de la position de départ de la première RREA, permettant ainsi d'atteindre un nombre suffisant d'électrons et de photons. Le mécanisme de runaway thermique suppose que les RREAs sont créées pendant la propagation des éclairs: le champ électrique intense induit dans les couronnes de streamers qui se forment au bout de traceurs d'éclairs pourraient accélérer une grande quantité d'électrons en provenance du leader, initiant ainsi la production de RREAs menant à un TGF.

Dans cette thèse, nous formulons deux questions non résolues que nous abordons dans les chapitres suivants. De quelle manière la dynamique des RREAs est-elle affectée par des effets auto-consistents ? Quelle est l'importance des aspects spatiaux et temporels dans l'initiation du feedback relativiste ?

Pour répondre à ces questions, nous avons mis au point un modèle relativiste auto-consistent, utilisant une technique de Monte Carlo pour simuler les collisions avec les molécules de l'air couplée à une méthode particle-in-cell (PIC) électromagnétique, qui résout les équations de Maxwell à chaque pas de temps afin de fournir une description détaillée des interactions entre le champ électromagnétique et les électrons. À notre connaissance, ce modèle constitue la première description pleinement causale des RREAs. En utilisant ce nouvel outil, nous avons découvert que la densité d'électrons de basse énergie saturait à une valeur prédictible. Nous montrons également qu'une limite fondamentale existe pour le nombre d'électrons et de photons de haute énergie, avec une magnitude correspondant aux observations de TGFs, et déduisons une formule simple donnant la densité de saturation et le nombre d'électrons. Afin de mieux comprendre le mécanisme de feedback relativiste, nous mettons au point une méthode afin de déterminer la valeur du champ électrique seuil pour le feedback. Nous réalisons ensuite des simulations du processus de feedback en utilisant le modèle complet, afin d'apprécier la complexité du phénomène. À partir des résultats, nous démontrons l'importance de prendre en compte tous les aspects spatio-temporels du processus de feedback relativiste afin de le décrire correctement. Les résultats semblent également supporter l'idée que le mécanisme de feedback relativiste n'agit pas seul dans la production des TGFs les plus courts et les plus intenses.

Mots clés : flashs de rayons gamma terrestres, plasmas, particle-in-cell, modélisation, runaway, décharges

Université d'ORLÉANS

Laboratoire de Physique et Chimie de l'Environnement et de l'Espace (LPC2E), 3A Avenue de la Recherche Scientifique, 45071, Orléans, CEDEX 02, France

LPC2E

Pierre GOURBIN

Self-consistent modeling of relativistic runaway electron avalanches producing terrestrial gamma ray flashes

Summary :

Terrestrial gamma ray flashes (TGFs) are short and intense bursts of gamma rays occurring during thunderstorms. Reported for the first time in 1994, a significant effort has been carried out to understand their properties and origins. It is agreed upon that TGFs are produced inside thunderclouds by relativistic runaway electron avalanches (RREAs): when submitted to a sufficiently high electric field, an electron can gain more energy from the field than it loses to collisions with air molecules, thus becoming runaway. Doing so, it ionizes the air, freeing more electrons, a small fraction of these electrons being themselves runaway, hence forming an avalanche of runaway electrons. The exact context in which RREAs are initiated inside thunderclouds remains up for debate. Two TGF-production theories are considered nowadays. The relativistic feedback mechanism relies on the backward propagation of photons and positrons created by a first RREA, to produce new avalanches near the starting location of the first RREA, allowing for an overall sufficient number of electrons and photons. The thermal runaway mechanism assumes that RREAs are created during lightning propagation: the strong electric field inside a streamer corona at the tip of leader could accelerate a high number of electrons injected from the leader, triggering the production of subsequent RREAs leading to a TGF.

In this thesis, we formulate two outstanding research questions that we address in the chapters. How the dynamics of RREAs is affected by self-consistent effects ? What is the importance of combined spatial and temporal aspects in the initiation of relativistic feedback ?

To address these questions, we have developed a new self-consistent relativistic model, using a Monte Carlo technique to simulate collisions with air molecules coupled with an electromagnetic particle-in-cell method, that solves the Maxwell-Ampere and Maxwell-Faraday equations at each timestep in order to represent accurately the interaction between the electromagnetic field and electrons. To our knowledge, this model constitutes the first fully causal relativistic description of RREAs. Using this new tool, we discovered that the low-energy electron density saturates at a predictable value. We also show that a fundamental limit exists in the number of high-energy electrons and photons, with a magnitude matching TGF observations, and derive a simple formula giving the observed saturation density and electron number. In order to better understand the relativistic feedback mechanism, we devise a method to derive a value of the feedback threshold electric field. We then perform simulations of the feedback process using the complete model, which allows us to fully appreciate the complexity of the phenomenon. From the results, we highlight the importance of considering all spatial and temporal aspects of the feedback process to describe it accurately. The results indicate that the relativistic feedback mechanism is unlikely to act alone in the production of the shortest or most intense TGFs.

Keywords : Terrestrial Gamma Ray Flash, plasmas, particle-in-cell, modelling, runaway, discharges

Université d'ORLÉANS

Laboratoire de Physique et Chimie de l'Environnement et de l'Espace (LPC2E), 3A Avenue de la Recherche Scientifique, 45071, Orléans, CEDEX 02, France

LPC2E